Mechanistic Insights into the Role of Sulfur Ligation in the Oxidative Reactivity of Non-Heme High-Valent Iron Complexes

A Thesis Submitted in Partial Fulfilment of the
Requirements for the degree of

DOCTOR of PHILOSOPHY

JAGNYESH KUMAR SATPATHY

Department of Chemistry
Indian Institute of Technology Guwahati
Guwahati, India

Prof. Chivukula V. Sastri; Supervisor

August 2024

Dedicated to
My Family

CONTENTS

STATEMENT

I am presenting this thesis as part of the requirements for the doctoral degree at the Indian Institute of Technology Guwahati. I affirm that the research presented in this thesis was conducted by myself in the Department of Chemistry at the Indian Institute of Technology Guwahati, India, under the guidance of Prof. Chivukula V. Sastri between 2019 and 2024. Consistent with the standard practice of scientific reporting, appropriate acknowledgments have been provided, and references to the original sources have been cited whenever the work is based on findings by other researchers.

Jagnyesh Kumar Satpathy

Date: _____/_____/_____

Place: Guwahati, 781039, India

CERTIFICATE

I certify that Jagnyesh Kumar Satpathy (196122016), a full-time PhD research scholar enrolled in the Department of Chemistry at the Indian Institute of Technology Guwahati, has been working under my supervision since July 2019. I am forwarding his thesis titled '**Mechanistic Insights into the Role of Sulfur Ligation in the Oxidative Reactivity of Non-Heme High-Valent Iron Complexes**' for consideration of the PhD (Science) degree from this institute. I confirm that he has met all the institute's requirements pertaining to the research presented in his thesis and that this work has not been submitted elsewhere for any other degree

Prof. Chivukula V. Sastri

Thesis Supervisor

Department of Chemistry

Indian Institute of Technology Guwahati

ACKNOWLEDGEMENTS

The research conducted during the tenure of my PhD is systematically presented in the form of this thesis. I am deeply grateful to all the people who have supported me directly or indirectly during my journey at the Indian Institute of Technology Guwahati. Foremost, I would like to express my deepest gratitude to my advisor, Prof. Chivukula V. Sastri, whose expertise, understanding, and patience added considerably to my graduate experience. His unwavering support and insightful guidance have been invaluable throughout my research journey.

I would like to express my gratitude to my Doctoral Committee Chairman, Dr. Pavan Kancharla, and members, Prof. Mohd. Qureshi, Prof. Aditya Narayan Panda, and Dr. Manabendra Sarma, for their valuable time in evaluating my progress and offering helpful suggestions to enhance my research. I am thankful to the former and current heads of the Department of Chemistry and the faculty members for their assistance throughout my research. My thanks also extend to the staff of the Chemistry department, whose support was essential to my work. I appreciate the Department of Chemistry and Central Instruments Facility (CIF) at IIT Guwahati for providing advanced instruments and infrastructure, and the Param Ishan server for computational facilities. Special thanks to Dr. K. K. Senapati and Dr. Babulal Das for their valuable guidance in learning and operating the SCXRD instrument.

I am grateful to IIT Guwahati and MHRD (Govt. of India) for financial support and resources throughout my tenure. I also thank our collaborators, Dr. Sam P. de Visser (University of Manchester, UK), Prof. Dr. Peter Comba (University of Heidelberg, Germany), Prof. Devesh Kumar (Babasaheb Bhimrao Ambedkar

University, India), Prof. Ebbe Nordlander (Lund University, Sweden) and Dr. Apparao Draksharapu for their valuable contributions to my research.

I extend my heartfelt thanks to my lab seniors, Dr. Gourab Mukherjee, Dr. Sayanta Sekhar Nag, and Dr. Umesh Kumar Bagha for their unwavering support and guidance. I am grateful for their willingness to share experiences and discuss innovative solutions to many challenges. I appreciate Dr. Rolly Yadav, Limashree Sahoo, and Payal Panwar for their invaluable help and support. They created a vibrant lab environment that encouraged productive ideas. Beyond research, getting to know each other and socializing with them was truly enjoyable.

I feel grateful to have been surrounded by friends who were instrumental during my time in Guwahati. I consider myself fortunate to have elder brothers such as Dr. Dilip Kumar Sahu, Dr. Tushar Kanta Sahu Dr. Biswajit Nayak, Dr. Umesh Kumar Bagha, Dr. Manoj Kumar Mohanta, and Dr. Bipin Kumar Behera, who warmly welcomed me to IITG and provided unwavering support, motivation and guidance. Following intensive research work, I fondly recall spending enjoyable times with them. Also, I consider myself lucky and blessed to have some amazing friends at IITG, with whom I have had some of the most amazing moments during my stay at IITG. I would like to name a few, Abhay Pratap Singh, Sourav Kumar, Maitery Yadav, Ritwika, Rahul Ahmed, Akash Dev Roshan, Vishnu G, Anil, Vishwa, Subham, Deepak, Alpana, Anandita, Sreekant and the list goes on. These are the most amazing people, who have given me cherished memories of fun, exploring, and playing cricket together. I am truly grateful to them. The cricket ground at IITG was my sanctuary, where I could escape the routine and release the stresses of research. Therefore, I am thankful to the sports board for providing the necessary resources.

I would like to thank all of my teachers for believing in me and motivating me to achieve my goal. Special mention goes to my teachers at Sambalpur University, Dr. Hirak Chakraborty, Dr. Satya Narayan Sahu, Dr. Amaresh Mishra, Prof. Pramila Kumari Mishra, Prof. Pradipta Kumar Behera, Dr. Ram Naresh Mahaling and Dr. Naba Krushna Behera for inspiring and implanting in me a love towards research for this subject. I am grateful and obliged to all my teachers from my schooling days, 12^{th} days, and graduation period for taking a vital role in making me the person I am today.

Last but certainly not least, I owe immense gratitude to my family and loved ones. I am deeply proud to have the unwavering love, support, and sacrifices of my parents, Shri Lalu Satpathy and Smt. Sunita Satpathy, as well as the support of my younger brother, Mr. Debesh Kumar Satpathy. They have stood by me through all the challenges and triumphs. I cannot imagine reaching this stage without their endless support and sacrifices.

I would like to thank everyone who contributed in some way or the other to the successful completion of this thesis. Your support and encouragement have been essential.

Thank you all for being part of this journey.

ABSTRACT

In recent years, there has been growing interest in understanding the mechanistic intricacies of high-valent metal intermediates involved in oxidation reactions, particularly within the realm of bio-inorganic chemistry. This thesis delves into the study of high-valent non-heme iron metalloenzymes, contributing to the extensive literature on this subject. A central focus is placed on investigating the impact of sulfur ligation on the stability and oxidative reactivity of various high-valent iron-oxygen and iron-nitrogen intermediates. Novel pentadentate N4S ligand frameworks were synthesized, and their iron(II) complexes were characterized, revealing consistent equatorial coordination of sulfur to iron across different systems.

In this thesis, we have explored the influence of equatorially ligated sulfur on the oxidative reactivity of iron(IV)-oxo complexes. The investigation demonstrates that sulfur incorporation enhances reaction rates in sulfoxidation and C-H bond activation reactions, accompanied by alterations in reaction pathways. Which seems to be novel for high-valent non-heme iron(IV)-oxo complexes. Also, the one-electron reduction potential of the iron(IV)-oxo complexes have been determined using marcus theory for electron transfer reactions. Also, we present the pioneering experimental characterization of a sulfur-ligated iron(IV)-tosylimido complex, examining its oxidative reactivity in sulfoxidation and C-H bond activation reactions. The iron(IV)-NTs species have been spectroscopically well characterized and its reactivity have been explored with a variety of substrates. We extend this exploration with the characterization of a sulfur-ligated iron(III)-alkylperoxide complex, evaluating its reactivity in oxygen atom transfer and aldehyde deformylation reactions.

Through systematic investigation, this thesis contributes new insights into the role of sulfur ligation in modulating the stability and reactivity of high-valent iron intermediates, highlighting its significance in bio-inorganic chemistry and oxidation catalysis.

LIST OF TABLES

LIST OF SCHEMES & FIGURES

ABBREVIATIONS

ESI-MS	Electrospray Ionization Mass Spectrometry
UV/Vis	Ultraviolet Visible
NMR	Nuclear Magnetic Resonance
VT-NMR	Variable Temperature Nuclear Magnetic Resonance
XRD	X-Ray Diffraction
GC	Gas Chromatography
LCMS	Liquid Chromatography Mass Spectrometry
UPLC	Ultra Performance Liquid Chromatography
EPR	Electron Paramagnetic Resonance
ROS	Reactive Oxygen Species
CYP	Cytochrome P450
SOR	Superoxide Reductase
His	Histidine
CDO	Cysteine Dioxygenase
α-KG	α-ketoglutarate
TauD	taurine/α-KG dioxygenase
pdb	Protein Data Bank
EXAFS	Extended X-ray Absorption Fine Structure
PhIO	Iodosylbenzene
^{s}PhIO	Soluble Iodosylbenzene
^{s}PhINTs	Soluble N-tosyliminobenzyliodinane
*t*BuOOH	*tert*-butyl hydroperoxide

CmOOH	cumene hydroperoxide
TMC	Tetramethylcyclam
BnTPEN	N^1-benzyl-N^1,N^2,N^2-tris(pyridine-2-ylmethyl)ethane-1,2-diamine
OOH	Hydroperoxo
OOR	Alkylperoxo
HAA	Hydrogen Atom Abstraction
OAT	Oxygen Atom Transfer
DFT	Density Functional Theory
THF	Tetrahydrofuran
DCM	Dichloromethane
CAN	Cerium (IV) ammonium nitrate
DMS	dimethylsulfide
m.p.	Melting point
RT	Room temperature
THA	Thioanisole
CHD	1,4-Cyclohexadiene
CCA	cyclohexanecarboxaldehye
DHA	9,10-Dihydroanthracene
PhEt	Ethylbenzene
OTf	triflate
ppm	Parts per million
Q-TOF	Quadrupole Time of Flight
KIE	Kinetic Isotope Effect
k_{obs}	pseudo first-order rate constant

k_2	second-order rate constant
BDE	bond dissociation energy
EA	Electron affinity
MLCT	Metal to ligand charge transfer
LMCT	Ligand to Metal charge transfer
NIR	Near-Infrared

COMPOUND ABBREVIATIONS

Chapter	Index	Description
Chapter III	L1	N5 ligand
	1a	$[Fe^{II}(N5)]^{2+}$
	1b	$[Fe^{IV}(O)(N5)]^{2+}$
	L2	N4S ligand
	2a	$[Fe^{II}(N4S)]^{2+}$
	2b	$[Fe^{IV}(O)(N4S)]^{2+}$
Chapter IV	L5	BnTPeN ligand
	5b	$[Fe^{IV}(O)(BnTPeN)]^{2+}$
	5c	$[Fe^{IV}(NTs)(BnTPeN)]^{2+}$
	L6	STPeN ligand
	6b	$[Fe^{IV}(O)(STPeN)]^{2+}$
	6c	$[Fe^{IV}(NTs)(STPeN)]^{2+}$
Chapter V	L8	$STPeN^{CH2}$ligand
	10a	$[Fe^{II}(STPeN^{CH2})(OTf)]^{+}$
	10b	$[Fe^{III}(STPeN^{CH2})(t\text{BuOO})]^{2+}$

SYNOPSIS

Name of the student: **Jagnyesh Kumar Satpathy** Roll No.: **196122016**

Degree for which submitted: **Ph. D.** Department: **Chemistry**

Thesis Title: **Mechanistic Insights into the Role of Sulfur Ligation in the Oxidative Reactivity of Non-Heme High-Valent Iron Complexes**

Name of Thesis supervisor: **Prof. Chivukula V. Sastri**

Month and year of thesis submission: **August, 2024**

The thesis has been organized into five chapters. Introductory **Chapter 1** addresses the primary aim of the work carried out in this thesis, along with scope and purpose of the present investigation. It presents an overview on the sulfur ligated iron metalloenzymes. Also, recent advancements in the rich chemistry of iron(IV)-oxo, iron(IV)-tosylimido and iron(III)-alkylperoxo species have been discussed. Relevant references of such species present in biology and the work presented in this thesis have been cited as well.

Chapter II. Synthesis and Characterization, Materials Employed and Methods Adapted.

This chapter focuses on an in-depth examination of the synthesis of oxidants, ligands and metal complexes, including their structural characterization. It also covers the role of solvents and the deliberate use and synthesis of particular substrates to determine the reactivity profiles of different intermediates. The synthesis of all the ligands utilized in this thesis has been thoroughly discussed,

including their spectroscopic characterization. Additionally, the chapter covers the preparation of metal complexes and the application of techniques such as electrospray ionization mass spectrometry (ESI-MS), ultraviolet-visible (UV/Vis) spectroscopy, Nuclear magnetic resonance spectroscopy, and single-crystal X-ray diffraction (XRD). Furthermore, it provides comprehensive descriptions of the physical methods employed and the procedures for analyzing reaction kinetics.

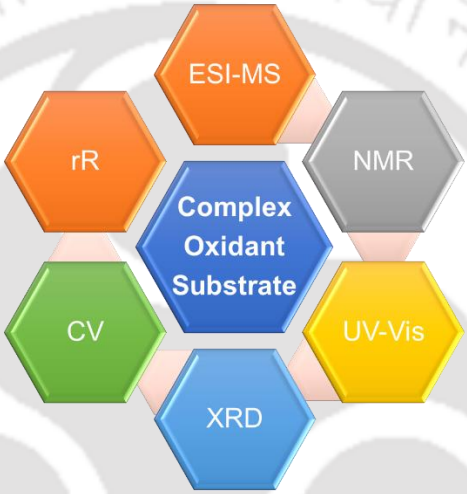

Chapter III. Enhanced Reactivity through Equatorial Sulfur Coordination in Nonheme Iron(IV)-Oxo Complexes: Insights from Experiment and Theory.

Sulfur ligation in metalloenzymes often gives the active site unique properties, whether it is the axial cysteinate ligand in the cytochrome P450s or the equatorial sulfur/thiol ligation in nonheme iron enzymes. In this work, we report the generation of a room temperature stable sulfur ligated iron(IV)-oxo complex bearing a pentadentate N_4S ligand, **2b** (N_4S = 1-thia-4,7-bis(2 pyridylmethyl)diazacyclononane). The complex was spectroscopically well characterized with UV-vis spectroscopy, ESI-MS spectrometry and resonance Raman spectroscopy. The reactivity in sulfoxidation and C-H bond activation reaction has been studied and compared with its parent N_5 ligated Fe(IV)-oxo

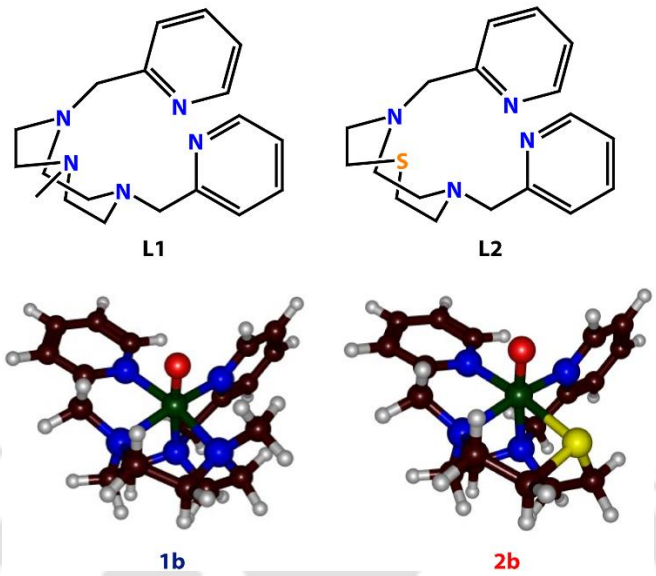

Fig. S1. Ligands and oxidants used in this chapter.

complex, **1b** (N_5 = *N*-methyl-*N*',*N*-bis(2-pyridylmethyl)-1,4,7-triazacyclononane). We observed that, there is a significant improvement in the reaction rates in both sulfoxidation as well as C-H bond activation reaction with sulfur incorporation. Also, we see a change in reaction pathway from direct oxygen atom transfer to electron transfer for **2b** in suldoxidation reaction. Whereas we observed a hydride transfer pathway in C-H activation reaction for **2b**. The redox potential values $Fe^{IV/III}$ seems to be increasing 480 mV for **2b**.

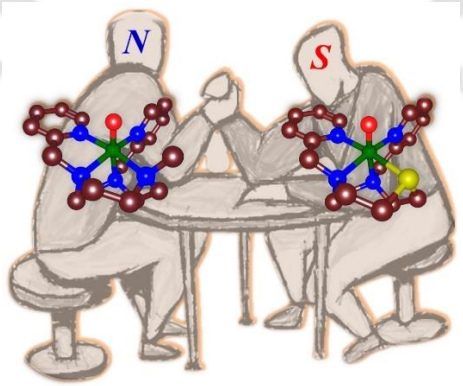

Chapter IV. Exploring a Sulfur Ligated Iron(IV)-Tosylimido species: A Comparative Study with its Oxo-Analogue.

High-valent metal-oxo and metal-nitrido species are crucial intermediates in enzymes, playing crucial roles in the catalytic cycles of various oxidases and nitrogenases. Many oxygenases utilize molecular oxygen to produce high-valent non-heme iron(IV)-oxo or iron(IV)-oxo heme cation radical species as the active oxidants. Conversely, a smaller subset of enzymes employs nitrogen to form high-valent iron(IV)-nitrido or iron(IV)-imido species. The latter has been suggested as a potential intermediate in the nitrogenase enzyme system.

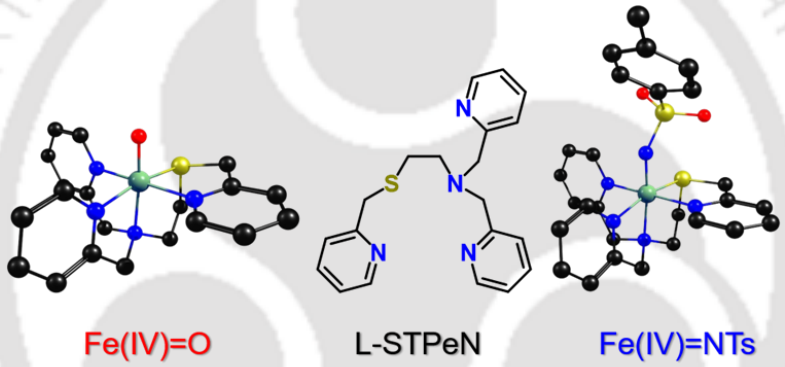

Fig. S2. Ligand and oxidants used in this chapter.

Herein, we report the synthesis of a sulfur ligated iron(IV)-NTs intermediate bearing a pentadentate ligand, **6c** STPeN = 2-(2-Pyridinyl)methylthio-N,N-bis[(2 pyridinyl)methyl]ethanamine. This species has been spectroscopically well characterized and its oxidative reactivity in sulfoxidation and C-H bond activation reaction has been investigated and compared with its Fe(IV)-oxo analogue, **6b**. There is change in reaction pathway from direct oxygen transfer to electron transfer in case of sulfoxidation reaction observed for **6c**. Also, we see a large KIE value of 85 in C-H bond activation reaction for **6c**. Which may be due to large quantum mechanical tunnelling.

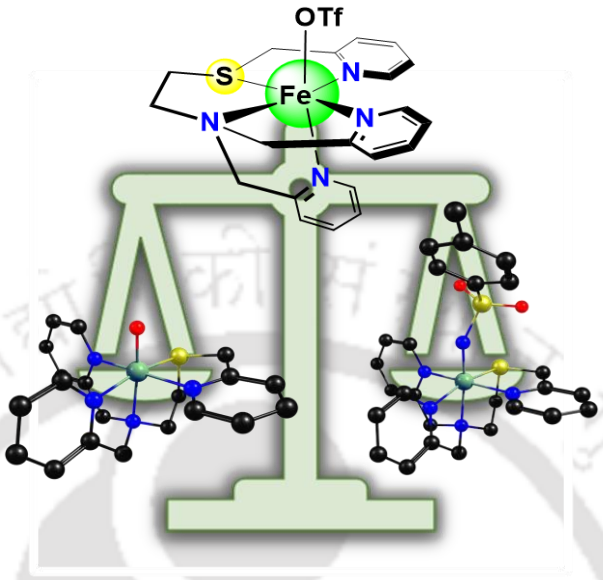

Chapter V. Sulfur Ligated Iron(III)-Alkylperoxide Complex: Spectroscopic Insights and Mechanistic Studies of Electrophilic Hydrogen Atom Abstraction with Aldehydes.

Iron(III)-hydroperoxides and alkylperoxides are known to be the active oxidants in various metalloenzymes. These complexes are known for their sluggish reactivity with organic substrates. In this work, we report the generation of a sulfur ligated low-spin iron(III)-alkylperoxide species bearing a pentadentate ligand framework, STPeN^{CH2} = 2-((2-(pyridin-2-yl)ethyl)thio)-N,N-bis(pyridin-2-

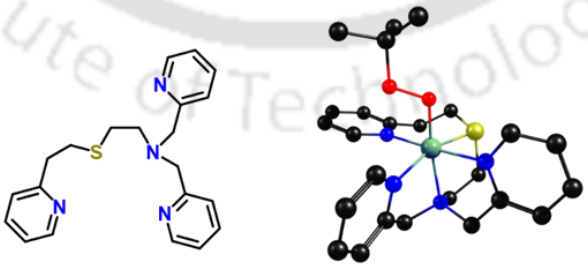

Fig. S3. Ligand and oxidants used in this chapter.

ylmethyl)ethan-1-amine). The species was characterized by UV-vis spectroscopy, EPR spectroscopy, resonance Raman spectroscopy and ESI-MS spectrometry. The reactivity study of this complex was investigated in oxygen atom transfer reaction and aldehyde deformylation reaction. In the reaction with cyclohexanecarboxaldehyde, we report here a novel aldehydic-H atom abstraction pathway with Fe^{III}-OOR species. Also, from experimental and computational analysis, we conclude that the Fe^{III}-OOR complex is reaction with organic substrates via O-O homolytic cleavage to form a putative Fe^{IV}=O species.

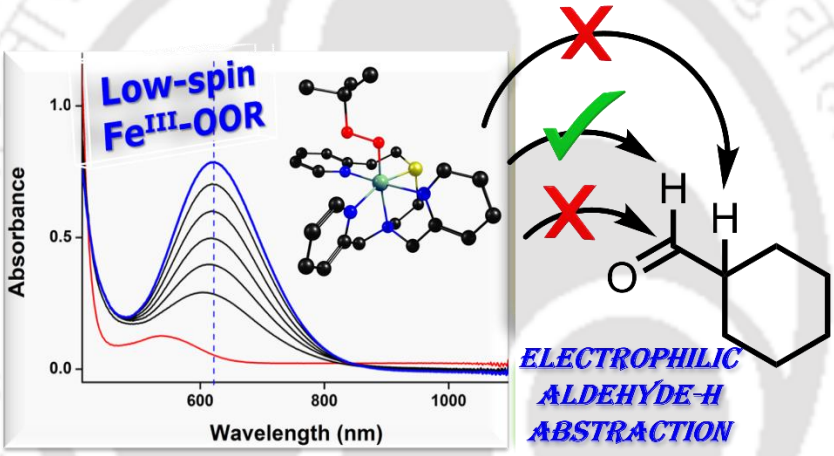

- **List of Publications**

1. **Satpathy, J. K.**; Yadav, R.; Bagha, U. K.; Kumar, D.; Sastri, C. V.; de Visser, S. P.; Enhanced Reactivity through Equatorial Sulfur Coordination in Nonheme Iron(IV)–Oxo Complexes: Insights from Experiment and Theory. *Inorg. Chem.* **2024**, *63*, 6752–6766.
2. Mukherjee, G.; Velmurugan, G.; Kerscher, M.; **Satpathy, J. K**.; Sastri, C. V.; Comba, P.; Mechanistic Insights into Amphoteric Reactivity of an Iron-Bispidine Complex. *Chem. Eur. J.* **2024**, *30*, e202303127.
3. Sahoo, L.; **Satpathy, J. K**.; Yadav, R.; de Visser, S. P.; Sastri, C. V.; Equatorial Perturbation Driven Reaction Bifurcation in Non-Heme Iron Complexes for Chlorite Oxidation. *Eur. J. Inorg. Chem*, **2023**, *26*, e202300380.
4. Bagha, U. K.; Yadav, R.; Mokkawes, T.; **Satpathy, J. K**.; Kumar, D.; Sastri, C. V.; de Visser, S. P. Defluorination of Fluorophenols by a Nonheme Iron(IV)-Oxo Species: Observation of a New Intermediate Along the Reaction. *Chem. Eur. J*. **2023**, *29*, e202300478.
5. Yeh, G, C-C.; Ghafoor, S.; **Satpathy, J. K.**; Mokkawes, T.; Sastri, C. V.; de Visser S. P. Cluster Model Study into the Catalytic Mechanism of α-Ketoglutarate Biodegradation by the Ethylene-Forming Enzyme Reveals Structural Differences with Nonheme Iron Hydroxylases. *ACS. Catal.*, **2022,** *12*, 3923-3937.
6. Bagha, U. K.; **Satpathy, J. K**.; Mukherjee, G.; Barman, P.; Kumar, D.; de Visser S. P.; Sastri, C. V. Oxidative dehalogenation of halophenols by high-valent nonheme iron(IV)-oxo intermediates. *Faraday Discuss.*, **2022**, *234*, 58–69.

7. Bagha. U. K.; **Satpathy. J. K**.; Mukherjee, G.; Sastri, C. V. de Visser, S. P. A Comprehensive Insight into Aldehyde Deformylation: Mechanistic Implications from Biology and Chemistry. *Org. Biomol. Chem*., **2021**, *19*, 1879-1899.
8. Roach, S.; Faponle, A. S.; **Satpathy, J. K**.; Sastri, C. V.; de Visser. S. P. Substrate sulfoxidation by a biomimetic cytochrome P450 Compound I mimic: How do porphyrin and phthalocyanine equatorial ligand compare?. *J. Chem. Sci*, **2021**, *133*, 61-74.
9. Mukherjee, G.; **Satpathy, J. K**.; Bagha, U. K.; Mubarak, M. Q. E.; Sastri, C. V.; de Visser, S. P. Inspiration from Nature: Influence of Engineered Ligand Scaffolds and Auxiliary Factors on the Reactivity of Biomimetic Oxidants. *ACS. Catal*., **2021**, *15*, 9761 - 9797.

GRAPHICAL ABSTRACT

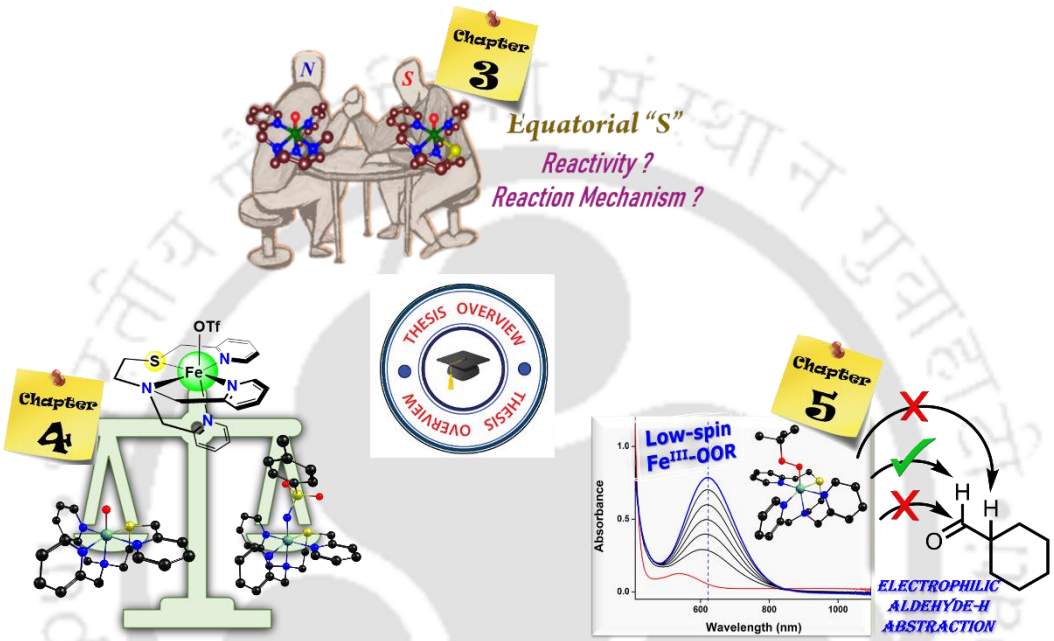

Synopsis

CHAPTER – I

A General Introduction into the Sulfur Ligated Heme and Non-Heme Iron Containing Metalloenzymes and Their Model Systems

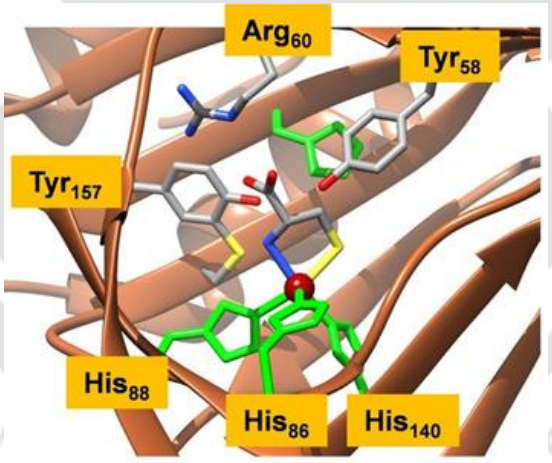

CDO

Metals ions in biology

Metal ions are essential in biological systems, as approximately one third of enzymes rely on them for catalytic activity. These ions are commonly incorporated into proteins, where they act as catalysts for crucial processes such as dioxygen transport and electron transfer, and also contribute to structural stability. Bioinorganic chemistry is dedicated to comprehending the roles of metal ions in living organisms, encompassing their selection, uptake mechanisms, regulation of concentrations, and specific biological functions. Collectively, metal ions are indispensable for sustaining various biological processes, underscoring their fundamental importance in supporting life.[1]

Metalloenzymes constitute a distinct category of metalloproteins that facilitate catalytic reactions. These enzymes catalyse reactions at their protein active sites. Investigating how nature manages these reactions involves studying the molecular-level structure of metalloprotein active sites alongside enzyme microbiology. Due to their substantial size, obtaining high-resolution structural details about the metal centers active site coordination is often challenging. Critical information such as bond lengths, proton presence, or intermediate identities can be incomplete due to constraints imposed by biological systems or physical techniques. Furthermore, probing the chemical reactivity of these enzymes is hindered by the resolution limits of techniques applicable to large biomolecules and the complexities of interpreting spectra when multiple metal centers are present. Addressing these challenges, synthetic modeling has emerged as a valuable approach. This method enables the acquisition of structural and mechanistic insights into the chemistry occurring at these sites. Model systems are designed to emulate the physical and chemical attributes of biomolecular metal centers, either by replicating known active sites or by hypothesizing structures based on spectroscopic data, thus facilitating correlations between structure and function.[1]

The biological functions of metalloenzymes are diverse and are influenced by factors such as the type, oxidation state, number, and coordination environment of metal ions in their active sites. Enzymes catalysing non-redox reactions like hydrolysis often contain non-redox active metal ions such as zinc, whereas those involved in electron-transfer processes like oxygen transport and activation utilize metal ions with variable oxidation states like copper and iron. Understanding the structural and reactivity properties of metalloenzyme active sites often involves comparing them with synthetic models.[1] By replicating the immediate coordination sphere of the active site, synthetic models provide spectroscopic benchmarks that aid in characterizing and assigning metalloenzymes. Furthermore, functional models can offer valuable insights into potential reaction mechanisms, proposed structures of mechanistic intermediates, and the role of the metal ion in enzyme reaction pathways.

Iron Enzymes

Iron (Fe) is one of the predominant metal found in the active sites of metalloenzymes. As the most prevalent transition metal in the Earth's crust, iron plays a crucial role in many bioinorganic systems, thanks to its capability to exist in multiple oxidation states ranging from Fe(I) to Fe(V). Within these systems, iron exists in various forms such as Fe-S clusters, heme, and non-heme tri-, bi-, and mononuclear sites. Both heme and non-heme iron enzymes play essential roles in a variety of critical biological processes. These include the synthesis of serotonin, leukotrienes, and DNA, as well as other functions such as dioxygen activation, superoxide reduction and dismutation, methane monooxygenation, and extradiol synthesis.[3,4]

Although heme and non-heme systems share similarities, non-heme iron systems are less well understood because of the difficulties associated with their spectroscopic analysis.[5] These difficulties stem from the absence of intense π-π* transitions from porphyrin ligands and the spectroscopic silence of Fe(II), the common metal ion in these enzymes.[6] In the past twenty years, considerable focus has been placed on investigating mononuclear and binuclear non-heme iron enzymes. During this period, the Solomon group has advanced physical techniques to acquire electronic structural data for Fe(II).[4,6]

Mononuclear iron enzymes typically feature the "2-His-1-carboxylate triad," where substrates bind and dioxygen activation occurs at the vacant positions on the metal.[7] These enzymes commonly coordinate aspartic acid (Asp), glutamic acid (Glu), and histidine (His) to the iron at the active site. Current research focuses on identifying and stabilizing reactive intermediates crucial to understanding enzyme function. There are few reports of non-heme iron enzymes with cysteine (Cys) ligands, which are distinct from traditional histidine-ligated systems. While heme iron metalloenzymes like cytochrome P450 can contain cysteinate ligands, only a few non-heme iron enzymes with cysteinate ligands are currently known, each exhibiting specific and previously unreported functions such as superoxide reductases (SORs), cysteine dioxygenases, nitrile hydratases (NHases), and peptide deformylases (PDFs), all with available crystal structures.[8-12] In enzymes such as SOR and NHase, an unmodified cysteinate residue is located trans to the substrate-binding site. This positioning is believed to be critical for catalytic activity, although the precise mechanism by which it contributes remains not fully elucidated.

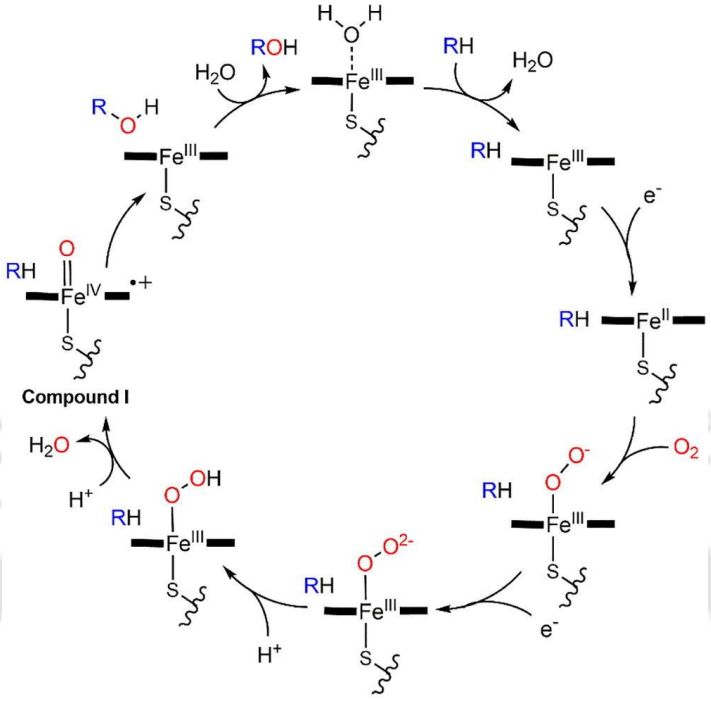

Figure. 1.1. Catalytic cycle of cytochrome P450.[14]

Cytochrome P450

The cytochrome P450 enzyme family is highly diverse, encompassing members that catalyze the oxidation of various substrates and perform multiple functions, including the bioremediation and detoxification of hydrocarbons.[13] The oxygen activation mechanism of cytochrome P450 has been extensively studied, and provides much of the insight into the mechanistic steps of oxygen activation by nonheme iron centers (Figure. 1.1)[14-15] In the iron(III) resting state, the iron center of cytochrome P450 is coordinated by four nitrogen ligands derived from a porphyrin dianion, in addition to an axial cysteinate and a proximal water ligand. The binding of the substrate causes the displacement of the water ligand and the subsequent reduction of the metal center to a high-spin iron(II) species. The introduction of oxygen and an electron then results in the formation of a

peroxoiron(III) or hydroperoxoiron(III) species. A combination of "push" and "pull" effects from the coordinated thiolate and distal protein residues, respectively, lead to heterolytic O-O bond cleavage of this intermediate.[16-18] This process yields water and a high-valent oxoiron(IV) species known as Compound I. Although formally an oxoiron(V) complex, Compound I has been identified as an oxoiron(IV) porphyrin cation radical complex.[19] This high-valent species is thought to abstract a hydrogen atom from the substrate, resulting in the formation of a substrate-based radical and a proposed hydroxoiron(IV) complex. This complex is believed to be analogous to Compound II found in chloroperoxidase, a closely related system.[20] Hydroxyl rebound to the substrate radical species[21-25]and subsequent dissociation complete the cycle by returning the enzyme to the resting state. This heme paradigm has informed much of our understanding of oxygen activation in biological systems; however recent studies challenge the accuracy of applying the P450 model to non-heme systems.

Superoxide Reductase

Superoxide reductases (SORs) are non-heme iron, intensely blue enzymes that are ligated with cysteinate and found in anaerobic bacteria.[26-28] Three crystal structures of SOR have been documented from two bacterial sources: *Pyrococcus furiosus*[29] and *Desulfovibrio desulfuricans*.[30] These enzymes exhibit a primary coordination motif similar to that of cytochrome P450, including the N4S donor system in the primary coordination sphere, with histidine residues substituting for the heme prosthetic group. The Fe(II) active site in SOR is coordinated by four equatorial histidines and one axial cysteinate residue.[29] Also, the Fe(II) active site in SOR possesses S=2 high spin character. Though, the structure-function relationship in SORs differs slightly. In SORs, the Fe-O bond in the ferric-hydroperoxide complex cleaves to release hydrogen peroxide. Additionally, the spin state of the iron center in SORs contrasts with that in P450: while P450 features a low-spin iron (S = 1/2)

in the peroxo species, SORs have a high-spin iron (S = 5/2). This suggests that SORs likely have a stronger O-O bond and a weaker Fe-O bond, thereby favoring the cleavage of the Fe-O bond.

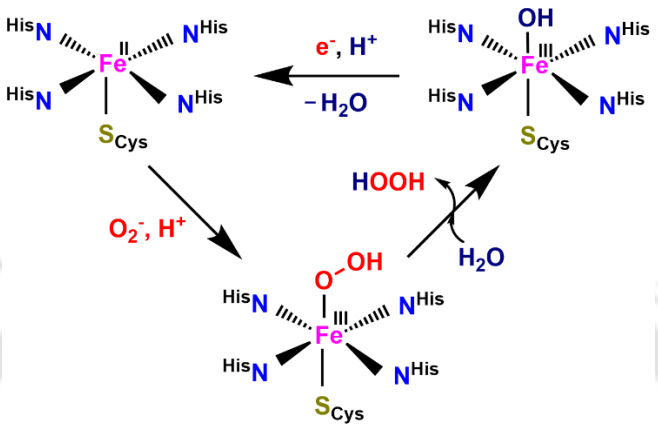

Figure 1.2. Catalytic cycle for superoxide reductase.[29]

Relationship between SOR and P450 Active Sites and Mechanism

The primary coordination sphere of the iron active site in superoxide reductases (SORs) bears a close resemblance to that of the heme enzyme cytochrome P450. Both enzymes feature an apical cysteinate opposite an open site and form an Fe(III)–OOH intermediate when reacting with oxygen-derived substrates. Despite these similarities, their reaction pathways diverge significantly. In P450, the O–O bond of the hydroperoxo intermediate is cleaved to produce a high-valent iron–oxo species, whereas in SOR, the Fe–O (peroxo) bond is broken, resulting in the release of hydrogen peroxide. Although the cysteinate is crucial for the O–O bond cleavage in P450, this mechanism does not occur in SOR. The reasons behind these different pathways remain unclear. Initially, it was believed that a porphyrin was essential for stabilizing a high-valent iron–oxo complex, but this assumption was challenged with the discovery of the first non-heme Fe(IV)=O complex.[32] Although theoretical investigations indicate that protonation sites could influence

the reaction pathway, precise protonation appears unlikely given that the metal ion is exposed on the protein surface.[31]

Cysteine dioxygenase

Maintaining adequate cysteine levels is essential for biological systems. Cysteine dioxygenase (CDO) plays a vital role in this process by converting free intracellular cysteine into cysteine sulfinic acid (CSA) using dioxygen. Besides mammals, Cysteine Dioxygenase (CDO) is also present in certain yeast and bacterial species. The active site of CDO features a unique geometry where, unlike the typical facial triad configuration involving two histidines and one carboxylate side-chain coordinating to iron (II), the iron is instead bound by three histidine ligands (Hist-86, 88, and 140).[33] Additionally, crystallographic studies show that the amino nitrogen and thiolate sulfur of cysteine, along with a single water molecule, are coordinated to the iron.[34]

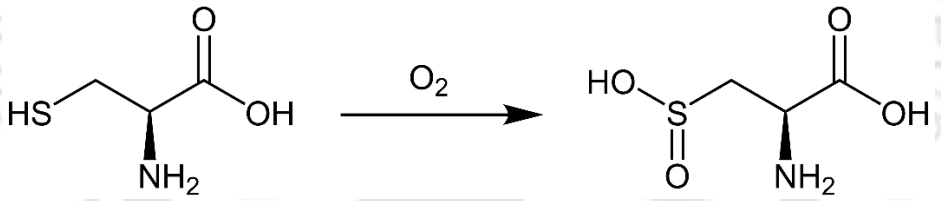

Scheme 1.1. Conversion of cysteine to cysteine sulfinic acid.[34]

Despite continuous research efforts, the mechanism of Cysteine Dioxygenase (CDO) remains inadequately understood. Generally, the reaction involves the spontaneous addition of O_2 to cysteine, though enzyme catalysis significantly enhances this process.[35,36] Studies suggest that the cysteinyl-tyrosine bridge lowers the oxidation potential of tyrosine, an electron donor in systems like photosystem II by approximately 0.5 V compared to phenol, while also increasing its acidity.

The thioether group likely plays a role in the enzyme's structure, redox reactions, or acid-base chemistry. Furthermore, Tyr157 has been recognized as essential for enzyme function, potentially acting as a tyrosinyl radical, and is highly conserved among various CDO variants.[35] Additionally, research has demonstrated that cysteamine, which is structurally similar to cysteine, can enhance the oxidation of cysteine but does not serve as a substrate for CDO. A proposed mechanism, supported by computational and spectroscopic studies, suggests that O2 binds cis to a thiolate, leading to the formation of a reactive iron (III)-superoxo species (A). This species then attacks the sulfur atom of the bound cysteine, resulting in the formation of a four-membered ring structure (B).[37-39] Heterolytic cleavage of the O-O bond results in the formation of a high-valent iron (IV) oxo intermediate (C), which enables the transfer of the second oxygen atom to the sulfur atom.[37,38]

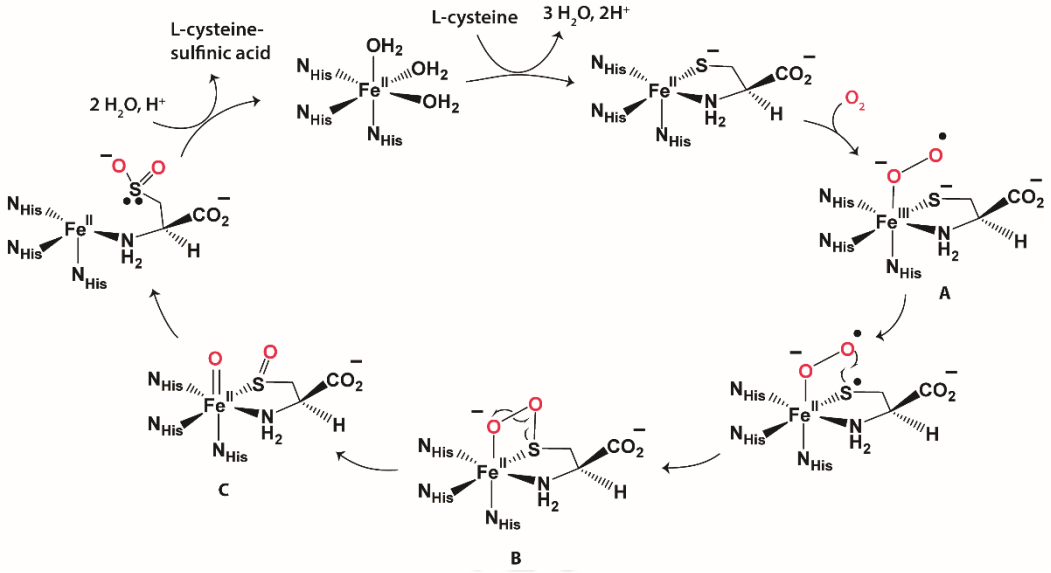

Figure. 1.3. Catalytic cycle of Cysteine dioxygenases.[37]

Isopenicillin N synthase

Isopenicillin N synthase (IPNS) is a critical enzyme in the production of penicillin and cephalosporin antibiotics. It facilitates the cyclization of the linear tripeptide δ-(L-α-aminoadipoyl)-L-cysteinyl-D-valine (ACV) to generate isopenicillin N, an essential intermediate in the antibiotic synthesis pathway.[40] It is a nonheme iron enzyme that belongs to the family of 2-oxoglutarate-dependent dioxygenases.

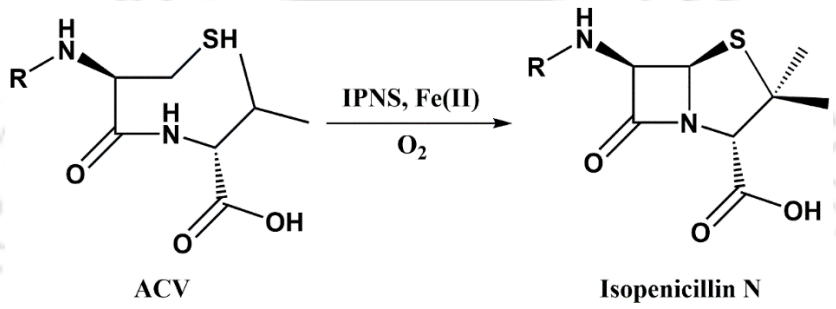

Scheme. 1.2. Conversion of ACV to Isopenicilin N by IPNS.[40]

The active site Fe(II) in CDO is coordinated by at least two histidine residues, one aspartate residue, one glutamine residue, and two water molecules in the absence of a bound substrate.[41] The Two histidine and one aspartic acid residue are highly conserved, indicating their essential role in the enzyme's function.[42] Specifically, His214, His270, and Asp216 are essential. The addition of ACV to the active site results in the replacement of Gln330 and a water molecule by the ACV thiolate.[43] The linear tripeptide δ-(L-α-aminoadipoyl)-L-cysteinyl-D-valine (LLD-ACV) is initially formed from its amino acid components by ACV synthase.[44] This helps in facilitating the binding of the ACV substrate to the cysteine residue's deprotonated thiol group.[43] The ACV is anchored in the active site by the thiolate's coordination with the iron centre. The Fe^{II}/Fe^{III} redox potential is lowered when ACV is bound, which facilitates the conversion of dioxygen to superoxide.[45,46] The reaction cycle is started when a robust RS-Fe^{III} bond forms, which lowers the activation barrier

for dioxygen binding.[43] A hydrogen atom transfer from C-3 of the cysteine residue to the distal superoxo oxygen converts Fe^{III} back to Fe^{II}. This reaction forms a thioaldehyde and a hydroperoxide ligand (OOH). The hydroperoxide ligand then deprotonates the amide, allowing it to close the β-lactam ring via a nucleophilic attack on the thioaldehyde carbon.[44]

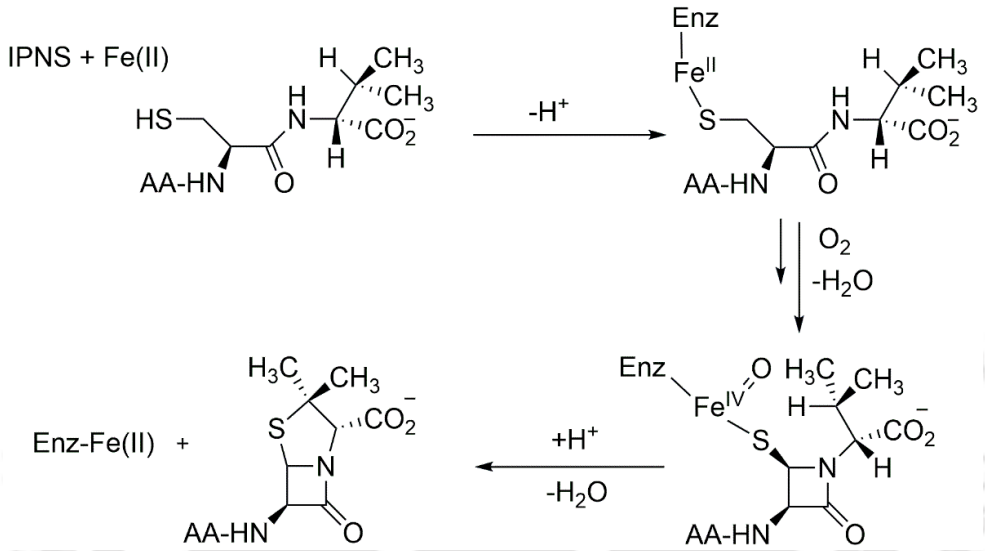

Figure. 1.4. Proposed reaction pathway for Isopenicillin N synthase enzyme.[43]

This positions the hydrogen atom on C-3 of the valine residue closer to the highly electrophilic iron(IV) oxo ligand. A second hydrogen transfer likely generates an isopropyl radical, which then closes the thiazolidine ring by attacking the thiolate sulfur atom.[44]

Biomimetic models

Early transition metal ions like iron (Fe), manganese (Mn), nickel (Ni), and cobalt (Co) are essential in metalloenzymes, where they activate molecular oxygen (O_2). This activation results in the formation of various metal-oxygen intermediates, such as metal(III)–peroxo, metal(III)–hydroperoxo, metal(III)–superoxo, and

metal(IV)–oxo species. These highly reactive intermediates play a critical role in oxidizing organic substrates and participating in various biological processes.[47-63] Many non-heme enzymes containing iron are essential in metabolism, catalyzing the activation of dioxygen (O_2). Figure 1.5 illustrates the speculated intermediates involved in these biotransformations catalyzed by iron and manganese.[64-69]

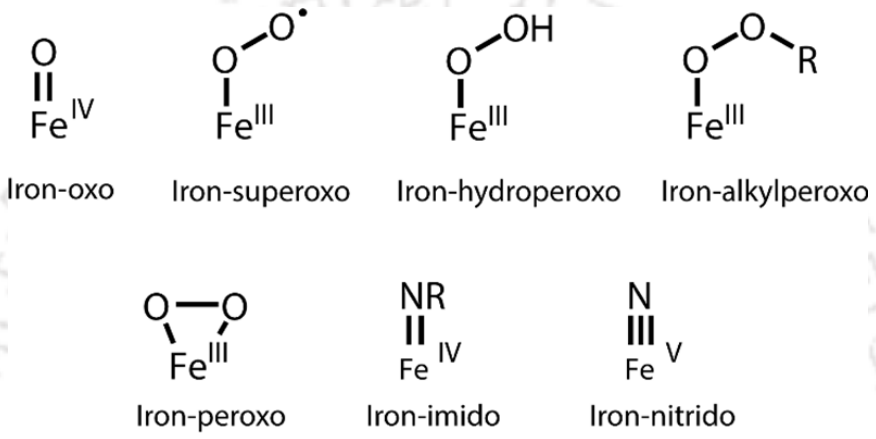

Figure. 1.5. Proposed intermediates of high-valent Iron with Oxygen and Nitrogen.

Numerous non-heme metalloenzymes incorporate iron (Fe) metals that play crucial roles in diverse biological functions. Looking at the literature review, many of these systems require synthetic models that can successfully replicate enzyme active sites and their biological reactions. Drawing inspiration from nature, researchers have sought to create model systems that can interact with various oxidants to produce high-valent transient intermediates. These intermediates are then examined in their reactions with different substrates to better understand their mechanisms.[70,71] Challenges encountered in these endeavours include stabilizing and characterizing these transient species, as well as controlling their rapid reaction kinetics studies.

This thesis specifically focuses on synthesizing synthetic models containing transition metal ions like iron, and on generating reactive intermediates through

reactions with suitable oxidants. The study also investigates the kinetics of these reactions with a variety of organic substrates, conducting numerous model reactions and establishing mechanistic insights. Throughout the research described, several reactive intermediates, such as iron(IV)-oxo, iron(IV)-tosylimido, and iron(III)-alkylperoxo were successfully generated and characterized. The stability of these intermediates, along with their reaction kinetics, were key aspects investigated to gain insight into the mechanistic details of various reactions, all conducted under controlled temperature conditions.

Non-heme iron(IV)-oxo

Researchers have proposed that catalytic cycles of several non-heme iron enzymes may involve high-valent iron(IV)-oxo species as crucial oxidants. Several iron(IV)-oxo species have been thoroughly characterized, proving to be significant for model systems.[72-76] The generation of these iron(IV)-oxo intermediates generally requires the addition of external oxidants, such as PhIO, peracetic acid, or hydrogen peroxide, to iron(II) precursors.[77] These intermediates hold significant potential as key oxidants, capable of driving various oxidative transformations.[78] The first non-heme iron(IV)-oxo species was reported by Weighardt and coworkers in 2000.[79] The iron(IV)-oxo species was generated by the ozonolysis of $[Fe^{III}(\text{cyclam-acetate})(CF_3SO_3)]^+$ at lower temperature. The species was characterized using UV-visible spectroscopy and Mössbauer spectroscopy. Similarly another iron(IV)-oxo species $[Fe^{IV}(O)(TMC)(CH_3CN)]^{2+}$ was reported by Nam and coworkers. They used PhIO as an external oxidant at lower temperature (233 K) to generate the species.

While axially & equatorially-bound sulfur ligands are crucial in numerous nonheme metalloenzymes, there remains a gap in understanding their influence on the structure and reactivity of iron(IV)-oxo cores. These iron(IV)-oxo species are

critical intermediates in enzymes and are thought to drive a significant portion of oxygen atom transfer reactions in biological systems. Although significant efforts have been made, the generation of an iron(IV)-oxo porphyrin complex featuring a thiolate ligand has not yet been reported. In contrast, several nonheme iron complexes have been documented to include a thiolate or thioether group as part of their ligand structure. One early example is the $[Fe^{IV}(O)(TMCS)]^{+}$ complex, where TMCS stands for 1-mercaptoethyl-4,8,11-trimethyl-1,4,8,11-tetraaza-cyclotetradecane. This species was characterized using various spectroscopic methods like UV-visible, resonance Raman, and Mössbauer spectroscopic techniques, and its crystal structure coordinates were determined.[80] The reaction of $[Fe^{IV}(O)(TMCS)]^{+}$ with 9,10-dehydroanthracene (DHA) demonstrated a hydrogen atom abstraction step, exhibiting a substantial kinetic isotope effect (KIE) of 80 when hydrogen atoms in the substrate were replaced with deuterium.[81] This observation suggested that the high KIE value may be attributed to the electron-donating properties of the axial thiolate ligand, which could facilitate significant quantum chemical tunnelling.

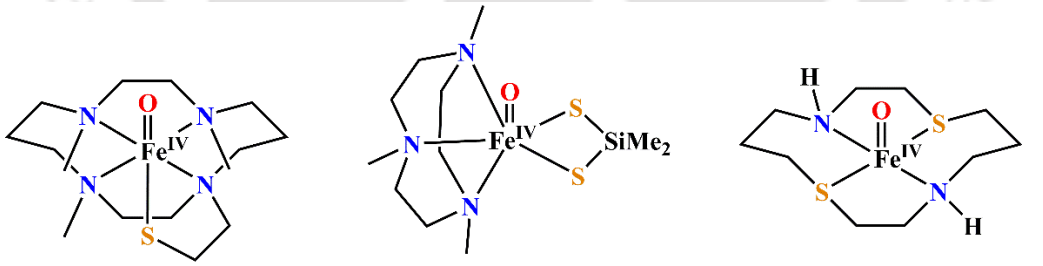

$[Fe^{IV}(O)(Me_3TACN)\text{-}(S_2SiMe_2)]^{+}$ $[Fe^{IV}(O)(Me_3TACN)\text{-}(S_2SiMe_2)]^{2+}$ $[(Dithiacyclam)Fe^{IV}(O)]^{2+}$

Figure. 1.6. Examples of Biomimetic Sulfur-Ligated Iron(IV)-Oxo Models.

Synthesizing biomimetic heme and nonheme iron(IV)-oxo complexes with thiolate ligands, whether axial or equatorial, remains a significant challenge. Consequently, research efforts in this area have pivoted towards neutral sulfur ligands,

specifically thioethers, resulting in the characterization of stable structures for several complexes. While thioethers differ in oxidation state and overall charge from thiolates, potentially leading to quantum mechanical distinctions between the two types of complexes, they are expected to exhibit similar stereochemical interactions. These investigations have spurred biomimetic studies focusing on sulfur-ligated iron(II) complexes as models for thiol dioxygenases found in nature. However, none of these studies have successfully trapped an iron(IV)-oxo species.[82-87] More recently, researchers reported a nonheme iron(IV)-oxo complex featuring an equatorial sulfur ligand, specifically $[Fe^{IV}(O)(Me_3TACN)(S_2Si(CH_3)_2)]$, where Me_3TACN represents 1,4,7-trimethyl 1,4,7-triazacyclononane.[88] The reactivity studies and rate measurements could not be performed due to the thermal instability of the complex. Subsequent work by Ray and colleagues focused on another iron(IV)-oxo complex incorporating a sulfur-containing cyclam ligand, $[Fe^{IV}(O)(dithiacyclam)(CH_3CN)]^{2+}$, where dithiacyclam denotes 1,8-dithia-4,11-diazacyclotetradecane.[89] This system features two sulfur atoms coordinated in the equatorial plane of the iron(IV)-oxo species. The authors suggested that placing sulfur groups in the equatorial position weakens the Fe-O bond and enhances the oxidative reactivity, accompanied by a reduced deuterium kinetic isotope effect. These findings contrast sharply with earlier studies on $[Fe^{IV}(O)(TMCS)]^{+}$ species.[80] Additionally, Kaur and Mandal conducted a thorough computational study to examine the effect of equatorial sulfur substitution on the C-H activation reactivity of iron(IV)-oxo cyclam complexes. Their findings indicate that incorporating sulfur atoms into the ligand scaffold enhances reactivity successively across the series $N_4 < N_3S < S_2N_2 < S_3N < S_4$.[90]

Non-heme iron(IV)-tosylimido

While there is considerable amount of research on high-valent iron-oxygen intermediates, there are relatively few studies on their isoelectronic analogues. Iron complexes featuring terminal nitrido or imido ligands represent some well-investigated systems in this regard. These complexes generally involve iron in higher oxidation states, such as +4, +5, and +6.[91,92] Non-heme iron(V)-nitrido and iron(VI)-nitrido complexes were synthesized using singlet photoelectrochemical methods by Weighart and colleagues, with a trimethyl cyclam acetate ligand framework supporting the complexes.[91,92] In 2000, Lee and colleagues reported the first iron(IV)-imido species, $[Fe_4(\mu_3\text{-}N\textit{t}Bu)_4]$. This species adopts a structure reminiscent of a cubane, where the iron(IV) center is situated at one of its vertices.[93] Subsequently, iron(IV)-imido complexes have been reported using various ligand frameworks.[94-104] These high-valent iron-nitride and imide complexes serve as potent oxidants and play a crucial role in catalyzing amination reactions similar to their isolobal analogues. In recent years, several research groups have explored the reactivity of these metal nitrides and amides in processes such as the aziridination of various alkenes and the aminidation of alkanes using iminoiodane.[94-104] For example, researchers performed a comparative study using the pentadentate N4Py ligand (N,N-bis(2-pyridylmethyl)-N-bis(2-pyridyl)methylamine), which acts as a fundamental ligand framework.[104,105] This ligand was the first system to stabilize both high-valent iron(IV)-oxo and -imido species at ambient temperatures. It was found that iron(IV)-oxo and iron(IV)-imido oxidants exhibit distinct reaction pathways toward substrates. Iron(IV)-oxo typically reacts via direct oxygen atom transfer, illustrated by its reaction with thioanisole. In contrast, iron(IV)-imido proceeds through electron transfer mechanisms. Additionally, Costas et al. reported two octahedral iron(IV)-imido complexes utilizing the ligand frameworks $MePy_2TACN$ (N-methyl-N,N-bis(2-

picolyl)-1,4,7-triazacyclononane) and $Me_2(CHPy_2)TACN$ (1-(di(2-pyridyl)methyl)-4,7-dimethyl-1,4,7-triazacyclononane).[106] Furthermore, our research group extensively investigated the comparative reactivity of iron(IV)-oxo and iron(IV)-imido complexes using the BnTPeN ligand framework (N-Benzyl-N,N,N-tris(pyridine-2-ylmethyl)ethane-1,2-diamine).[107]

Non-heme iron(III)-alkylperoxo

Iron(III)-hydroperoxides and alkylperoxides are known to be the active oxidants in various metalloenzymes. These complexes are known for their sluggish reactivity with organic substrates.[108-113] This may be due to the in-situ formation of Fe^{IV}=O complexes following the homolytic cleavage of O-O bonds. Fe^{IV}=O complexes are known for their reactivity in electrophilic oxidation reactions. However, there have been limited reports indicating that Fe^{III}-OOH intermediates can also exhibit reactivity towards organic transformations.[114-125] The exact mechanisms underlying the reactivity of Fe(III)-OOR complexes are not well-understood, largely due to their thermal instability. Kinetic studies of these species are often inconclusive because of their tendency to engage in competitive bifurcated reaction pathways. In recent decades, reports have indicated occurrences of both homolytic and heterolytic O-O bond cleavage processes.[126-131] The spin state of the metal center is recognized as a critical factor influencing the reaction pathway, as it modulates the strength of both the Fe-O and O-O bonds.[132-134] Quantum chemical calculations have indicated the cleavage of Fe-O bond for high-spin Fe(III)-OOH/R species. Whereas low-spin Fe(III)-OOH/R complexes generally undergo O-O homolytic cleavage. But, not much have been investigated upon the reactivity towards the organic substrates for these species.[135-140]

Scope and aim of the thesis

In the past decade, there has been a growing emphasis on gaining mechanistic insights into the reactivity of high-valent metal intermediates in oxidation reactions, particularly within the field of bio-inorganic chemistry. Minor adjustments in both the primary and secondary coordination environments can result in significant alterations in the stability, spin states, reactivity, and structural characteristics of these synthetic model systems. This thesis provides a thorough investigation into the high-valent non-heme iron metalloenzymes and adds to its huge literature database. In this thesis, we have tried to study the role of sulfur ligation towards the stability and oxidative reactivity of various high-valent iron-oxygen and iron-nitrogen intermediates. We have prepared a series of pentadentate N4S ligand backbones and their iron(II) complexes have been prepared, where it was seen sulfur coordinates equatorially to iron in all the systems. Chapter II covers the utilization of reagents, solvents, oxidants, and synthetic procedures involving various ligand frameworks and metal complexes. Additionally, it discusses their spectroscopic characterizations. Chapter III elaborates on the role of equatorially ligated sulfur on the oxidative reactivity of iron(IV)-oxo complexes. Where the incorporation of sulfur resulted in an enhancement of reaction rates in both sulfoxidation and C-H bond activation reactions. Also, we have observed a change in reaction pathway upon sulfur ligation in both sulfoxidation as well as C-H bond activation reactions. Chapter IV provides the first experimental characterization of a sulfur ligated iron(IV)-tosylimido complex. Its oxidative reactivity was also investigated in sulfoxidation as well as C-H bond activation reactions. Chapter V presents the characterization of a sulfur ligated iron(III)-alkylperoxide complex, where its reactivity has been studied in oxygen atom transfer and aldehyde deformylation reactions.

References

1. Holm, R. H.; Kennepohl, P.; Solomon, E. I., *Chem. Rev.* **1996,** *96*, 2239-2314.
2. Lippard, S. J.; Berg, J. M., *Principles of Bioinorganic Chemistry*. University, Science Books: Mill Valley, CA, **1994**, 411.
3. Kovacs, J. A., *Chem. Rev*. **2004**, *104*, 825-848.
4. Solomon, E. I.; Brunold, T. C.; Davis, M. I.; Kemsley, J. N.; Lee, S.-K.; Lehnert, N.; Neese, F.; Skulan, A. J.; Yange, Y.-S.; Zhou, J., *Chem. Rev*. **2000**, *100*, 235-349.
5. Kennepohl, P.; Neese, F.; Schweitzer, D.; Jackson, H. L.; Kovacs, J. A.; Solomon, E. I., *Inorg. Chem*. **2005**, *44*, 1826-1836.
6. Holm, R. H.; Kennepohl, P.; Solomon, E. I., *Chem. Rev*. **1996**, *96*, 2239-2314.
7. Costas, M.; Mehn, M. P.; Jensen, M. P.; Que, L., Jr., *Chem. Rev*. **2004**,*104*, 939-986.
8. Yeh, A. P.; Hu, Y.; Jenney, F. E., Jr.; Adams, M. W. W.; Rees, D. C., *Biochemistry*. **2000**, *39*, 2499-2508.
9. Coelho, A. V.; Matias, P.; Fulop, V.; Thompson, A.; Gonzalez, A.; Carrondo, M. A., *J. Biol. Inorg. Chem*. **1997**, *7*, 680-689.
10. 9. Huang, W.; Jia, J.; Cummings, J.; Nelson, M. J.; Schneider, G.; Lindqvist, Y., *Structure*. **1997**, *5*, 691-699.
11. 10. Nagashima, S.; Nakasako, M.; Naoshi, D.; Tsujimura, M.; Takio, K.; Odaka, M.; Kamiya, N.; Endo, I., *Nat. Struct. Biol*. **1998**, *5*, 347-351.
12. Becker, A.; Schlichting, I.; Kabsch, W.; Groche, D.; Schultz, S.; Wagner, A. F., *Nat. Struct. Biol*. **1998**, *12*, 1053-1058.
13. *Cytochrome P450: Structure, Mechanism, and Biochemistry*, 3rd ed. (Ed.: P. R. Ortiz de Montellano), Kluwer Academic/Plenum Publishers, New York, **2005**.

14. J. T. Groves, *J. Chem. Ed*. **1985**, *62*, 928-931.
15. J. T. Groves, Y.-Z. Han, *In Cytochrome P-450: Structure, Mechanism and Biochemistry*, P. R. Oritz de Montellano, Ed. Plenum Press, New York, **1995**, pp. 3-48.
16. F. Ogliaro, S. P. de Visser, S. Shaik, *J. Inorg. Biochem*. **2002**, *91*, 554-567.
17. D. L. Harris, G. H. Loew, *J. Am. Chem. Soc*. **1998**, *120*, 8941-8948.
18. D. L. Harris, G. H. Loew, *J. Am. Chem. Soc*. **1996**, *118*, 6377-6387.
19. J. Rittle and M. T. Green, *Science* **2010**, *330*, 933–937.
20. M. T. Green, J. H. Dawson, H. B. Gray, *Science* **2004**, *304*, 1653-1656.
21. J. T. Groves, In *Cytochrome P450: Structure, Mechanism, and Biochemistry*; 3rd ed.; P. R. Ortiz de Montellano, Ed.; Plenum Publishers: New York, **2005**, pp. 1-43.
22. M. Newcomb, M.-H. Le Tadic, D. A. Putt, P. F. Hollenberg, *J. Am. Chem. Soc*. **1995**, *777*, 3312-3313.
23. V. W. Dowry, K. U. Ingold, *J. Am. Chem. Soc*. **1991**, *113*, 5699-5707.
24. M. Filatov, N. Harris, S. Shaik, *Angew. Chem. Int. Ed. Engl.* **1999**, *38*, 3510-3512.
25. F. Ogliaro, N. Harris, S. Cohen, M. Filatov, S. P. deVisser, S. Shaik, *J. Am. Chem. Soc*. **2000**, *122*, 8977-8989.
26. J. A. Kovacs, *Chem. Rev*. **2004**, *104*, 825–848.
27. C. Mathe, T. A. Mattioli, O. Horner, M. Lombard, J. M. Latour, M. Fontecave, V. Niviere, *J. Am. Chem. Soc*. **2002**, *124*, 4966–4967.
28. V. Niviere, M. Asso, C. O. Weill, M. Lombard, B. Guigliarelli, V. Favaudon, C. Houe′e-Levin, *Biochemistry*, **2004**, *43*, 808–818.
29. A. P. Yeh, Y. Hu, F. E. Jenney Jr, M. W. W. Adams, D. C. Rees, *Biochemistry*. **2000**, *39*, 2499-2508.

30. A. V. Coelho, P. Matias, V. Fulop, A. Thompson, A. Gonzalez, M. A. Carrondo, *J. Biol. Inorg. Chem.* **1997**, *7*, 680-689.
31. K. Auclair, P. Moenne-Loccoz, P. R. Ortiz de Montellano, *J. Am. Chem. Soc*. **2001**, *123*, 4877–4885.
32. J. -U. Rohde, J. H. In, M. H. Lim, W. W. Brennessel, M. R. Bukowski, A. Stubna, E. Munck, W. Nam, L. Que, Jr. *Science*. **2003**, *299*, 1037–1039.
33. C. R. Simmons, Q. Liu, Q. Q. Huang, Q. Hao, T. P. Begley, P. A. Karplus, M. H. Stipanuk, *J. Biol. Chem.* **2006,** *281*, 18723-18733.
34. S. Ye, X. Wu, L. Wei, D. M. Tang, P. Sun, M. Bartlam, Z. H. Rao, *J. Biol. Chem.* **2007,** 282, (5), 3391-3402.
35. C. A. Joseph, M. J. Maroney, *Chem. Commun*. **2007**, *32*. 3338–3349.
36. S. Aluri, S. P. de Visser, *J. Am. Chem. Soc.* **2007**, *129*, 14846–14847.
37. E. P. Tchesnokov, A. S. Faponle, C. G. Davies, M. G. Quesne, R. Turner, M. Fellner, R. J. Souness, S. M. Wilbanks, S. P. de Visser, G. N. Jameson, *Chem. Commun.* **2016**, *52*, 8814–8817.
38. G. Villar-Acevedo, P. Lugo-Mas, M. N. Blakely, J. A. Rees, A. S. Ganas, E. M. Hanada, W. Kaminsky and J. A. Kovacs, *J. Am. Chem. Soc*, **2017**, *139*, 119–129.
39. D. Kumar, W. Thiel, S. P. de Visser, *J. Am. Chem. Soc.* **2011**, *133*, 3869–3882.
40. J. E. Baldwin, E. Abraham, *Nat. Prod. Rep*. **1988**, *5*, 129–145.
41. C. P. Pang, *Biochem. J*. **1984**, *222*, 789–795.
42. I. Borovok, O. Landman, R. Kreisberg-Zakarin, Y. Aharonowitz, G. Cohen, *Biochemistry*. **1996**, *35*, 1981 -1987.
43. P. L. Roach, I. J. Clifton, C. M. Hensgens, N. Shibata, C. J. Schofield, J. Hajdu, J. E. Baldwin, *Nature.* **1997**, *387*, 827–830.
44. W. A. Schenk, *Angew. Chem. Int. Ed.* **2000**, *39*, 3409–3411.

45. J. A. Kovacs, L. M. Brines, *Acc. Chem. Res*. **2007**, *40*, 501–509.
46. J. A. Kovacs, L. M. Brines. *J. Am. Chem. Soc*. **2007**, *129*, 7427–7438.
47. E. I. Solomon, *Chem. Rev*. **2000**, *100*, 235–350.
48. E. G. Kovaleva, J. D. Lipscomb, *Nature Chem. Biol.* **2008**, *4*, 186–193.
49. L. C. Blasiak, F. H. Vaillancourt, C. T. Walsh, C. L. Drennan, *Nature* **2006**, *440*,368–371.
50. J. Rittle, M. T. Green, *Science* **2010**, *330*, 933–937.
51. E. G. Kovaleva, J. D. Lipscomb, *Science* **2007**, *316*, 453–457.
52. A. Karlsson, *Science* **2003**, *299*, 1039–1042.
53. R. M.Cicchillo, *Nature* **2009**, *459*, 871–874.
54. M. J. Park, J. Lee, Y. Suh, J. Kim, W. Nam, *J. Am. Chem. Soc.* **2006**, *128*, 2630–2634.
55. Y. M. Kim, K.−B. Cho, J. Cho, B. Wang, C. Li, S. Shaik, W. Nam, *J. Am. Chem. Soc.* **2013**, *135*, 8838−8841.
56. L. V. Liu, S. Hong, J. Cho, W. Nam, E. I. Solomon, *J. Am. Chem. Soc.* **2013,** *135*, 3286−3299.
57. H. So, Y. J. Park, K.−B. Cho, Y.−M. Lee, M. S. Seo, J. Cho, R. Sarangi, W. Nam, *J. Am. Chem. Soc.* **2014**, *136*, 12229−12232.
58. J. Annaraj, Y. Suh, M. S. Seo, S. O. Kim, W. Nam, *Chem. Commun*. **2005**, 4529–4531.
59. J. Annaraj, J. Cho, Y.–M. Lee, S. Y. Kim, R. Latifi, S. P. de Visser, W. Nam, *Angew. Chem. Int. Ed*. **2009**, *48*, 4150–4153.
60. M. S. Seo, J. Y. Kim, J. Annaraj, Y. Kim, Y.–M. Lee, S.–J. Kim, J. Kim, W. Nam, *Angew. Chem. Int. Ed.* **2007**, *46*, 377–380.
61. R. A. Geiger, S. Chattopadhyay, V. W. Day, T. A. Jackson, *Dalton Trans.* **2011**, *40*, 1707–1715.

62. Y. Goto, S. Wada, I. Morishima, Y. Watanabe, *J. Inorg. Biochem.* **1998**, *69*, 241–247.
63. J. Cho, R. Sarangi, J. Annaraj, S. Y. Kim, M. Kubo, T. Ogura, E. I. Solomon, W. Nam, *Nat. Chem*. **2009**, *1*, 568–572.
64. E. I. Solomon, T. C. Brunold, M. I. Davis, J. N. Kemsley, S.–K. Lee, N. Lehnert, F. Neese, A. J. Skulan, Y.–S. Yang, J. Zhou, *Chem. Rev.* **2000**, *100*, 235–349.
65. M. Costas, M. P. Mehn, M. P.Jensen, L. Que Jr., *Chem. Rev.* **2004,** *104*, 939–986.
66. R. P. Hausinger, *Crit. Rev. Biochem. Mol. Biol*. **2004**, *39*, 21–68.
67. E. G. Kovaleva, J. D. Lipscomb, *Nat. Chem. Biol*. **2008**, *4*, 186–193.
68. C. Loenarz, C. J. Schofield, *Nat. Chem. Biol*. **2008**, *4*, 152–156.
69. W. Nam, *Acc. Chem. Res*. **2007**, *40*, 522–531.
70. J.-J. Girerd, F. Banse, A. J. Simaan, *Struct. Bonding* **2000**, *97*, 145−177.
71. J.-U. Rohde, M. R. Bukowski, L. Que, Jr., *Curr. Op. Chem. Biol.* **2003**.
72. C. A. Grapperhaus, B. Mienert, E. Bill, T. Weyhermtiller, K. Wieghardt, *Inorg. Chem*. **2000**, *39*, 5306−5317.
73. J.-U. Rohde, J.-H. In, M. H. Lim, W. W. Brennessel, M. R. Bukowski, A. Stubna, E. Münck, W. Nam, L. Que, Jr., *Science* **2003**, *299*, 1037−1039.
74. M. H. Lim, J.-U. Rohde, A. Stubna, M. R. Bukowski, M. Costas, R. Y. N. Ho, E. Münck, W. Nam, L. Que, Jr., *Proc. Natl. Acad. Sci. USA.* **2003**, *100*, 3665−3670.
75. J. Kaizer, E. J. Klinker, N. Y. Oh, J.-U. Rohde, W. J. Song, A. Stubna, J. Kim, W. Nam, E. Münck, L. Que, Jr., *J. Am. Chem. Soc.* **2004**, *126*, 472-473.
76. V. Balland, M.-F. Chariot, F. Banse, J.-J. Girerd, T. A. Mattioli, E. Bill, J.-F. Bartoli, P. Battioni, D. Mansuy, *Eur. J. Inorg. Chem.* **2004**, 301-308.

77. J.-U. Rohde, L. Que, Jr., *Angew. Chem. Int. Ed.* **2005**, *44*, 2255-2258.

78. J. T. Groves, J. T. In *Cytochrome P450: Structure, Mechanism, and Biochemistry*; 3rd ed.; Ortiz de Montellano, P. R., Ed.; Plenum Publishers: New York, **2005**, p 1-43.

79. C. A. Grapperhaus, B. Mienert, E. Bill, T. Weyhermüller, K. Wieghardt, *Inorg. Chem.* **2000**, *39*, 5306-5317.

80. M. R. Bukowski, K. D. Koehntop, A. Stubna, E. L. Bominaar, J. A. Halfen, E. Münck, W. Nam, L. Que Jr. *Science*. **2005**, *310*, 1000–1002.

81. J. E. M. N. Klein, D. Mandal, W. M. Ching, D. Mallick, L. Que, S. Shaik. *J. Am. Chem. Soc*. **2017**, *139*, 18705–18713.

82. Y. Jiang, L. R. Widger, G. D. Kasper, M. A. Siegler, D. P. Goldberg. *J. Am. Chem. Soc*. **2010**, *132*, 12214–12215.

83. A. R. McDonald, M. R. Bukowski, E. R. Farquhar, T. A. Jackson, K. D. Koehntop, M. S. Seo, R. F. De Hont, A. Stubna, J. A. Halfen, E. Munck, W. Nam, L. Que Jr. *J. Am. Chem. Soc*. **2010**, *132*, 17118-17129.

84. M. Sallmann, S. Kumar, P. Chernev, J. Nehrkorn, A. Schnegg, D. Kumar, H. Dau, C. Limberg, S. P. de Visser. *Chem. Eur. J*. **2015**, *21*, 7470–7479.

85. K. Anandababu, R. Ramasubramanian, H. Wadepohl, P. Comba, N. J. Britto, M. Jaccob, R. Mayilmurugan. *Chem. Eur. J*. **2019**, *25*, 9540-9547.

86. G. Villar-Acevedo, P. Lugo-Mas, M. N. Blakely, J. A. Rees, A. S. Ganas, E. M. Hanada, W. Kaminsky, J. A. Kovacs. *J. Am. Chem. Soc*. **2017**, *139*, 119−129.

87. A. A. Fischer, J. R. Miller, R. J. Jodts, D. M. Ekanayake, S. V. Lindeman, T. C. Brunold, A. T. Fiedler. *Inorg. Chem*. **2019**, *58*, 16487−16499.

88. J. B. Gordon, A. C. Vilbert, I. M. DiMucci, S. N. MacMillan, K. M. Lancaster, P. Moënne-Loccoz, D. P. Goldberg. *J. Am. Chem. Soc*. **2019**, *141*, 17533–17547.

89. J. Deutscher, P. Gerschel, K. Warm, U. Kuhlmann, S. Mebs, M. Haumann, H. Dau, P. Hildebrandt, U. P. Apfel, K. Ray. *Chem. Commun*. **2021**, *57*, 2947–2950.

90. L. Kaur, D. Mandal. *Inorg. Chem*. **2022**, *61*, 14582–14590.

91. T. A. Betley, J. C. Peters. *J. Am. Chem. Soc.* **2004**, *126*, 6252–6254.

92. N. Aliaga-Alcalde, S. D. George, B. Mienert, E. Bill, K. Wieghardt, F. Neese. *Angew. Chem. Int. Ed.* **2005**, *44*, 2908–2912.

93. A. K. Verma, T. N. Nazif, C. Achim, S. C. Lee, *J. Am. Chem. Soc.* **2000**, *122*, 11013–11014.

94. C. M. Thomas, N. P. Mankad, J. C. Peters, *J. Am. Chem. Soc.* **2006**, *128*, 4956–4957.

95. J. F. Berry, E. Bill, E. Bothe, S. D. George, B. Mienert, F. Neese, K. Wieghardt, *Science* **2006**, *312*, 1937–1941.

96. P. Comba, C. Lang, C. Lopez de Laorden, A. Muruganatham, G. Rajaraman, H. Wadepohl, M. Zajaczkowski, *Chem. Eur. J*. **2008**, *14*, 5313–5328.

97. K. L. Klotz, L. M. Slominski, M. E. Riemer, J. A. Phillips, J. A. Halfen, *Inorg. Chem.* **2009**, *48*, 801–803.

98. J. J. Scepaniak, J. A. Young, R. P. Bontchev, J. M. Smith, *Angew. Chem. Int. Ed*. **2009**, *48*, 3158–3160.

99. P. Leeladee, G. N. L. Jameson, M. A. Siegler, D. Kumar, S. P. de Visser, D. P. Goldberg, *Inorg. Chem*. **2013**, *52*, 4668–4682.

100. M. J. Zdilla, M. M. Abu-Omar, *J. Am. Chem. Soc*. **2006**, *128*, 16971-16979.

101. S. Kundu, E. Miceli, E. Farquhar, F. F. Pfaff, U. Kuhlmann, P. Hildebrandt, B. Braun, C. Greco, K. Ray, *J. Am. Chem. Soc.* **2012**, *134*, 14710−14713.

102. J. W. W. Chang, P. W. H. Chan, *Angew. Chem. Int. Ed.* **2008**, *47*, 1138–1140.

103. E. T. Hennessy, T. A. Betley, *Science* **2013**, *340*, 591–595.

104. A. K. Vardhaman, P. Barman, S. Kumar, C. V. Sastri, D. Kumar and S. P. de visser, *Angew. Chem. Int. Ed.* **2013**, *52*, 12288–12292.

105. S. Kumar, A. S. Faponle, P. Barman, A. K. Vardhaman, C. V. Sastri, D. Kumar and S. P. de Visser, *J. Am. Chem. Soc*., **2014**, *136*, 17102.

106. G. Sabenya, I. Gamba, L. Gómez, M. Clémancey, J. R. Frisch, E. J. Klinker, G. Blondin, S. Torelli, L. Jr. Que, V. Martin-Diaconescu, J. M. Latour, *Chem. Sci*. **2019**, *10*, 9513−9529.

107. G. Mukherjee, F. G. CantúReinhard, U. K. Bagha, C. V. Sastri, S. P. de Visser, *Dalton Trans*. **2020**, *49*, 5921−5931.

108. M. S. Seo, T. Kamachi, T. Kouno, K. Murata, M. J. Park, K. Yoshizawa, W. Nam, *Angew. Chem. Int. Ed*. **2007**, *46*, 2291-2294

109. C. Würtele, E. Gaoutchenova, K. Harms, M. C. Holthausen, J. Sundermeyer, S. Schindler, *Angew. Chem. Int. Ed.* **2006**, *45*, 3867-3869.

110. S. Itoh, *Acc. Chem. Res.* **2015**, *48*, 2066-2074.

111. J. J. Liu, D. E. Diaz, D. A. Quist, K. D. Karlin, *Isr. J. Chem.* **2016**, *56*, 738-755.

112. C. E. Elwell, N. L. Gagnon, B. D. Neisen, D. Dhar, A. D. Spaeth, G. M. Yee, W. B. Tolman, *Chem. Rev.* **2017**, *117*, 2059-2107.

113. J. K. Satpathy, R. Y. Yadav, U. K. Bagha, D. Kumar, C. V. Sastri, S. P. de Visser, *Inorg. Chem*. **2024**, *63*, 6752-6766.

114. T. Ogihara, S. Hikichi, M. Akita, T. Uchida, T. Kitigawa, Y. Moro-oka, *Inorg. Chem. Acta*, **2000**, *297*, 162-170.

115. A. P. Sobolev, D. E. Babushkin, E. P. Talsi, *J. Mol. Catal. A*. **2000**, *159*, 233-245.

116. J. Kim, Y. Zang, M. Costas, R. G. Harrison, E. C. Wilkinson, L. Que, Jr., *J. Biol. Inorg. Chem*. **2001**, *6*, 275-284.

117. M. P. Jensen, S. J. Lange, M. P. Mehn, E. L. Que, L. Que, Jr. *J. Am. Chem. Soc*. **2003**, *125*, 2113-2128.

118. N. Lehnert, K. Fujisawa, E. I. Solomon, *Inorg. Chem*. **2003**, *42*, 469-481.

119. J.-U. Rohde, S. Torelli, X. Shan, M. H. Lim, E. J. Klinker, J. Kaizer, K. Chen, W. Nam, L. Que, Jr. *J. Am. Chem. Soc*. **2004**, *126*, 16750-16761.

120. M. P. Jensen, M. Costas, R. Y. N. Ho, J. Kaizer, A. Mariata i Payeras, E. Münck, L. Que, Jr., J.-U. Rohde, A. Stubna, *J. Am. Chem. Soc*. **2005**, *127*, 10512-10525.

121. T. K. Paine, M. Costas, J. Kaizer, L. Que, Jr. *J. Biol. Inorg. Chem*. **2006**, *11*, 272-276.

122. J. Bautz, P. Comba, L. Que, Jr. *Inorg. Chem*, **2006**, *45*, 7077-7082.

123. X. Shan, J.-U. Rohde, K. D. Koehntop, Y. Zhou, M. R. Bukowski, M. Costas, K. Fujisawa, L. Que, Jr., *Inorg. Chem*. **2007**, *46*, 8410-8417.

124. F. Namuswe, G. D. Kasper, A. A. N. Sarjeant, T. Hayashi, C. M. Krest, M. T. Green, P.Moënne-Loccoz, D. P. Goldberg, *J. Am. Chem. Soc*. **2008**, *130*, 14189-14200.

125. F. Namuswe, T. Hayashi, Y. Jiang, G. D. Kasper, A. A. N. Sarjeant, P. Moënne-Loccoz, D. P. Goldberg, *J. Am. Chem. Soc*. **2010**, *132*, 157-167.

126. S. Ménage, E. C. Wilkinson, L. Que, Jr., M. Fontecave, *Angew. Chem. Int. Ed*. **1995**, *34*, 203-205.

127. R. Y. Ho, G. Roelfes, B. L. Feringa, L. Que, *J. Am. Chem. Soc*. **1999**, *121*, 264-265.

128. A. Bassan, M. R. Blomberg, P. E. Siegbahn, L. Que, Jr. *J. Am. Chem. Soc*. **2002**, *124*, 11056-11063.

129. W. N. Oloo, A. J. Fielding, L. Que, Jr. *J. Am. Chem. Soc*. **2013**, *135*, 6438-6441.

130. S. Bang, S. Park, Y.-M. Lee, S. Hong, K.-B. Cho, W. Nam, *Angew. Chem. Int. Ed*. **2014**, *53*, 7843-7847.

131. I. Ghosh, S. Banerjee, S, Paul, T. Corona, T. K. Paine, *Angew. Chem. Int. Ed*. **2019**, *58*, 12534-12539.

132. J. J. Girerd, F. Banse, A. J. Simaan, *Struct. Bonding (Berlin)*. **2000**, *97*, 145-177.

133. M. P. Jensen, A. Mariata i Payeras, A. T. Fiedler, M. Costas, J. Kaizer, A. Stubna, E. Münck, L. Que, Jr. *Inorg. Chem*. **2007**, *46*, 2398-2408.

134. J. Kaizer, M. Costas, L. Que, Jr., *Angew. Chem. Int. Ed*. **2003**, *42*, 3671-3673.

135. N. Lehnert, R. Y. N. Ho, L. Que, Jr., E. I. Solomon, *J. Am. Chem. Soc*. **2001**, *123*, 8271-8290.

136. N. Lehnert, R. Y. N. Ho, L. Que, Jr., E. I. Solomon, *J. Am. Chem. Soc*. **2001**, *123*, 12802-12816.

137. L. R. Widger, Y. Jiang, A. C. McQuilken, T. Yang, M. A. Siegler, H. Matsumura, P. Moënne-Loccoz, D. Kumar, S. P. de Visser, D. P. Goldberg, *Dalton Trans*. **2014**, *43*, 7522-7532.

138. Y. Zang, J. Kim, Y. Dong, E. C. Wilkinson, E. H. Appelman, L. Que, Jr., *J. Am. Chem. Soc*. **1997**, *119*, 4197-4205.

139. M. R. Bukowski, H. L. Halfen, T. A. van den Berg, J. A. Halfen, L. Que, Jr., *Angew. Chem. Int. Ed*. **2005**, *44*, 584-587.

140. D. Krishnamurthy, G. D. Kasper, F. Namuswe, W. D. Kerber, A. A. N. Sarjeant, P. Moënne-Loccoz, D. P. Goldberg, *J. Am. Chem. Soc*. **2006**, *128*, 14222-14223.

CHAPTER – II

Synthesis and Characterization, Materials Employed and Methods Adapted

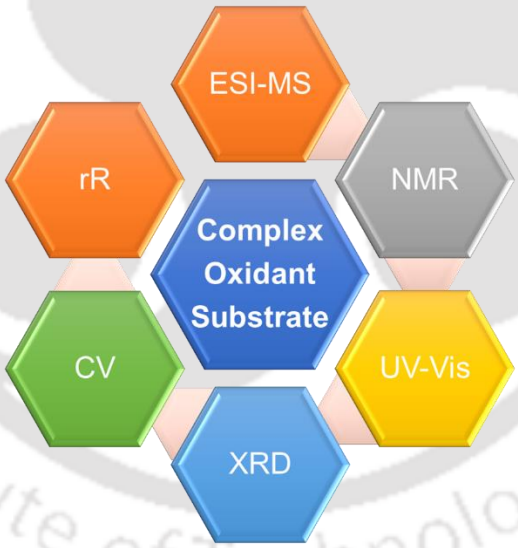

2.1. Introduction

The work presented here stems from a series of meticulously planned experiments with thorough observations. A comprehensive analysis would distinctly categorize each phase of the research into several tasks, including: developing the ligand frameworks, synthesizing the oxidants and substrates (if not commercially available), preparing the metal complexes, generating and stabilizing the metal intermediates, optimizing the reaction conditions, performing a kinetic study, analyzing the products, and finally interpreting and evaluating the results obtained.

Prior to each experiment, appropriate safety protocols were implemented. Extensive examination of the chemical purity is also necessary for perfect experimental outcomes. Below is a detailed discussion of the methods used for the instrumentation, characterization, synthesis, and purification.

2.2. Experimental Section

2.2.1. Solvents

Solvents were dried following published procedures[1] and distilled under argon before use. Acetonitrile (CH_3CN) was dried over Calcium hydride in a solvent still-head distillation apparatus fitted with a condenser on a heating mantle. A similar setup was followed for other solvents like THF and diethyl ether, although they were dried over sodium using benzophenone as an indicator. Solvents were collected from the solvent still-head distillation apparatus into dry glassware through a cannula using vacuum pumps. Glassware were extensively

dried using either flame or kept inside hot oven for prolonged period of time before use.

2.2.2. Oxidants

Generation of the different types of reaction intermediates requires different types of oxidants (such as iodosylbenzene, peracetic acid, oxone, CAN, hydrogen peroxide, (Diacetoxyiodo)benzene, sodium chlorite, *tert*-butyl hydroperoxide, potassium superoxide, etc.) that react with the metal complexes. Some of the oxidants used herewith were purchased commercially while some of them were synthesized using previously reported procedures. The oxidants that were commercially available were (i) (Diacetoxyiodo)benzene ($PhI(OAc)_2$), (Aldrich Chemical Company) (ii) hydrogen peroxide (H_2O_2) (Merck) and (iii) *tert*-butyl hydroperoxide (^tBuOOH) (Aldrich Chemical Company). Oxidant that was synthesized was PhIO, ^{S}PhIO and ^{S}PhINTs.

Synthesis of Iodosylbenzene (PhIO): Iodosylbenzene was prepared by following a well-established literature method.[2] 10 g of finely grounded (iodosobenzene)diacetate was placed in 250 mL beaker, then 100 mL of NaOH solution (3 N) was slowly added for a 5 minutes period with continuous stirring. The lumps were formed instantaneously, which were then grounded for 10-15 minutes with glass rod and the reaction mixture was stirred for another 1 hour to complete the reaction. Next, 100 mL of water was added to the reaction mixture, which was stirred vigorously and filtered using a Büchner funnel. The crude solid iodosylbenzene obtained was then placed back into the beaker and mixed with 200 mL of water. The solid was once again collected using a Büchner funnel, washed with an additional 200 mL of water, and dried under vacuum. Finally, it was triturated in 75 mL of chloroform in a beaker, filtered, dried, and stored in a cool, dark place. Yield: 8 g; m.p. 210 °C (caution: potential explosive).

Synthesis of ^{S}*PhIO:* The synthesis of ^{S}PhIO has been done by following a literature protocol.[3]

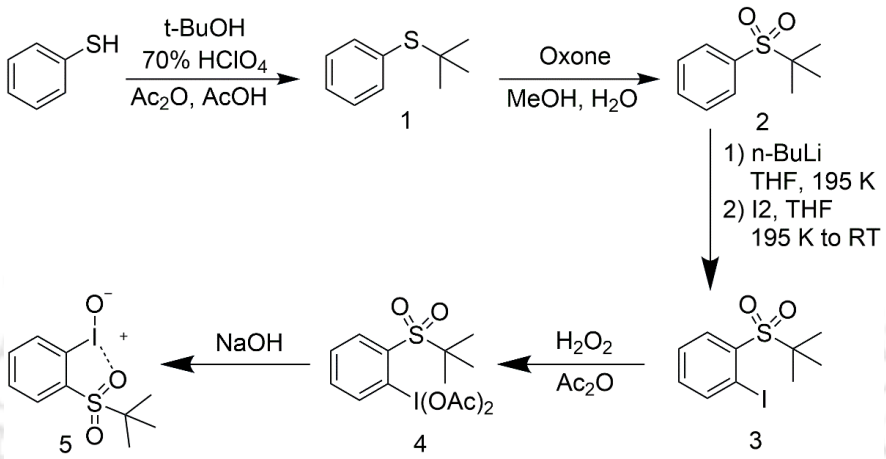

Scheme 1. Synthetic procedure of ^{S}PhIO.

*Synthesis of tert-butyl(phenyl)sulfane (**1**)*: A 250-mL round-bottomed flask was cooled in an ice bath before the addition of acetic acid (10 mL), 70% perchloric acid solution (3.5 mL), and acetic anhydride (6 mL). The mixture was stirred at 0 °C for about 20 minutes. Thiophenol (1.00 equiv), tert-butanol (1.20 equiv), and an additional 15.0 mL of acetic acid were then added. The reaction mixture was then allowed to warm to room temperature (23 °C) and stirred overnight. Once the reaction was complete, the mixture was poured into 100 mL of brine and extracted with diethyl ether (3 x 100 mL). The combined organic layers were washed with saturated sodium bicarbonate solution (until CO_2 evolution stopped) and water (100 mL), and then dried over sodium sulfate. After evaporating the solvent under reduced pressure, the residue was purified by silica gel chromatography using a mobile phase of 10% ethyl acetate in hexanes. This process afforded compound **1** as a colorless oil.

^{1}H NMR (δ, 23 °C, $CDCl_3$): 7.61 (d, *J* = 7.1 Hz, 2H), 7.42 (d, *J* = 7.3 Hz, 3H), 1.35 (s, 9H).

*Synthesis of (tert-butylsulfonyl)benzene (**2**):* In a 500-mL round-bottomed flask, tert-butyl(phenyl)sulfane (1 equiv.) was diluted with methanol (100 mL) and cooled to 0 °C using an ice bath. A solution of Oxone® (2.1 equiv.) in water (100 mL) was then added to the reaction mixture in one portion. The mixture was allowed to warm to room temperature (23 °C) and continued stirring for 2 hours. Methanol was subsequently evaporated under reduced pressure. Water (50 mL) was added, and the aqueous phase was extracted with diethyl ether (3 x 50 mL). The combined organic layers were washed with brine and dried over Na_2SO_4. The solvent was removed under reduced pressure, and the residue was purified by silica gel chromatography using a mobile phase of 20% ethyl acetate in hexanes, resulting in compound **2** as a white solid. ^{1}H NMR (δ, 23 °C, $CDCl_3$): 7.95–7.91 (m, 2H), 7.72–7.65 (m, 1H), 7.58 (t, *J* = 7.6 Hz, 2H), 1.38 (s, 9H).

*Synthesis of 2-(tert-butylsulfpnyl)iodobenzene (**3**):* In a 250-mL Schlenk flask, tert-butylsulfonylbenzene (1.00 equiv.) was dissolved in THF (30 mL) and the mixture was cooled to -78 °C. n-BuLi (2.45 M in hexane) (1.42 equiv.) was added dropwise to the solution. The reaction mixture was stirred at -78 °C for 1 hour. Subsequently, a solution of I_2 (1.54 equiv.) in THF (30 mL) was added, and the reaction was allowed to warm to room temperature (23 °C) where it was stirred for 16 hours. The solvent was removed under reduced pressure, and the residue was treated with saturated aqueous NH_4Cl (50 mL) and dichloromethane (50 mL). The layers were separated, and the aqueous layer was further extracted with dichloromethane (2 x 50 mL). The combined organic layers were washed with saturated aqueous $Na_2S_2O_3$ solution and dried over Na_2SO_4. After evaporating the solvent under reduced pressure, the residue was purified by silica gel chromatography using a

mobile phase of 25% ethyl acetate in hexanes, yielding the title compound (**3**) as a white solid.

^{1}H NMR (δ, 23 °C, $CDCl_3$): 8.21 (d, *J* = 7.9 Hz, 1H), 8.06 (d, *J* = 8.0 Hz, 1H), 7.66 (t, *J* = 8.3 Hz, 1H), 7.31–7.22 (m, 1H), 1.34 (s, 9H).

*Synthesis of 2-(tert-butylsulfonyl)diacetoxyiodobenzene (**4**):* In a 10-mL round-bottomed flask, a solution of hydrogen peroxide (30 wt%, 5 mL) and acetic anhydride (20 mL) was prepared and stirred for 4 hours at 40 °C. Subsequently, 2-(tert-butylsulfonyl)iodobenzene (3, 5 g) was added to the reaction mixture, which was then stirred at room temperature (23 °C) for 24 hours. The progress of the reaction was monitored by thin-layer chromatography (using SiO_2 as the stationary phase and an eluent of 20% ethyl acetate in hexanes, resulting in a R_f value of 0.3). After completion, the reaction mixture was concentrated under reduced pressure to yield a white solid, which was used in the subsequent step without further purification.

*Synthesis of 2-(tert-butylsulfonyl)iodosylbenzene (**5**):* The solid 4 (derived from 5 g of compound 3) was treated with 3 N NaOH aqueous solution dropwise under vigorous stirring until the pH exceeded 7. The resulting mixture was stirred for an additional half-hour. The yellow solid product was collected by filtration, washed with diethyl ether, and subsequently dried under reduced pressure to yield compound **5** as a yellow powder.

Synthesis of 2-(tert-butylsulfonyl)(p-toluenesulfonyliminoiodo)benzene: The solid 4 was combined with an ice-chilled solution of p-toluenesulfonamide and excess KOH in 60 mL of dry methanol. Upon mixing, a pale yellowish sludge formed immediately, and the mixture was stirred for 25 minutes. Crushed ice was then added, and the resulting yellow powder was separated by filtration. The isolated

product was washed with water and diethyl ether, followed by drying under reduced pressure to obtain compound **6** as a pale-yellow powder.

2.2.3. Substrates

Most of the chemicals were obtained from Sigma-Aldrich Chemical Company and used as received, unless specified otherwise. Thioanisole (THA) and its para-X derivatives (X = -OMe, -Me, -Cl), benzyl alcohol, fluorene, toluene, 1,4-cyclohexadiene (CHD), and cyclohexanecarboxaldehyde (CCA) were purchased from Aldrich Chemical Company. Triphenylmethane was sourced from Avra Synthesis Pvt. Ltd. 9,10-Dihydroanthracene (DHA), ethylbenzene, and cumene were obtained from TCI Chemicals Pvt. Ltd. $H_2{}^{18}O$ (99.9% pure, enrichment 97.1 atom %) was procured from Berry and Associates (Icon Isotopes). Benzyl alcohol-D7 and ethylbenzene-D10 were purchased from Cambridge Isotope Laboratories, Inc. Other deuterated solvents such as $CDCl_3$, CD_3CN, D_2O, DMSO-D_6, and CD_3OD were acquired from Aldrich Chemical Company. α-D-cyclohexanecarboxaldehyde (α-D-CCA) was purchased from RVL Scientific & Engineering Pvt Ltd.

- *Synthesis of Xanthene-D_2*:

The synthesis and purification procedures were followed from the published literature methods.[4] Xanthene (1.82 g, 10 mmol) was dissolved in DMSO-d_6 (8 mL) containing NaH (1 g) under a nitrogen atmosphere. The reaction mixture was stirred at room temperature for 2 hours and then quenched with D_2O (8 mL). The crude product was filtered and washed thoroughly with water. The resulting solid was purified by silica gel column chromatography using hexane as the eluent, followed by recrystallization from isopropanol.; ^{1}H NMR (500 MHz, $CDCl_3$): δ 7.19 (4H, m), 7.04 (4H, m). The NMR data indicated > 99.9% deuteration.

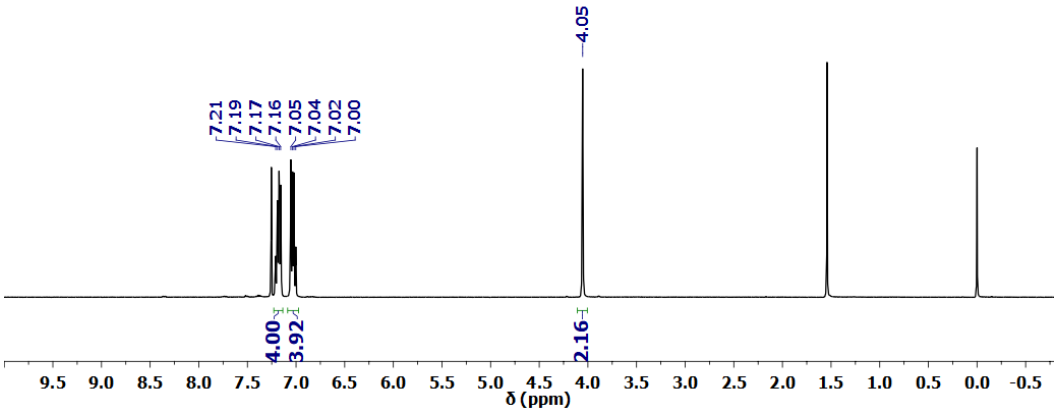

Fig. 2.1. ^{1}H NMR (400 MHz) spectrum of Xanthene in $CDCl_3$ at 298 K.

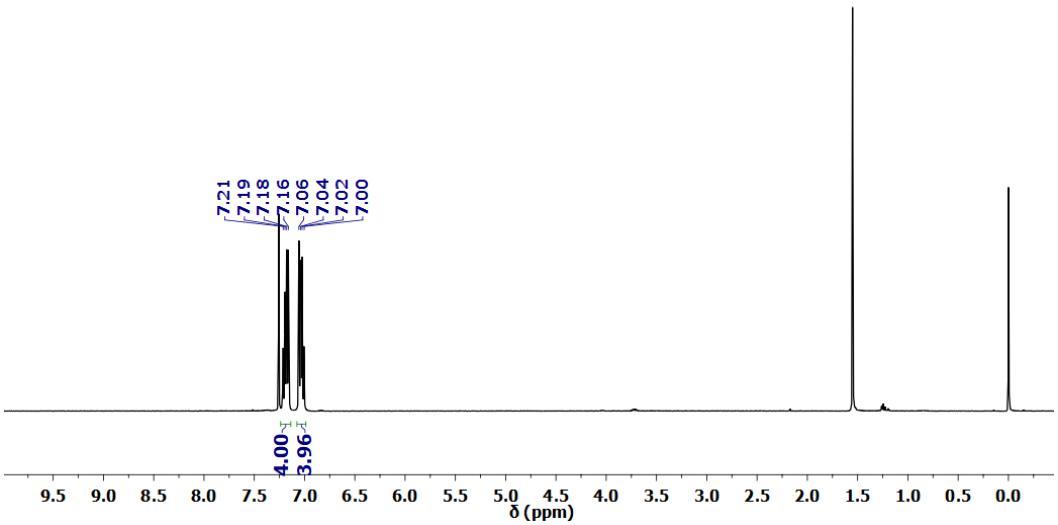

Fig. 2.2. ^{1}H NMR (400 MHz) spectrum of Xanthene-D_2 in $CDCl_3$ at 298 K.

2.2.4. Ligands

Scheme 2.2. Ligand systems used and discussed throughout.

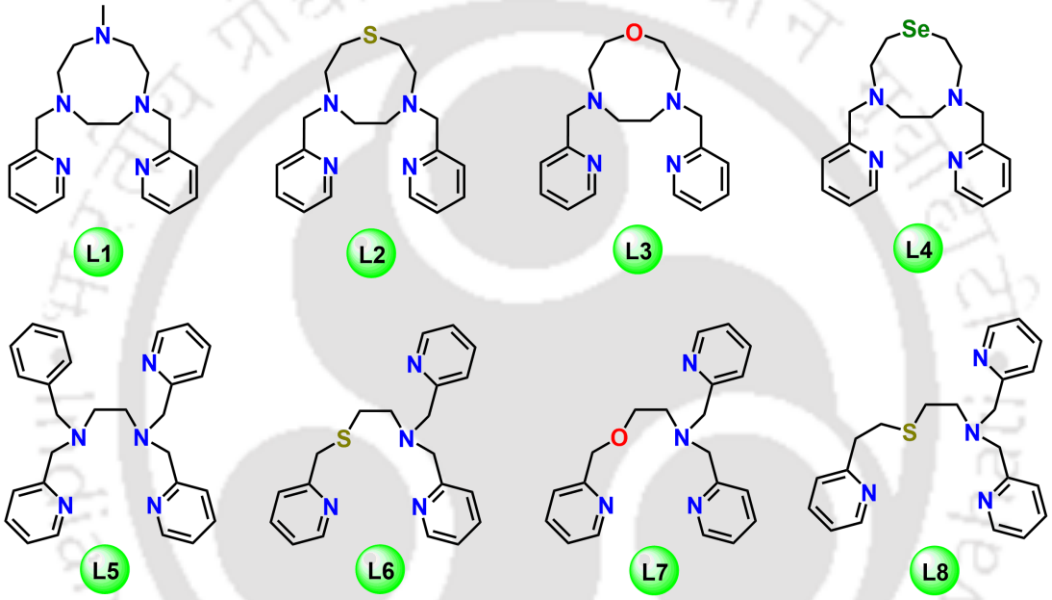

- *Synthesis of the ligand N5-TACN / L1* :

L1=1-Methyl-4,7-bis(2-pyridylmethyl)-triazacyclononane was synthesized following a reported procedure.[5]

Synthesis of ^{P}*L1*: TACN.3HCl (1 eq.) and picolyl chloride hydrochloride (2.1 eq.) were both dissolved in water. The pH of the solution was maintained at pH 9 by the addition of 2 M NaOH. Thereafter, the resulting pale orange solution was stirred for 6 days and the free ligand was extracted into chloroform and the solution

was dried over Na_2SO_4. After filtration the solvent was removed under reduced pressure yielding a yellow oil.

Synthesis of L1: 1,4-bis(2-pyridylmethyl)-1,4,7-triazacyclononane was dissolved in formaldehyde (37%), formic acid (98%), and water, and the resulting yellow solution was refluxed for 30 h. After cooling to room temperature, 3 mL of HCl was added to the mixture and left stirring for 10 min. The solvent was removed under vacuum, and a small amount of water was added to the resulting residue. The solution was brought to pH 14 by the addition of NaOH (4 M). After stirring for 20 min, the aqueous phase was extracted with CH_2Cl_2 (3 × 50 mL). The combined organic phases were dried over anhydrous $MgSO_4$, and the solvent was removed under reduced pressure. The resulting residue was treated with *n*-hexane (75 mL) and stirred for 12 h. The solvent was decanted and removed under reduced pressure to yield a colorless oil. Yield: 1 g, 82%

^{1}H NMR (500 MHz, $CDCl_3$) δ 8.50 (d, J = 4.5 Hz, 2H), 7.64 (t, J = 7.5 Hz, 2H), 7.50 (t, J = 8 Hz, 2H), 7.14 (t, 6 Hz, 2H), 3.82 (s, 4H), 2.88 (s, 12H), 2.34 (s, 3H), *m/z*: 326 (325 + H^+)

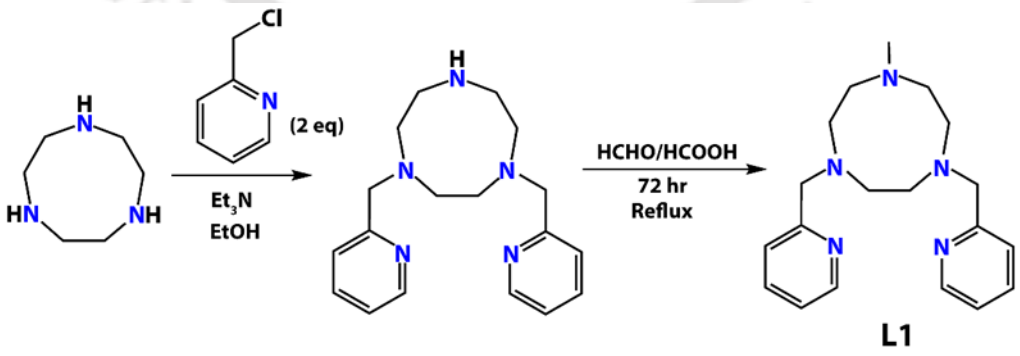

Scheme 2.3. Synthesis of ligand L1.

- *Synthesis of the ligand N4S-TACN / L2*:

Synthesis of L2=1-Thia-4,7-bis(2-pyridylmethyl)-diazacyclononane was prepared by slight modifications from the reported procedure.[6]

Synthesis of L2: Dihydrobromide salt of S-TACN (1 eq.), 2-(chloromethyl)pyridine.HCl (2.1 eq.), and triethylamine (9.5 eq.) were dissolved in absolute ethanol and the reaction mixture was refluxed for 12 h under a N_2 atmosphere and subsequently extracted with chloroform (3 × 100 mL). The chloroform extract was washed with water and dried over anhydrous Na_2SO_4. The solvent was removed using a rotary evaporator.

^{1}H NMR (500 MHz, $CDCl_3$) δ 8.51 (d, J = 5.0 Hz, 2H), 7.68–7.64 (m, 2H), 7.52 (d, J = 7.5 Hz, 2H), 7.16–7.13 (m, 2H), 3.85 (s, 4H), 3.11 (t, J = 5.0 Hz, 4H), 2.95 (t, J = 5.0 Hz, 4H), 2.68 (s, 4H); 13C NMR (125 MHz, CDCl3) δ 160.2, 159.2, 149.3, 148.8, 136.8, 136.5, 123.5, 122.5, 122.2, 120.7, 64.6, 64.4, 59.3, 56.3, 32.3, *m/z*: 329 (328 + H^+)

- *Synthesis of the ligand N4O-TACN / L3*:

Ligand L3 = 1-Oxa-4,7-bis(2-pyridylmethyl)-diazacyclononane was prepared by slight modifications from the reported procedure.[7]

Synthesis of L3: An aqueous solution of 2-picolyl chloride hydrochloride (2.1 equivalents) was added dropwise to a neutralized aqueous solution (10 mL) of O-TACN (1 equivalent), adjusted to pH 7 with 0.5 N NaOH, while stirring over 1 hour at room temperature. The pH of the resulting solution was then raised to 9.0 using 0.5 M NaOH. The resulting orange solution was subsequently extracted three times with chloroform (30 mL each). After washing the organic layers with water,

the combined organic extracts containing the product were dried over Na_2SO_4. The solvent was then evaporated under reduced pressure, yielding a brown oil as the final product. Yield: 1.1 g, 74%.

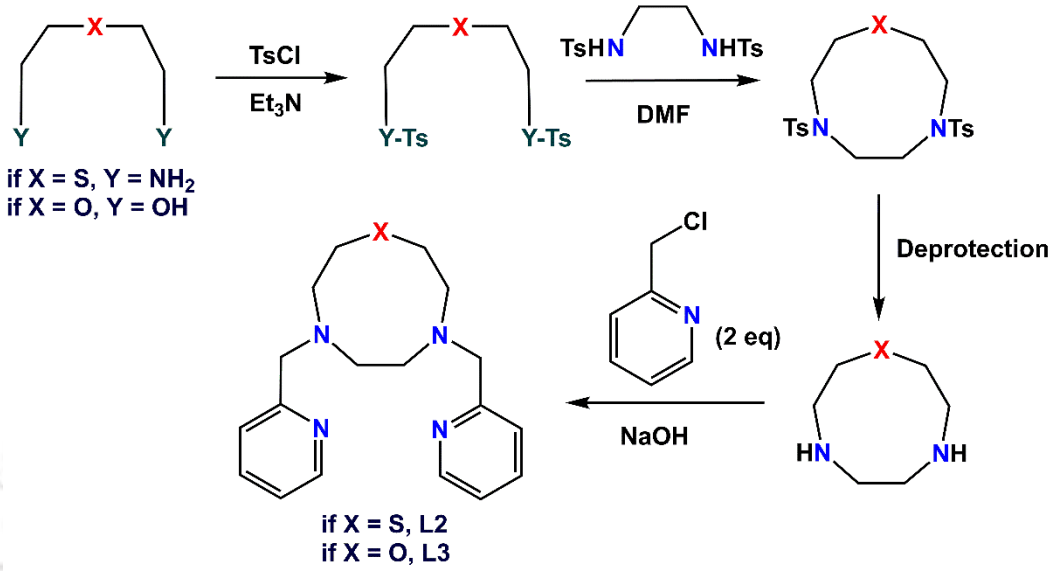

Scheme 2.4. Synthesis of ligand L2 & L3.

NMR Characterization of L1.

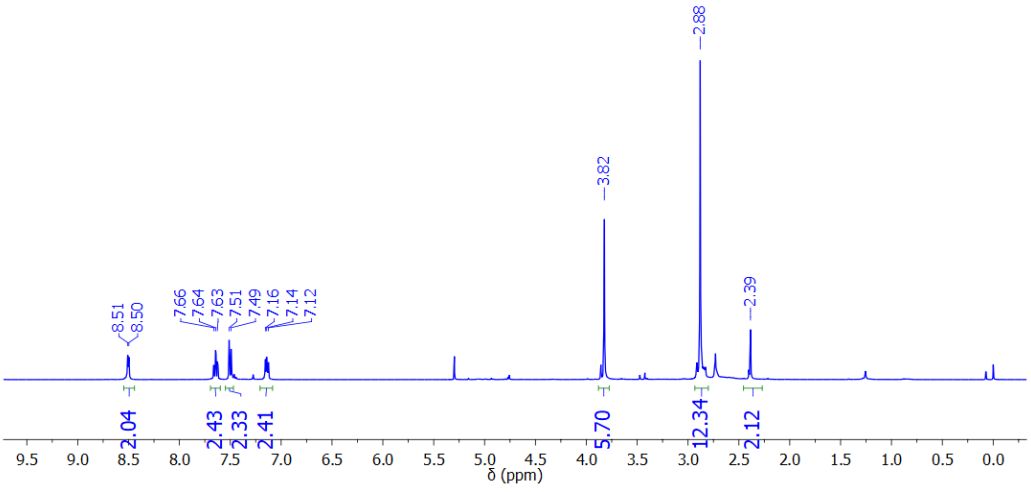

Fig. 2.3. ^{1}H NMR (400 MHz) spectrum of ligand L1 in $CDCl_3$.

NMR Characterization of L2.

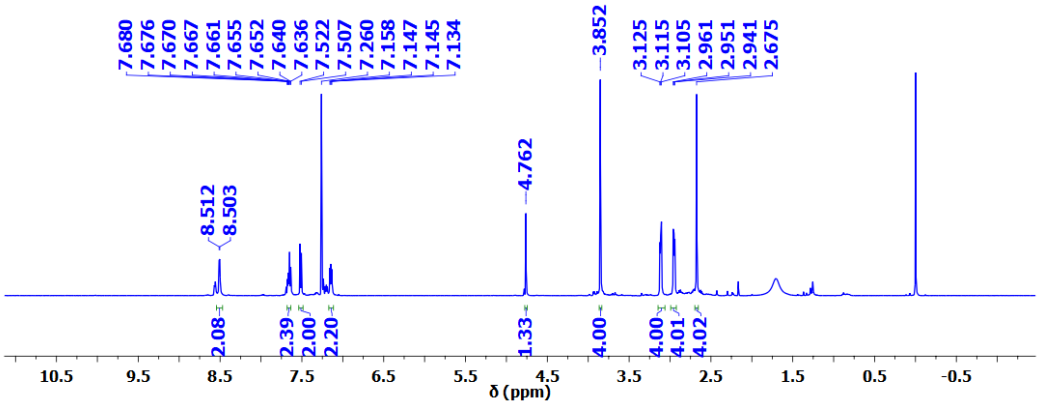

Fig. 2.4. ^{1}H NMR (400 MHz) spectrum of ligand L2 in $CDCl_3$.

NMR Characterization of L3.

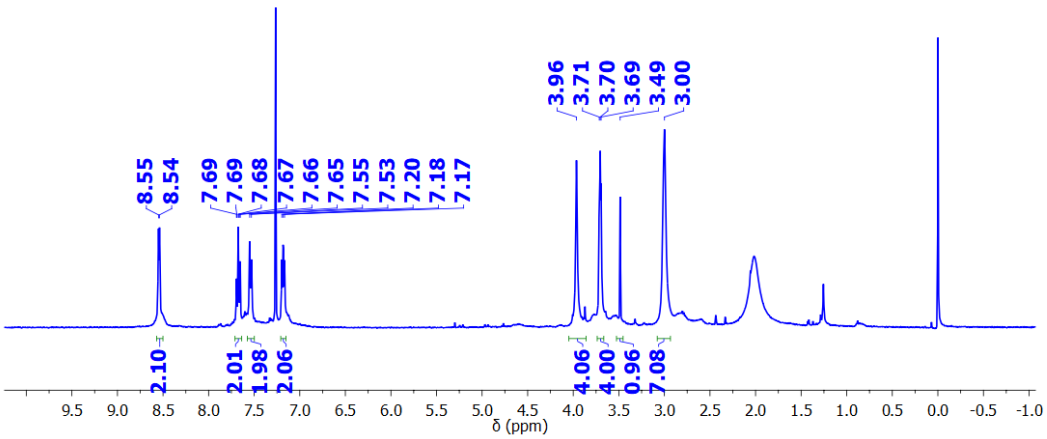

Fig. 2.5. ^{1}H NMR (400 MHz) spectrum of ligand L3 in $CDCl_3$.

- *Synthesis of the ligand BnTPen = N-benzyl-N, N', N'-tris(2 pyridylmethyl)ethane-1,2-diamine /L5*:

Synthesis of L5:[8] N-benzylethylenediamine (1 equivalent) dissolved in CH_2Cl_2 (20 mL) was combined with 2-(chloromethyl) pyridine hydrochloride (3.1 equivalents) in water (20 mL). NaOH (3.2 g, 80 mmol) in water (10 mL) was added incrementally over 5 days under a nitrogen atmosphere. The reaction mixture was extracted with methylene chloride (3 × 25 mL). The collected organic phases were dried with $MgSO_4$, and the solvent was evaporated to yield a white solid. Purification was achieved by Soxhlet extraction using low-boiling petroleum ether. Yield: 1.3 g, 79%.

^{1}H NMR (600 MHz, $CDCl_3$) δ 8.48 (s, 3H), 7.56 (s, 3H), 7.49 – 7.41 (m, 3H), 7.27 (d, J = 19.6 Hz, 5H), 7.11 (s, 3H), 3.77 (s, 4H), 3.71 (s, 2H), 3.58 (s, 2H), 2.72 (d, J = 14.4 Hz, 4H). ^{13}C NMR (150 MHz, CDCl3) δ 160.16 (s), 159.72 (s), 148.94 (s), 148.77 (s), 139.19 (s), 136.37 (s), 128.63 (s), 128.19 (s), 126.89 (s), 122.71 (d, J = 8.5 Hz), 121.85 (d, J = 9.3 Hz), 77.31 (s), 77.10 (s), 76.89 (s), 60.78 (s), 60.57 (s), 58.98 (s), 52.21 (s), 51.89 (s).

- *Synthesis of the ligand STPen/L6*:

Synthesis of L6:[9] A solution of 2-aminoethanethiol (1 equivalent) in CH_2Cl_2 (20 mL) was introduced to a solution of 2-(chloromethyl) pyridine hydrochloride (3.1 equivalents) in water (20 mL). NaOH (3.2 g) dissolved in water (10 mL) was gradually added over 5 days while maintaining a nitrogen atmosphere. The resulting mixture was extracted with methylene chloride (3 × 25 mL), and the combined organic phases were dried using $MgSO_4$. Evaporation of the solvent yielded a brown oil as the final product. Yield: 1.6 g, 92%.

^{1}H NMR (600 MHz, $CDCl_3$) δ 8.49 (dd, J = 11.0, 4.7 Hz, 3H), 7.64 (t, J = 8.4 Hz, 2H), 7.59 (t, J = 7.6 Hz, 1H), 7.55 (d, J = 7.8 Hz, 2H), 7.28 (s, 1H), 7.13 (dd, J = 12.3, 7.1 Hz, 3H), 3.81 (s, 4H), 3.76 (s, 2H), 2.81 – 2.75 (m, 2H), 2.73 – 2.65 (m, 2H). ^{13}C NMR (150 MHz, CDCl3) δ 159.44, 158.76, 149.27, 148.92, 148.52,

136.62, 136.41, 122.94, 121.96, 121.83, 120.40, 77.28, 77.06, 76.85, 64.20, 60.14, 54.66, 53.59, 48.03, 38.21, 37.85, 31.79, 29.28.

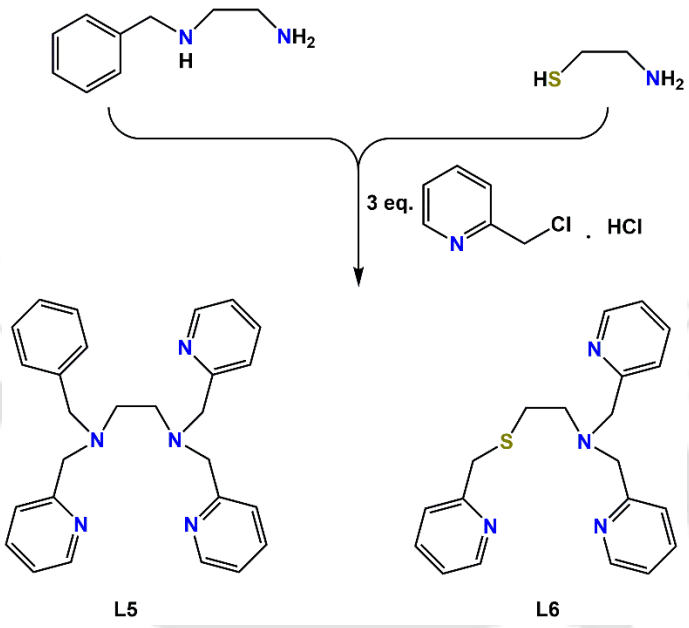

Scheme 2.5. Synthesis of ligand L5 & L6.

NMR Characterization of L5 & L6.

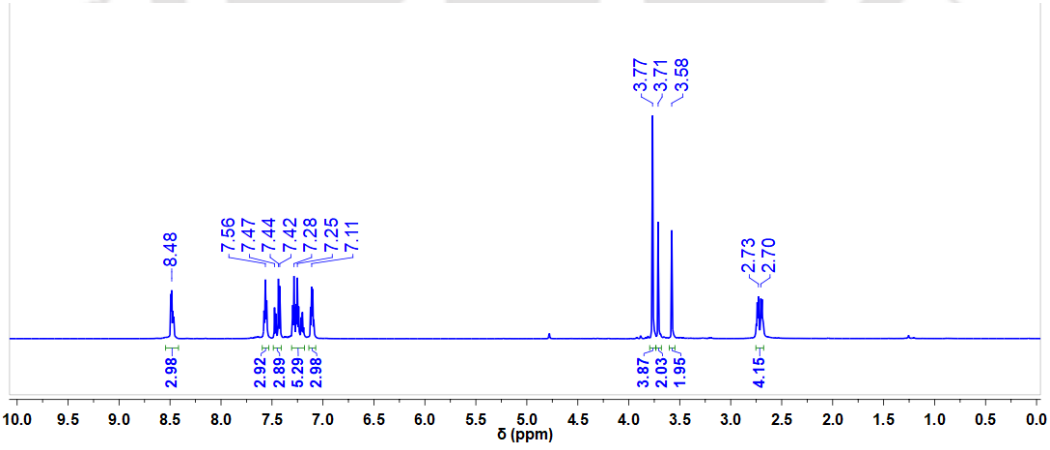

Fig. 2.6. ^{1}H NMR (400 MHz) spectrum of ligand L5 in $CDCl_3$.

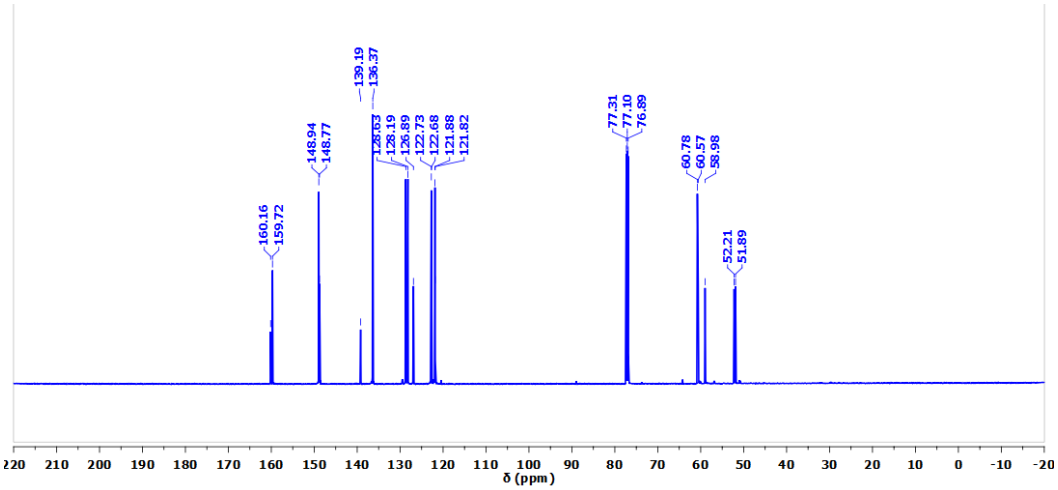

Fig. 2.7. ^{13}C NMR (400 MHz) spectrum of ligand L5 in $CDCl_3$.

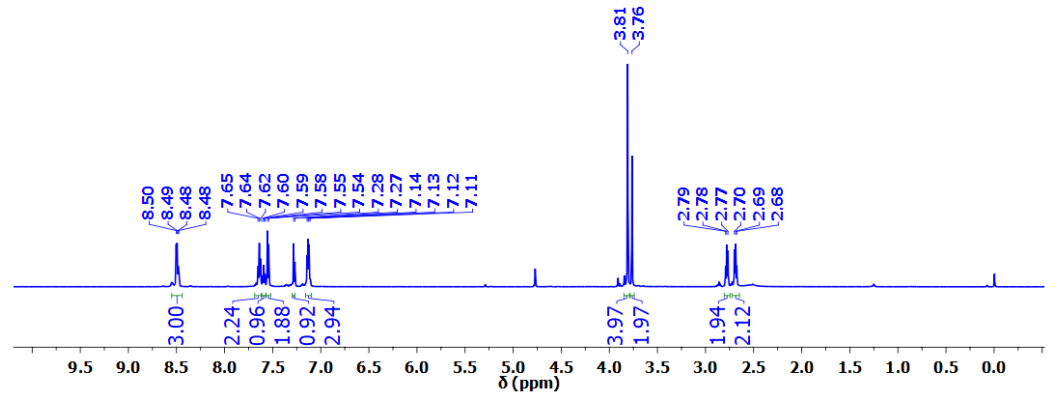

Fig. 2.8. ^{1}H NMR (400 MHz) spectrum of ligand L6 in $CDCl_3$.

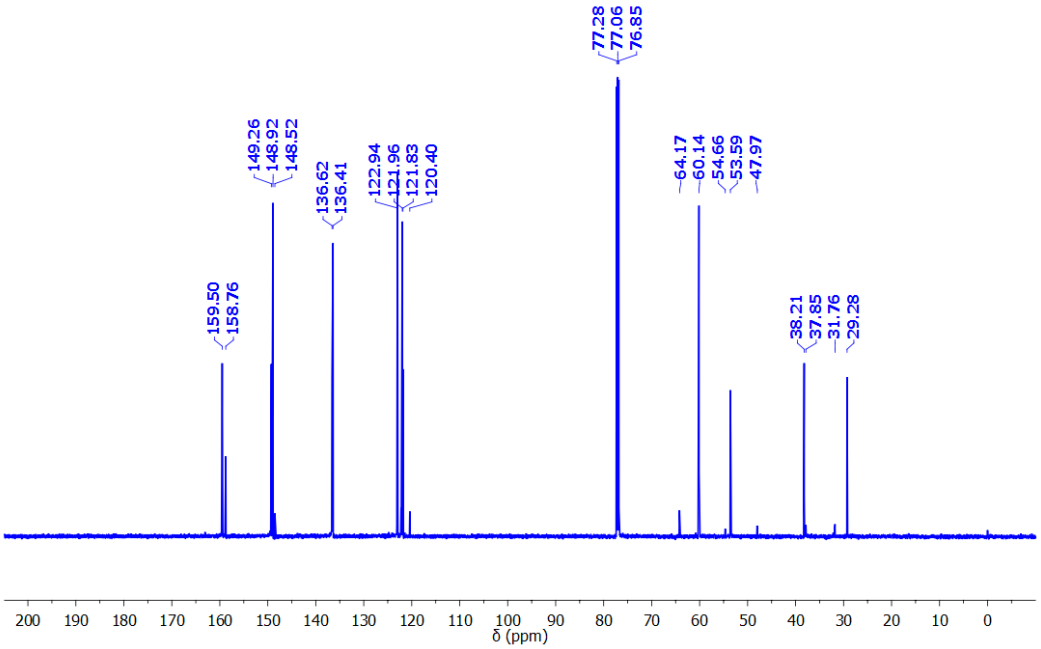

Fig. 2.9. ^{13}C NMR (400 MHz) spectrum of ligand L6 in $CDCl_3$.

- *Synthesis of the ligand L8*: The ligand (L) was synthesized with slight modification from previously reported procedure (see Scheme S1).[10]

Synthesis of $^{P}L8$: 1 equivalent of 2-aminoethanethiol hydrochloride was combined with 1 equivalent of 2-vinylpyridine in 50 mL of ethanol, and the mixture was refluxed until clear. Subsequently, 25 mL of 1 M NaOH in ethanol was added, and reflux continued for 10 minutes. The resulting light-yellow cloudy solution was filtered to remove NaCl, and the filtrate was evaporated to yield a yellow oil. This oil was dissolved in water, and the aqueous solution was extracted with 3 portions of 20 mL CH_2Cl_2. The combined organic layers were dried with $MgSO_4$, and the solvent was evaporated to afford a yellow oil, (^{P}L). This product was used in the subsequent step without further purification.

Synthesis of L8: In the second step, 2.1 equivalents of 2-picolyl chloride hydrochloride were reacted with PL8 (1 equivalent) in 20 mL of water. To this

mixture, 10 mL of 8 M NaOH solution was added. The reaction proceeded for 6 days, after which the compound was extracted with 30 mL of CH_2Cl_2. This extraction process was repeated three times. The organic phase was subsequently washed with Na_2SO_4 and filtered. The resulting solution was concentrated under vacuum to obtain a brown oil (L8). Yield: 2 g, 91%. The purity of the ligand was confirmed using nuclear magnetic resonance (NMR) spectroscopy. $C_{21}H_{24}N_4S$ (M = 364.51 g mol^{-1}). ^1H NMR ($CDCl_3$, 400 MHz) ppm: 8.51–8.49 (s, 3H), 7.64 (dt, J = 7.6 Hz, 2H), 7.59–7.54 (m, 3H), 7.14–7.09 (m, 4H), 3.84 (s, 4H), 3.01–2.68 (m, 8H). 13C NMR (CDCl3, 100.6 MHz) ı, ppm: 160.3, 159.8, 149.7, 149.3, 136.7, 136.6, 123.5, 123.3, 122.3, 121.7, 60.5, 54.2, 38.8, 32.1, 30.1. ESI-MS (positive mode, CH_3CN): m/z, 365.5 $\{[L+H]\}^+$.

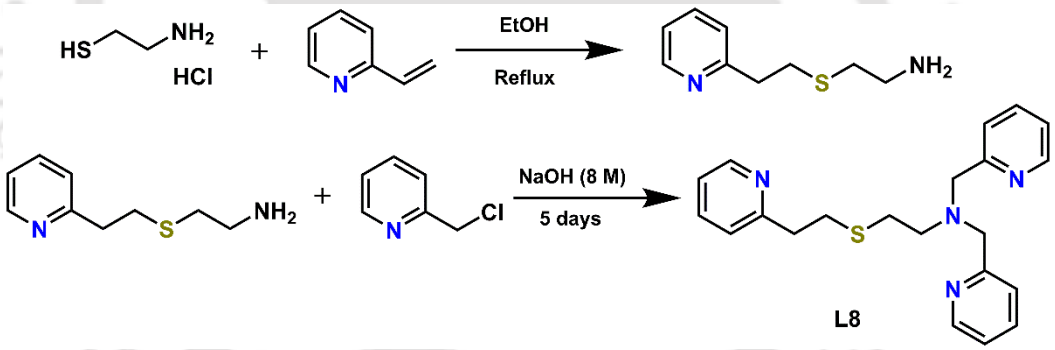

Scheme 2.6. Synthesis of ligand L8.

NMR Characterization of L8.

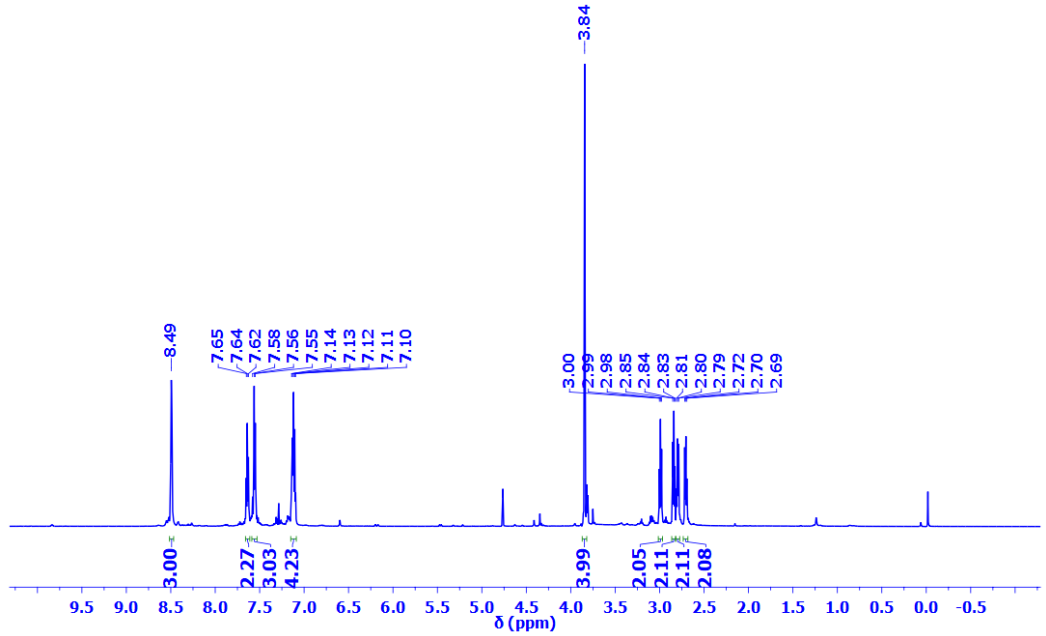

Fig. 2.10. ^{1}H NMR (400 MHz) spectrum of ligand L8 in $CDCl_3$.

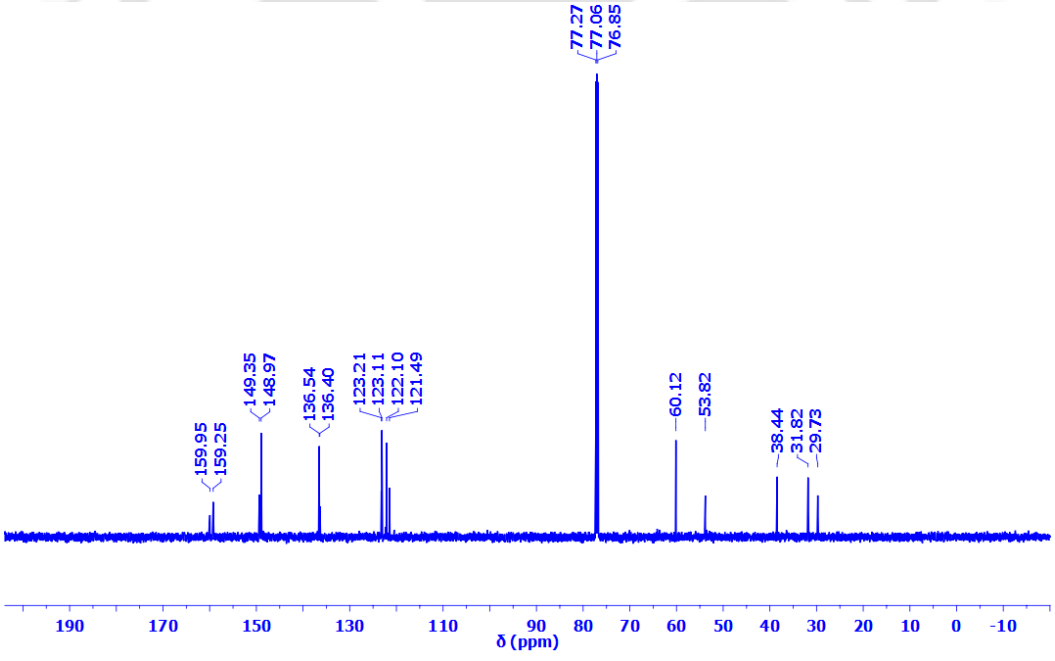

Fig. 2.11. ^{13}C NMR (400 MHz) spectrum of ligand L8 in $CDCl_3$.

2.2.5. Metal Complexes

- *General Procedure for the synthesis of the Fe(II)-complexes.*

The ferrous complexes were synthesized by following a general procedure: 100 mg of ligand was dissolved in CH_3CN (2 mL) inside a glove box filled with argon. To this solution, 1.2 equivalents of Fe(II) salts (triflates, perchlorates, or tetrafluoroborates) in CH_3CN (2 mL) were added, and the mixture was stirred overnight to ensure complete metalation. The resulting solution was filtered using 0.2 µm PTFE syringe filters and crystallized by slow vapor diffusion of diethyl ether into a CH_3CN solution, then stored at -40°C. The obtained complexes were washed with diethyl ether and dried under vacuum to obtain the desired metal complexes (Table 2.1).

Table 2.1. Synthetic parameters and characteristics of metal complexes.

Complex	Ligand	Metal Salt	Solvent	Colour	Texture	Yield
1a	L1	$Fe^{II}(CH_3CN)_2(OTf)_2$	CH_3CN	Dark red	Crystalline	95%
2a	L2	$Fe^{II}(CH_3CN)_2(OTf)_2$	CH_3CN	Dark yellow	Powder	92%
3a	L3	$Fe^{II}(CH_3CN)_2(OTf)_2$	CH_3CN	Brown	Powder	90%
5a	L5	$Fe^{II}(CH_3CN)_2(OTf)_2$	CH_3CN	Dark Red	Crystalline	85%
6a	L6	$Fe^{II}(CH_3CN)_2(OTf)_2$	CH_3CN	Dark Red	Crystalline	88%
7a	L7	$Fe^{II}(CH_3CN)_2(OTf)_2$	CH_3CN	Dark Yellow	Powder	90%
8a	L8	$Fe^{II}(CH_3CN)_2(OTf)_2$	CH_3CN	Dark Red	Powder	91%

2.3. Characterization of the Fe(II) Complexes

2.3.1. ESI-MS

The ESI-MS spectra of all the Fe(II)-complexes were recorded in acetonitrile solvent, at ambient temperature. The samples were carefully filtered through syringe filters before injecting into the mass spectrometer.

- *ESI-MS spectrum of* $[Fe^{II}(L1)(OTf)]^+$:

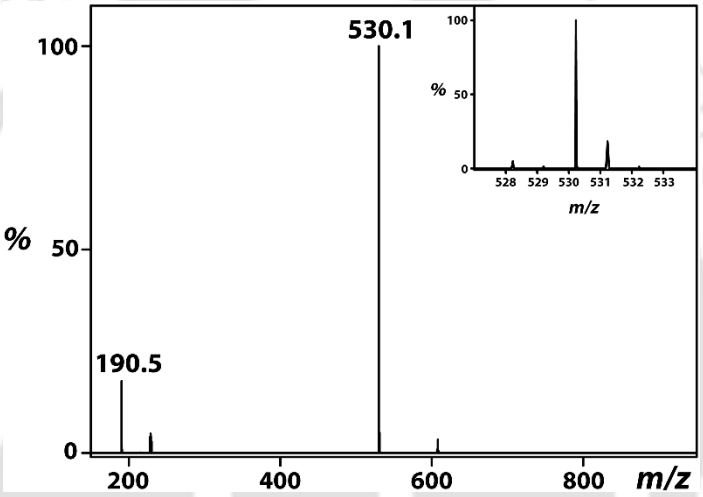

Fig. 2.12. ESI-MS spectrum of $[Fe^{II}(L1)(OTf)]^+$; *m/z* 530.1 and 190.5 corresponds to $[Fe^{II}(L1)(OTf)]^+$ and $[Fe^{II}(L1)]^{2+}$ respectively. Inset shows the isotopic distribution pattern for the *m/z* values of 530.1.

- *ESI-MS spectrum of* $[Fe^{II}(L2)(OTf)]^+$:

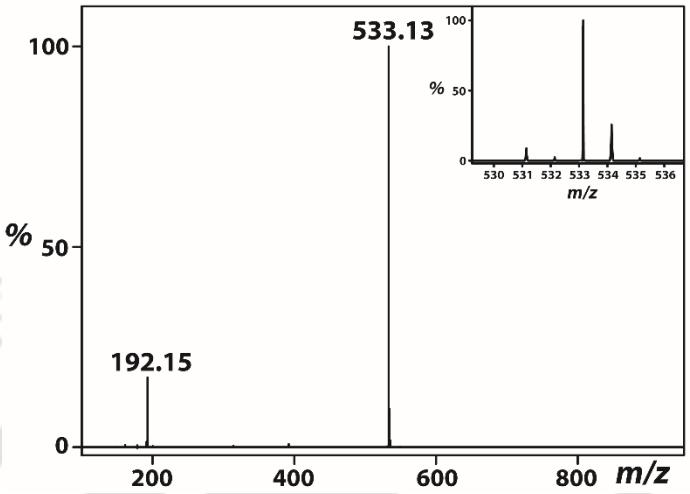

Fig. 2.13. ESI-MS spectrum of $[Fe^{II}(L2)(OTf)]^+$; *m/z* 533.13 and 192.15 corresponds to $[Fe^{II}(L2)(OTf)]^+$ and $[Fe^{II}(L2)]^{2+}$ respectively. Inset shows the isotopic distribution pattern for the *m/z* values of 533.1.

- *ESI-MS spectrum of* $[Fe^{II}(L3)(OTf)]^+$:

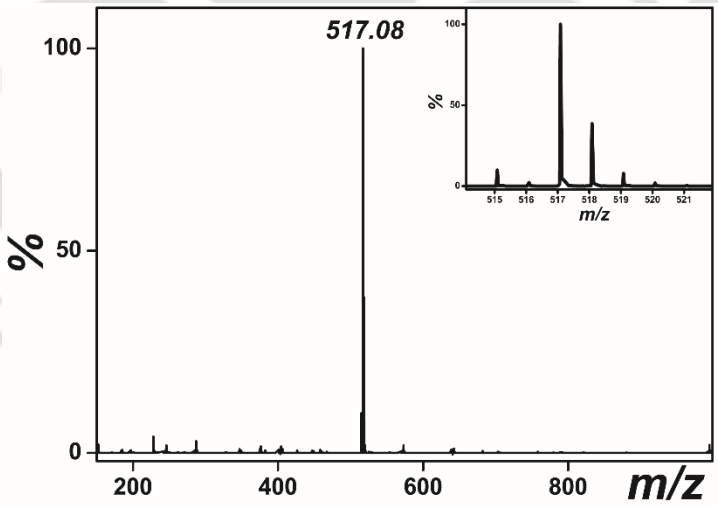

Fig. 2.14. ESI-MS spectrum of $[Fe^{II}(L3)(OTf)]^+$; *m/z* 517.08 corresponds to $[Fe^{II}(L3)(OTf)]^+$. Inset shows the isotopic distribution pattern for the *m/z* 517.08.

- *ESI-MS spectrum of $[Fe^{II}(L5)(OTf)]^+$:*

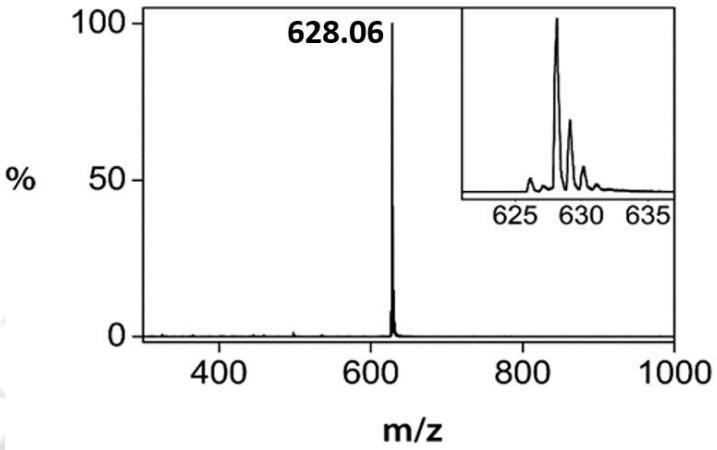

Fig. 2.15. ESI-MS spectrum of $[Fe^{II}(L5)(OTf)]^+$; *m/z* 628.06 corresponds to $[Fe^{II}(L5)(OTf)]^+$. Inset shows the isotopic distribution pattern for the *m/z* 628.06.

- *ESI-MS spectrum of $[Fe^{II}(L6)(OTf)]^+$:*

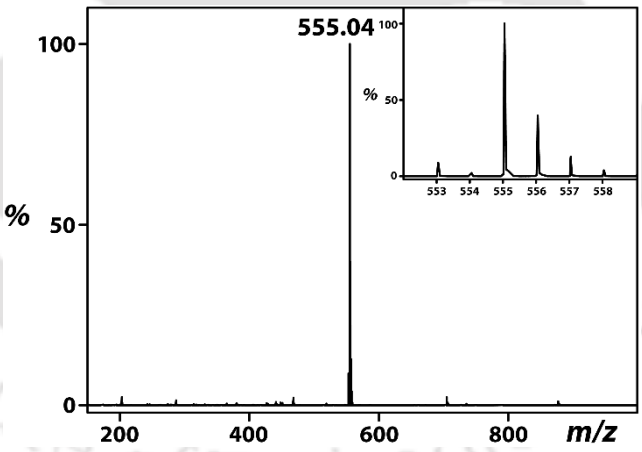

Fig. 2.16. ESI-MS spectrum of $[Fe^{II}(L6)(OTf)]^+$; *m/z* 555.04 correspond to $[Fe^{II}(L6)(OTf)]^+$. Inset shows their isotopic distribution pattern for $[Fe^{II}(L6)(OTf)]^+$.

- *ESI-MS spectrum of* $[Fe^{II}(L8)(OTf)]^+$:

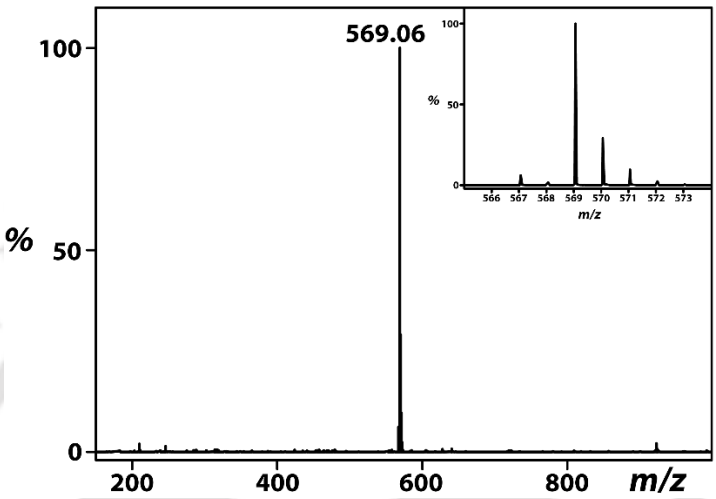

Fig. 2.17. ESI-MS spectrum of $[Fe^{II}(L6)(OTf)]^+$; *m/z* 569.06 correspond to $[Fe^{II}(L6)(OTf)]^+$. Inset shows their isotopic distribution pattern for $[Fe^{II}(L6)(OTf)]^+$.

2.3.2. ^{1}H-NMR

Generally, NMR spectroscopy is mainly conducted on diamagnetic molecules, but paramagnetic samples can also be analysed using NMR, albeit with some distinguishing effects such as broadening of the spectral patterns and large chemical shift values. In spite of all these challenges, ^{1}H-NMR spectroscopy of metal complexes remains valuable for providing crucial structural insights and information about bonding patterns.

^{1}H NMR spectra of metal complexes shows paramagnetically induced shifts across a broad spectral range of approximately 200 ppm. These shifts, known as isotropic shifts, arise from differences in chemical shifts with and without a metal ion present. These shifts can be substantial, ranging from -100 to +200 ppm due to the

presence of unpaired electrons in metal complexes. The α-protons, nearest to the metal center, are typically the most affected and may sometimes be indistinguishable. In cases where substitution occurs at the α-position, β-protons can also exhibit significant shifts due to interactions with the metal ion.

The coordination number, geometry, and spatial arrangement of protons around the metal center play critical roles in determining the observed shift patterns in different systems. Mechanisms such as σ-delocalization contribute to downfield shifts of pyridine protons in the order α-H > β-H > γ-H.[11-15] On the other hand, π-delocalization can lead to a shift pattern where β-H shifts downfield while α-H and γ-H shift upfield.[16]

Scheme 2.7. Numbering scheme for metal complexes containing substituted pyridine donors.

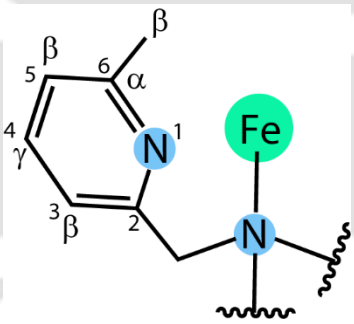

^{1}H-NMR spectrum of [Fe^{II}(L1)(OTf)]$^{+}$:

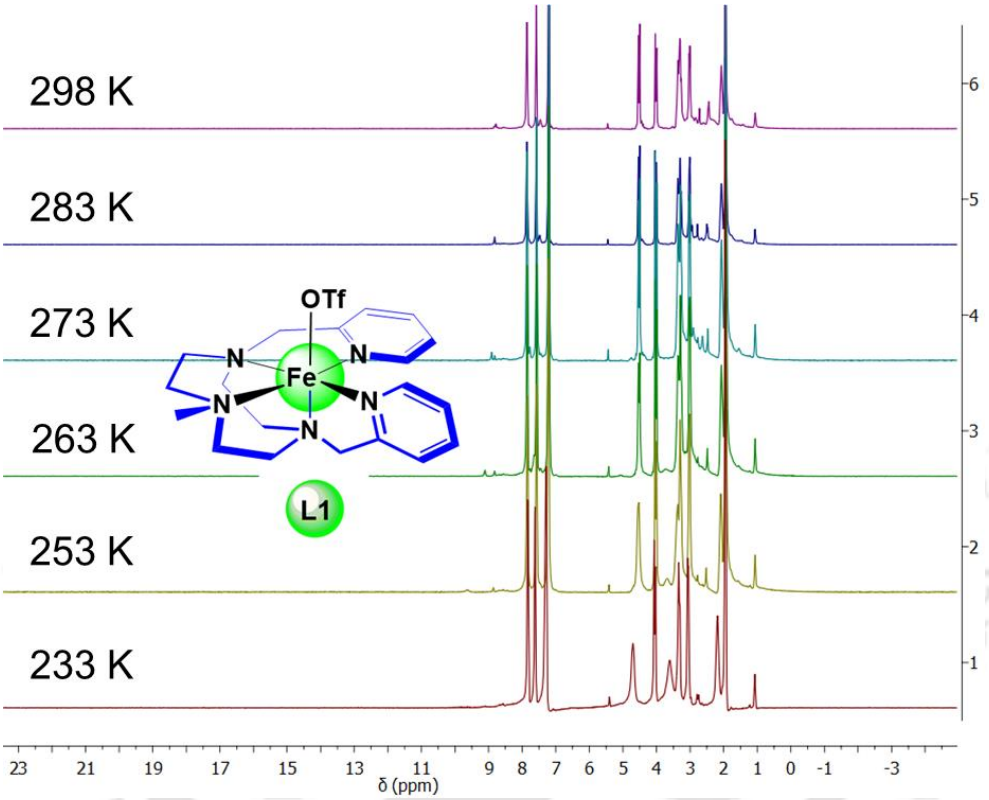

Fig. 2.18. ^{1}H-NMR spectrum (400 MHz) of complex 1a in CD_3CN at different temperatures ranging from 298 K-233 K with a spectral width of ~200 ppm (no. of scans = 128).

- *^{1}H-NMR spectrum of [Fe^{II}(L2)(ClO$_4$)]$^+$*:

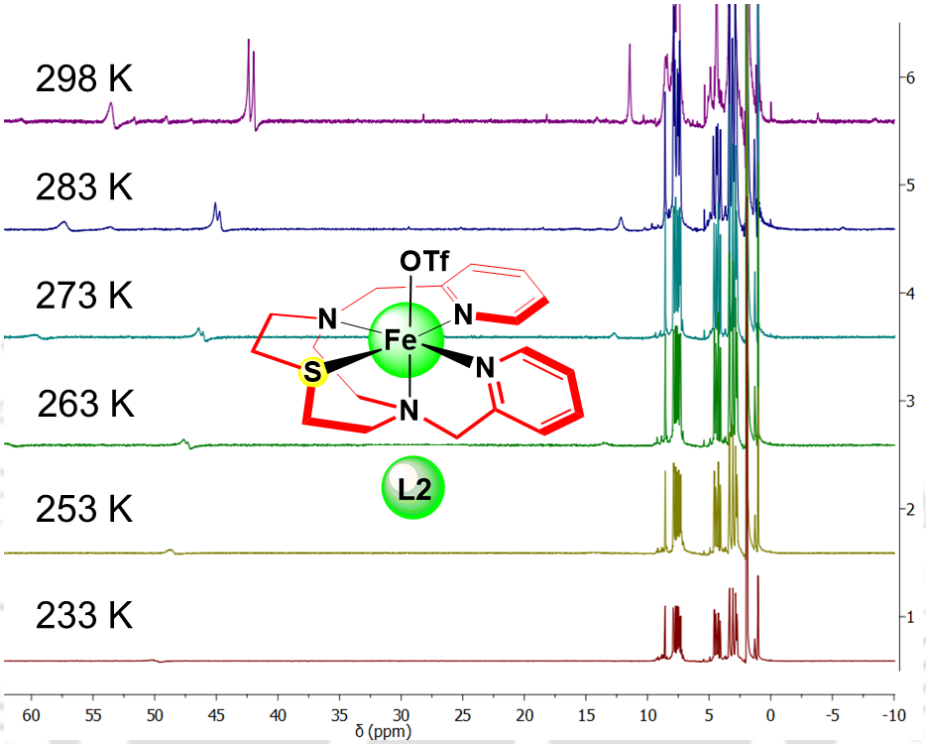

Fig. 2.19. ^{1}H-NMR spectrum (400 MHz) of complex 2a in CD_3CN at different temperatures ranging from 298 K-233 K with a spectral width of ~200 ppm (no. of scans = 128).

2.3.3. Cyclic Voltammetry and Differential Pulse Voltammetry

The cyclic voltammetry experiments were carried out at room temperature using a CH Instruments Electrochemical Analyzer CHI1120B series. A three-electrode system was used where a glassy carbon was used as the working electrode, Pt wire as the auxiliary electrode, and aqueous Ag/AgCl as the reference electrode. The solutions used were 1 mM of **1a,** and 100 mM supporting electrolyte tetra-*n*-butylammonium hexafluorophosphate ($TBAPF_6$) in acetonitrile.

- *CV & DPV Spectra of* $[Fe^{II}(L1)(OTf)]^+$ *&* $[Fe^{II}(L2)(OTf)]^+$:

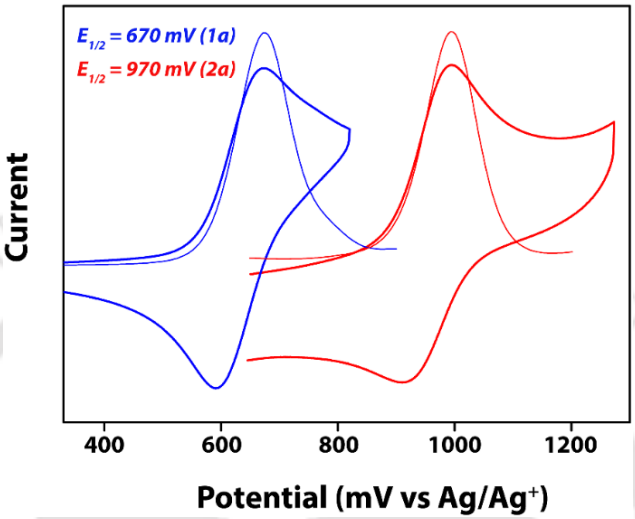

Fig. 2.20. CV & DPV Spectra of **1a** & **2a** in acetonitrile at room temperature.

- *CV & DPV Spectra of* $[Fe^{II}(L5)(OTf)]^+$ *&* $[Fe^{II}(L6)(OTf)]^+$:

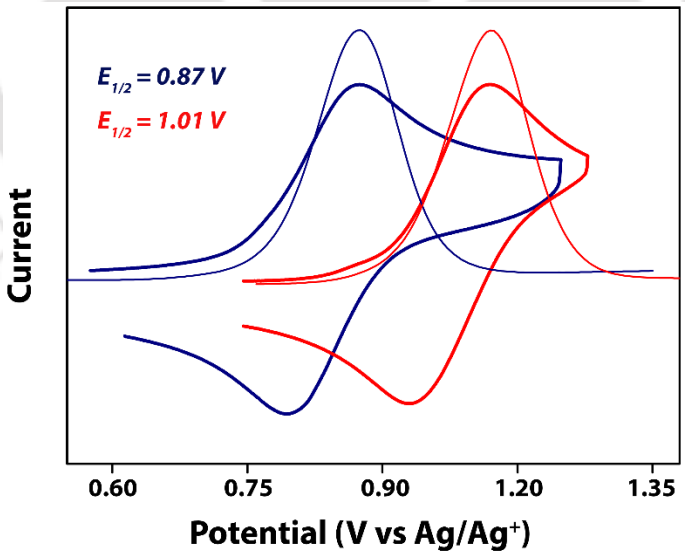

Fig. 2.21. CV & DPV Spectra of **5a** (Blue) & **6a** (Red) in acetonitrile at room temperature.

- *CV & DPV Spectra of* $[Fe^{II}(L8)(OTf)]^{+}$:

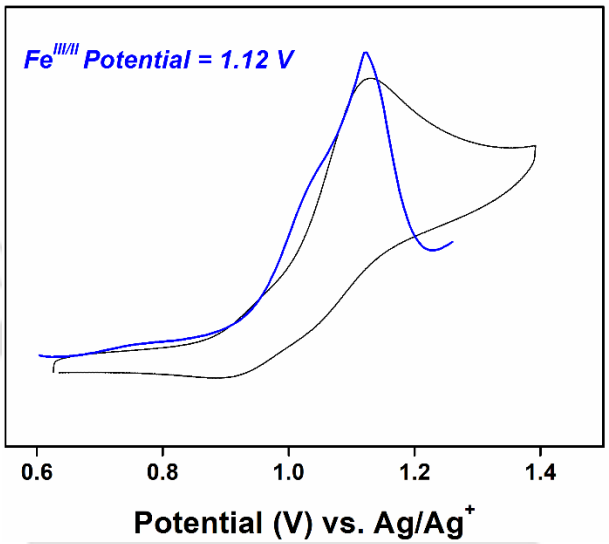

Fig. 2.22. CV & DPV Spectra of **8a** in acetonitrile at room temperature.

2.3.4. EPR Spectrocopy

The X-band electron paramagnetic resonance (EPR) was measured on a JEOL (JES-FA200) ESR spectrometer at 77 K in acetoniotrile. Experimental conditions [frequency, 9135.99 MHz; power, 0.995 mW; field center, 336.00 mT, width, ±50.00 mT; sweep time, 30.0 s; modulation frequency, 100.00 kHz, width, 2 mT; amplitude CH1=10, CH2=2.0 and time constant, 0.03 s] were kept the same for all the samples.

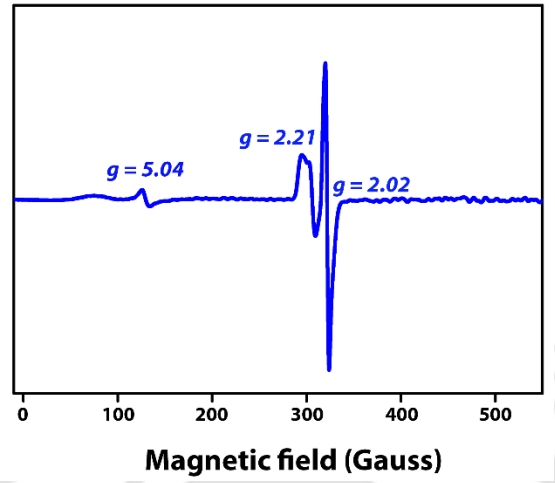

Fig. 2.23. EPR Spectrum of **8b** in acetonitrile at 77 K.

2.3.4. resonance Raman Spectroscopy

The resonance Raman spectra of 2a was obtained at 638 nm (80 mW, Cobolt lasers, HÜBNER Photonics) excitation wavelengths using a Kymera 328i motorized Czerny-Turner Spectrograph (Andor Technology) equipped with a DU 420A-BEX2-DD camera (iDus 420 CCD, Andor Technology). The CCD camera was cooled to −80 °C. The spectral slit width of the instrument was set to 120 µm.

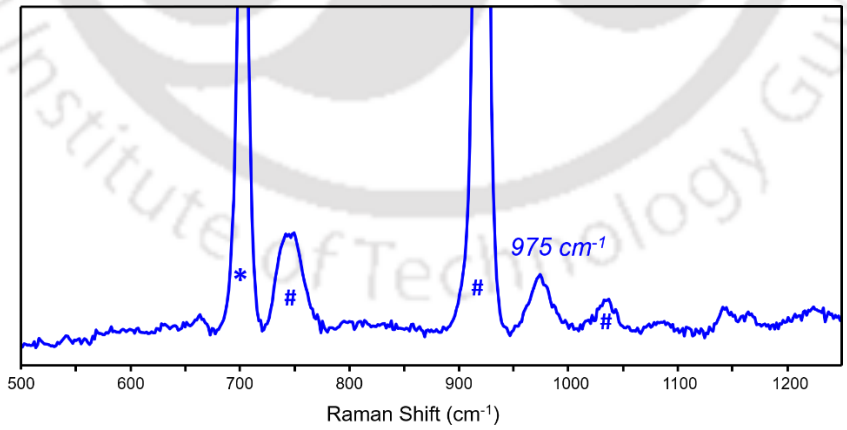

Fig. 2.24. Resonance Raman Spectrum of **6c** [Fe^{IV}(NTs)L6] in acetonitrile at RT upon 561 nm excitation wavelength. (* & # denote the solvent peaks)

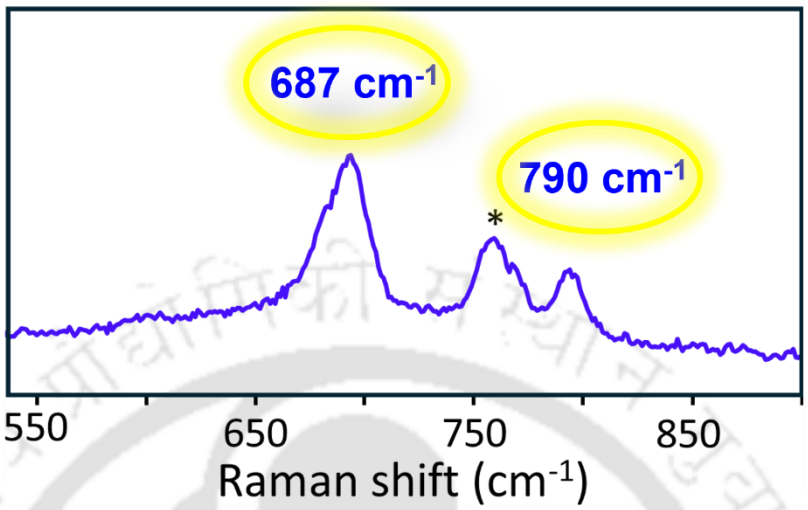

Fig. 2.25. Resonance Raman Spectrum of **8b** in acetonitrile at 233 K upon 638 nm excitation wavelength. (* denotes the solvent peaks)

2.3.3. X-ray crystallography

- *Crystallographic data for complex* $[Fe^{II}(L6)(CH_3CN)](OTf)_2$ *and its structure refinement parameters* :

The X-ray single crystal diffraction data for the complex was collected by Bruker APEX-II CCD diffractometer at room temperature. Data refinement and cell reductions were carried out by Bruker SAINT Software. Data reduction and cell refinements were per formed using SAINT and XPREP software. Structures were solved by direct methods using SHELXS-97 and were refined by full-matrix least-squares on F2 using SHELXL-14 and OLEX2 programs. CCDC 2310147 contains the supplementary crystallographic data for this complex. These data are provided free of charge by The Cambridge Crystallographic Data Centre. Dark wine red crystals were grown by slow vapour diffusion of diethyl ether into the acetonitrile solution of the Fe(II) complex. The refined structure shows binding of a solvent (CH_3CN) molecule to the Fe(II) and two non-bound OTf counter-anions.

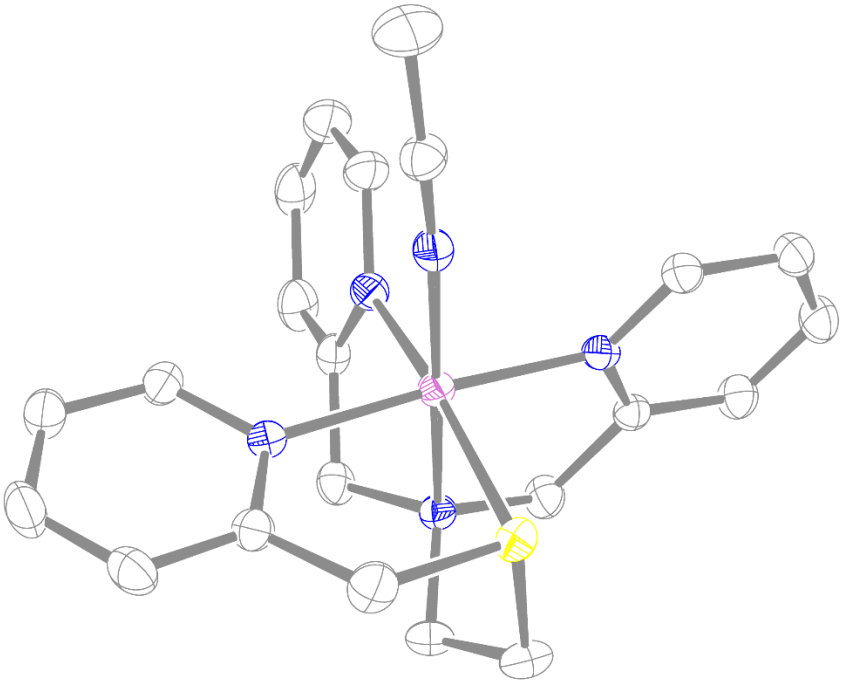

Fig. 2.26. ORTEP plot of $[Fe^{II}(STPen)(CH_3CN)]$ $(OTf)_2$ with thermal ellipsoid drawn at 30 % probability level. Counter-ions and hydrogens have been omitted for better clarity.

Table 2.2. Structure refinement parameters.

Crystal identification	Fe-L6-OTf	
Empirical formula (Calculated)	C_{24} H_{25} F_6 Fe N_5 O_6 S_3	
Formula Weight (Calculated)	745.52 g/mol	
Color, morphology	Deep red, block	
Temperature	293 K	
Wavelength	0.71073 Å	
Space group (Calculated)	P -1	
Hall group	-P 1	
Volume (Calculated)	1536 (3) $Å^3$	
Bond precision	C-C = 0.0056 Å	
Unit cell parameters	*a* = 11.840 (13) Å	α = 109.78 (3) ˚
	b = 12.227 (13) Å	β = 95.38 (4) ˚
	c = 12.436 (13) Å	γ = 110.84 (3)˚
Z (calculated)	2	
Density (calculated) (g cm^{-3})	1.612	
Mu (mm^{-1})	0.779	
F000 (F000')	760.0 (761.87)	
h, k, l $_{max}$	14, 15, 15	
N $_{ref}$ (calculated)	6482	
N $_{ref}$ (Reported)	6333	
Minimum transmission (T) (calculated) [reported limit]	0.817 [0.869]	
Maximum transmission (calculated) [reported limit]	0.660 [0.747]	
Absorption correction	Multi-scan	
Data completeness	0.977	
Theta (max)	26.667	
R (Reflections)	0.0518 (4158)	
wR2 (Reflections)	0.1379 (6333)	
R	0.0518 (4158)	
S	1.081	
Npar	407	
Prob (%)	50	

Table 2.3. Selected bond lengths [Å] and bond angles [°] for $[Fe^{II}(L4)(CH_3CN)](BF_4)_2$.

Bonds		**Bond-lengths (Å)**	
Fe1 _ N1		1.980	
Fe1 _ N2		2.025	
Fe1 _ N3		2.010	
Fe1 _ N4		1.956	
Fe1 _ N5		1.929	
Fe1 _ S1		2.261	
Avg Fe _ N		1.980	
***cis*-equatorial bond angles (°)**		***cis*-bond angle of equatorial Fe1-S with $N_{ax/eq}$ (°)**	
∠ N1-Fe1-N4	90.05(2)	∠ N3-Fe1-S1	85.50 (2)
∠ N1-Fe1-N3	94.34(2)	∠ N4-Fe1-S1	89.90(2)
∠ N2-Fe1-N4	84.18(2)	∠ N2-Fe1-S1	88.44(2)
∠ S1-Fe1-N3	85.50(2)	∠ N5-Fe1-S1	96.94(2)
***trans*-equatorial bond angles (°)**		***cis*-bond angle of equatorial Fe1-N/ Fe1-S with N2 (°)**	
∠ N3-Fe1-N4	175.38(2)	∠ N1-Fe1-N2	80.84(2)
∠ S1-Fe1-N1	169.23(2)	∠ N4-Fe1-N2	84.18(2)
-	-	∠ N3-Fe1-N2	95.11(2)
-	-	∠ S1-Fe1-N2	88.44(2)

The crystal structure (Fig. 2.24 and Table 2.3) shows clear penta-coordination of the metal to the STPen ligand in a structural orientation analogous to the reported complexes $[Fe^{II}(BnTPen)]^{2+}$.[17,18] The Fe-N bond distances, as shown in Table 2.3, are typical for low-spin Fe(II) complexes reported previously.[17-24]

2.3.4. UV-vis Spectroscopy

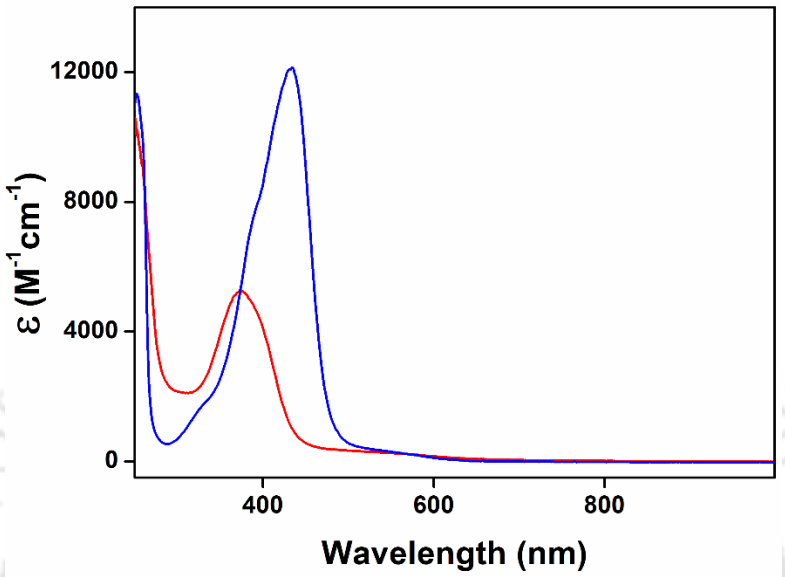

Fig. 2.27. UV-vis spectra of complexes **1a** (Blue) & **2a** (Red) in acetonitrile at RT.

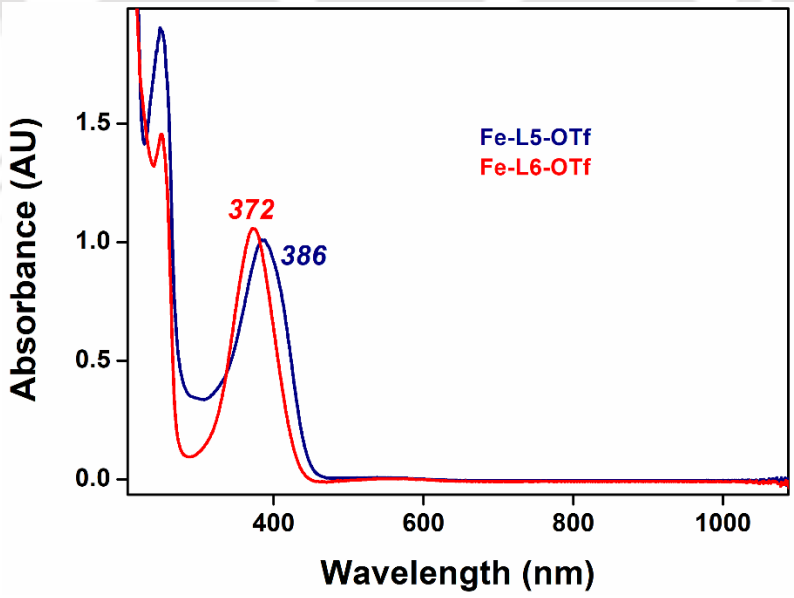

Fig. 2.28. UV-vis spectra of complexes **5a** (Blue) & **6a** (Red) in acetonitrile at RT.

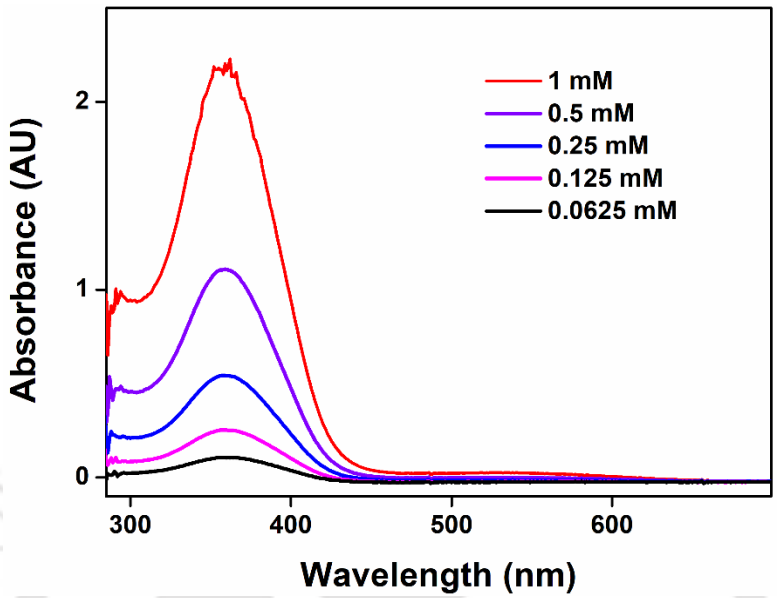

Fig. 2.29. UV-vis spectra of complex **8a** in acetonitrile at RT.

2.4. Generation of the Reactive Metal Intermediates

The formation of the Fe(IV)=O intermediates (1b & 2b) was achieved by vigorous stirring of the Fe(II) complex, (1a & 2a) with excess solid PhIO in acetonitrile and filtering off the unreacted excess oxidant using 0.2 μm PTFE syringe filters. The resulting clean filtrate was stored in cold and used for further studies. The Fe(IV)-oxo complexes 5b & 6b were synthesized *in situ* from their respective Fe(II) precursor complexes at room temperature by the addition of 1.5 equivalents of ^{S}PhIO in acetonitrile. The Fe(IV)-tosylimido species 5c & 6c were synthesized *in situ* from their respective Fe(II) precursor complexes at room temperature by the addition of 1.5 equivalents of ^{S}PhINTs in acetonitrile. Complex 8b was formed upon addition of little excess (~30 equivalents) of *tert*-butyl hydroperoxide solution (70% in water) in acetonitrile at room temperature. The stability of these intermediates are crucial considerations in order to successfully

characterize them using various spectroscopic techniques like ESI-MS, UV/Vis, NMR, EPR and resonance Raman, etc. The formation techniques, stability, characterizations and reactivity of these reactive high valent intermediates are discussed latter in their respective chapters.

2.5. Physical Methods

UV/Vis spectra were recorded on a Hewlett Packard 8453 spectrophotometer equipped with either constant temperature circulating water bath or a liquid nitrogen cryostat (Unisoku) with a temperature controller. High-resolution electrospray ionization-mass spectra (ESI-MS) were recorded on a Waters (Micromass MS Technologies) Q-TOF Premier mass spectrometer by infusing analyte samples directly into the source at 15 μL min^{-1} using a syringe pump. The spray voltage was set at 2 kV and the capillary temperature at 80 °C unless otherwise mentioned. Also, few mass spectra were recorded with the help of Agilent-Q-TOF 6520 instrument in positive mode equipped with a Mass hunter workstation; the spray voltage was set at 3 kV and the drying gas flow and temperature were maintained as 5.0 L min^{-1} and 200 °C respectively. NMR spectra were recorded on Bruker Avance III HD 600 MHz and 400 MHz spectrometers and a Jeol Advanced Solution State 400 MHz spectrometer (JNMECZ400S) using TMS as internal standard under ambient conditions unless otherwise mentioned. The reported chemical shifts (in ppm) are in reference to the residual solvent peaks. The crystal structure was recorded on an Agilent Single Crystal X-Ray Diffractometer (XRD) equipped with Mo X-ray source (Mova), CCD detector (Eos), Oxford cryo system and crystal AlisPRO and Autochem software.

2.6. Reaction Kinetics

All reactions were conducted in a 10 mm path length UV/Vis cuvette, with UV/Vis spectral changes of the reaction solutions being monitored. Kinetic studies were carried out under pseudo first-order conditions by using excess substrate concentrations. The progress of the reactions was tracked by observing the decrease in absorbance of the characteristic peaks over time. Rate constants were determined by fitting the changes in absorbance of the intermediates. Each reaction was performed in triplicate, and the reported data represent the average of these trials, with the standard deviation being less than 10% of the reported values.

Kinetic experiments were performed by using the following procedures: 1 mM Fe(IV)-oxo complexes including $[Fe^{IV}(O)(L1)]^{2+}$, (1b) and $[Fe^{IV}(O)(L2)]^{2+}$, (2b) were prepared from 1 mM solutions of their ferrous precursor complexes 1a and 2a respectively by reacting with excess amount of solid PhIO in acetonitrile at room temperature. Each time 2.5 mL portion of the Fe(II) solutions were taken in a 4 mL glass vial and then an excess amount of solid PhIO was added to it. Then, the solution was filtered off to remove the unreacted excess oxidant using 0.2 μm PTFE syringe filters. The resulting clean filtrate was stored in cold and used for further studies. 2 mL of the solution was transferred into the quartz cuvette each time and deoxygenated with argon gas sealed with rubber septum and kept in UV/Vis spectrophotometer cuvette holder. For fast reactions, low temperature setup was employed using the low temperature cryostat when the oxidants were added through a 250 μL Hamiltonian syringe, immediately mixed with another 1 ml syringe until the characteristic peaks of intermediates were monitored in the UV/Vis spectrophotometer. Upon the maximum formation of Fe(IV)-oxo chromophore, few minutes were given to equilibrate the solution temperature. The substrates were then slowly added through a 250 μL Hamiltonian syringe into the quartz cuvette and mixed with another 1 mL syringe. The time course of the decay

of the Fe(IV)-oxo chromophore was monitored. Concentrations of the substrates used in each case varied and were adjusted to achieve convenient reaction time and control.

1 mM solutions of $[Fe^{IV}(L5)(O)]^{2+}$ (5b) and $[Fe^{IV}(L6)(O)]^{2+}$ (6b) were prepared from 1 mM solutions of $[Fe^{II}(L5)(OTf)]$ (5a) and/or $[Fe^{II}(L6)(OTf)]$ (6a) by reacting with ^{S}PhIO (1.5 equiv.) in CH_3CN at 25 ºC. Similarly, 1 mM solutions of $[Fe^{IV}(L5)(NTs)]^{2+}$ (5c) and $[Fe^{IV}(L6)(NTs)]^{2+}$ (6c) were prepared from 1 mM solutions of $[Fe^{II}(L5)(OTf)]$ (5a) and/or $[Fe^{II}(L6)(OTf)]$ (6a) by reacting with ^{S}PhINTs (1.5 equiv.) in CH_3CN at 25 ºC. Each time 2.5 mL of Fe(II) complex solution was taken in a 4 mL glass vial, and 2 mL of it was transferred into a cuvette and deoxygenated with argon gas sealed with a rubber septum and kept in UV/Vis spectrophotometer cuvette holder, then slowly 50 μL of 1.5 equivalents of ^{S}PhIO and ^{S}PhINTs was added immediately. The solution was mixed with another 1 ml Cuvette until characteristic peaks of the intermediates were obtained in the visible region. After it reaches the maximum formation of Fe(IV)-oxo and Fe(IV)-NTs intermediates, Then 50 μL of excess substrates were slowly added to the solutions, mixed with another 1 mL cuvette, and the time course of the decay of the Fe(IV)-oxo and Fe(IV)-NTs chromophore was monitored.

The formation of the alkylperoxo adduct was identified at 233 K. when 8a was treated with *tert*-butyl hydroperoxide solution (70% in water, 30 eq.). A new blue species (8b) was formed gradually. 1 mM solutions of 8a in CH_3CN was reacted with excess *tert*-butyl hydroperoxide and the formation spectra were optimized with the help of UV/Vis spectrophotometer. The oxidant solution and substrates were prepared in CH_3CN and substrates were added to the intermediates solution formed *in situ* at different temperature depending upon the rates of decay. Plots of the k_{obs} against substrate concentrations gave the second-order rate constants for each system. The reaction mixtures were removed from the cuvette,

oxidation products and metal salts were separated and passed through the silica gel and washed subsequently with CH_3CN. Product yields were determined by peak area ratios relative to the standard samples by different (like NMR and ESI-MS) spectroscopic techniques.

2.7. References

1. W. L. F. Armarego in *Purification of Laboratory Chemicals*, (Ed: D. D. Perrin), Pergamon Press, Oxford, **1997**.
2. H. Saltzman, in *Organic Syntheses*, Vol. V (Ed: J. G. Sharefkin), Wiley, New York, **1973**, pp. 658.
3. D. Macikenas, E. Skrzypczak-Jankun, J. D. Protasiewicz, *J. Am. Chem. Soc*. **1999**, *121*, 7164-7165.
4. A. Lewandowska-Andralojc, D. C. Grills, J. Zhang, R. M. Bullock, A. Miyazawa, Y. Kawanishi, E. Fujita, *J. Am. Chem. Soc*. **2014**, *136*, 3572–3578.
5. A. Company, G. Sabenya, M. Gonzalez-Bejar, L. Gomez, L, M. Clemancey, G. Blondin, A. J. Jasniewski, M. Puri, W. R. Browne, J.-M. Latour, L. Que Jr, M. Costas, J. Perez-Prieto, J. Lloret-Fillol, *J. Am. Chem. Soc*. **2014**, *136*, 4624–4633.
6. D. Zhang, D. H. Busch, N. W. Alcock, *Bull. Korean. Chem. Soc.* **1998**, *19*, 895-1018.
7. W. Szulbinski , P. R. Warburton , D. H. Busch , N. W. Alcock , *Inorg. Chem.* **1993**, *32*, 297 –302.
8. A. K. Vardhaman, P. Barman, S. Kumar, C. V. Sastri, D. Kumar, S. P. de Visser, *Chem. Commun.* **2013**, *49*, 10926–10928.

9. T. Nakajima, Y. Kawasaki, B. Kure, T. Tanase, *Eur. J. Inorg. Chem.* **2016**, 4701–4710.
10. R. R. Fernandes, J. Lasri, M. F. C. G. da Silva, J. A. L. da Silva, J. J. R. F. da Silva, A. J. L. Pombeiro, *J. Mol. Catal. A: Chem.* **2011**, *351*, 100-111.
11. P. Comba, B. Kanellakopulos, C. Katsichtis, A. Lienke, H. Pritzkow, F. J. Rominger, Chem. Soc., Dalton Trans. 1998, 3997− 4001.
12. P. Barman, A. K. Vardhaman, B. Martin, S. J. Wörner, C. V. Sastri, P. Comba, Angew. Chem., Int. Ed. 2015, 54, 2095−2099.
13. N. A. Barnes, A. T. Brooker, S. M. Godfrey, P. R. Mallender, R. G. Pritchard, M. Sadler, Eur. J. Org. Chem. 2008, 6, 1019-1030.
14. L. Duelund, R. Hazell, C. J. McKenzie, L. P. Nielsen, H. Toftlund, J. Chem. Soc., Dalton Trans. 2001, 152–156.
15. R. H. Holm, G. W. Everett Jr., W. D. Horrocks Jr., J. Am. Chem. Soc. 1966, 88, 1071-1073.
16. J. A. Happe, R. L. Ward, J. Chem. Phvs. 1963, 39, 1211-1218.

CHAPTER – III

Enhanced Reactivity through Equatorial Sulfur Coordination in Nonheme Iron(IV)-Oxo Complexes: Insights from Experiment and Theory.

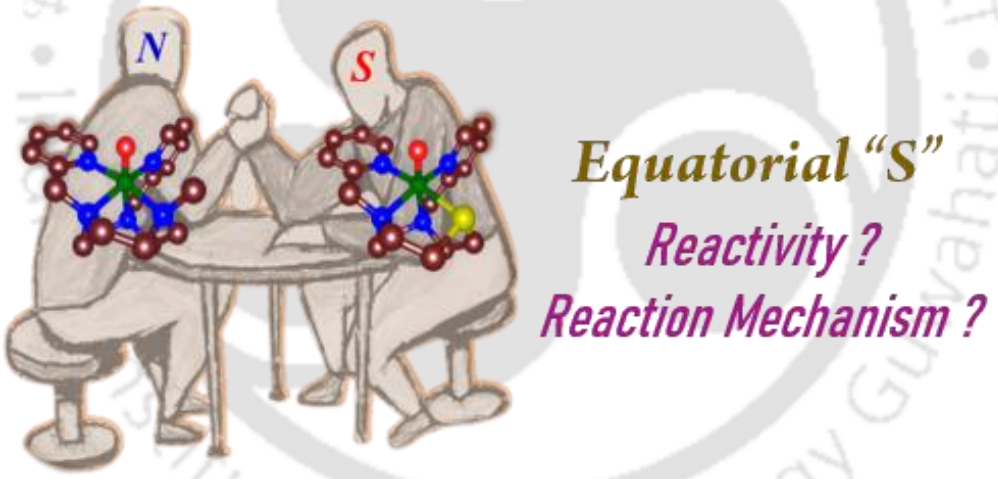

● Adapted from *Inorganic Chemistry*, **2024**, *63 (15)*, 6752-6766 with permission from the American Chemical Society ●

3.1. Introduction

Oxygen-activating metalloenzymes have unique structure and properties and catalyze a vast range of chemical reactions in nature under physiological conditions.[1-3] Many of these metalloenzymes utilize iron that is bound to the protein with interactions from amino acid side chains that are often histidine or carboxylate groups (of Asp or Glu). However, a considerable number of metalloenzymes bind the metal ion either via an axial or equatorial cysteinate residue of the protein. These differences in ligand coordination of the metalloenzyme often are associated with its function and properties. For instance, structures of the cytochromes P450 (P450) and the nitric oxide synthases have been determined and shown them to contain an iron-heme cofactor bound to the protein through a cysteinate linkage (Figure 3.1a).[4-7] This cysteinate axial ligand not only provides an anchor for the heme in the protein structure but induces a push-effect on the metal-heme center that is believed to have significant effect on the basicity and the redox potential of the metal-oxygen bond thereby enhancing its chemical catalysis for oxygen atom transfer reactions.[8-10] The widely explored class of P450 enzymes catalyze a large variety of regioselective and stereospecific substrate hydroxylation and epoxidation reactions as part of the metabolism of xenobiotics in the liver or for the biosynthesis of natural products.[11-16] Consequently, the P450s are important oxidants in most biosystems and highly versatile. The catalytic cycle of the P450s uses two reduction equivalents, a molecule of dioxygen and two protons from the solvent to generate a high-valent iron(IV)–oxo heme π-cation radical species called Compound I, Cpd I.[17-19] Cpd I has been spectroscopically characterized and isolated for the camphor hydroxylating isozyme $P450_{CAM}$ and shown to react via hydrogen atom abstraction from its substrate.[20] The strong electron-donation by the axially ligated cysteinate ligand was shown to enhance

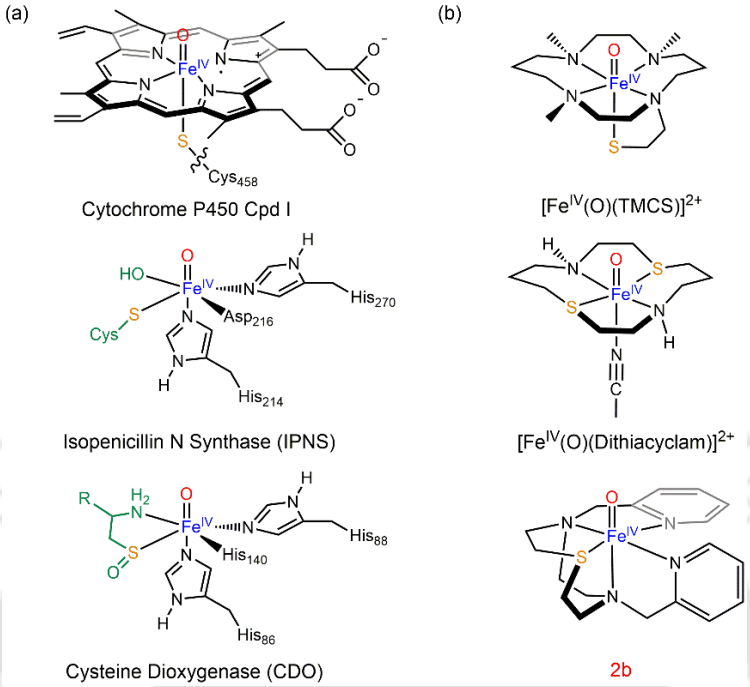

Figure. 3.1. (a) Proposed Structures of Hypothesized Sulfur-Ligated Iron(IV)-Oxo Reactive Intermediates in Biology. (b) Examples of Biomimetic Sulfur-Ligated Iron(IV)-Oxo Models: $[Fe^{IV}(O)(TMCS)]^{+}$, $[Fe^{IV}(O)(dithiacyclam)]^{2+}$ and **2b**.

the basicity of the iron(IV)-oxo core in Cpd I and thereby enabled a hydrogen atom abstraction reaction at a lowered redox potential.[21]

Several nonheme iron enzymes utilize a cysteinate amino acid as a substrate that binds directly to the iron center either as an amino acid monomer or as part of a peptide chain. Examples of these nonheme iron enzymes include isopenicillin *N* synthase (IPNS),[22,23] cysteine dioxygenase (CDO),[24-29] the ergothioneine biosynthesis protein EgtB,[30] and mercaptopropionate dioxygenase (MDO).[31,32] All of these enzymes react O_2 on an iron(II) center and have been proposed to form an iron(IV)-oxo intermediate, although these have never been trapped and characterized. Scheme 1a shows the active site structures of the iron(IV)-oxo intermediates of IPNS and CDO for comparison. Interestingly, in contrast to most nonheme iron dioxygenases that have a facial metal-coordination with two

histidine and one carboxylate group of either an Asp or Glu residue, these equatorially ligated sulfur-bound enzymes like CDO, EgtB and MDO bind the metal to three histidine groups and no Asp/Glu is directly bound to iron.[33-39] Computational studies on wildtype CDO as compared to CDO variants with an anionic equatorial ligand rather than a neutral His ligand explored the cysteine dioxygenation reaction differences.[40] The work showed weakening of the iron-sulfur bond upon binding of an anionic equatorial ligand leading to major changes to the kinetics of oxygen atom transfer reactions. Therefore, the ligand environment and the first-coordination sphere of iron centers are important and a sulfur coordination may lead to changes of chemical properties of the metal center and influence its reactivity.

Although, equatorially-bound sulfur ligands play an important role in various nonheme metalloenzymes, there is a lack of understanding on the effect of these ligands on the structure and reactivity of iron(IV)-oxo cores. These iron(IV)-oxo moieties are key intermediates in enzymes and believed to be responsible for the majority of the oxygen atom transfer reactivities in nature. As a consequence, many groups have created synthetic analogues, i.e., biomimetic models, to gain insight into their structure and reactivity.[41-46] The use of small-molecule complexes designed to mimic the active site of short-lived high-valent enzymatic intermediates has significantly enhanced our understanding of the catalytic cycles of heme and nonheme iron dioxygenases. Despite all these efforts, the synthesis of an iron(IV)-oxo porphyrin complex with a thiolate ligand has not yet been reported. On the other hand, several nonheme iron complexes have been reported that bear a thiolate or thioether group as part of the ligand framework. One of the earliest examples of those that was characterized is the $[Fe^{IV}(O)(TMCS)]^{+}$ complex, TMCS = 1-mercaptoethyl-4,8,11-trimethyl-1,4,8,11-tetraaza-cyclotetradecane, shown in Scheme 1b.[47] The complex was characterized with UV-visible, resonance

Raman and Mössbauer spectroscopic methods and its crystal structure coordinates were determined. The reaction of $[Fe^{IV}(O)(TMCS)]^{+}$ with 9,10-dehydroanthracene (DHA) established a rate-determining hydrogen atom abstraction with a large kinetic isotope effect (KIE) for the replacement of hydrogen by deuterium atoms in the substrate with a KIE = 80. It was proposed that this large KIE value is the result of the electron-donor abilities of the axial thiolate ligand resulting in large amount of quantum chemical tunneling.[48] As the synthesis of biomimetic heme and nonheme iron(IV)-oxo complexes with thiolate ligand (either axial or equatorial) remains challenging, the efforts in the field have shifted to neutral sulfur ligands, i.e. thioethers, and for several complexes stable structures could be characterized. As the oxidation state and overall charge of thioethers is different from thiolates there may be quantum mechanical differences between the two complexes but they should have the same stereochemical interactions. These studies triggered biomimetic studies on sulfur-ligated iron(II) complexes as mimics of thiol dioxygenases in nature, although in none of those an iron(IV)-oxo species could be trapped.[49-54]

More recently, a nonheme iron(IV)-oxo complex with equatorial sulfur ligand was reported, namely the complex $[Fe^{IV}(O)(Me_3TACN)(S_2Si(CH_3)_2)]$ with Me_3TACN = 1,4,7-trimethyl-1,4,7-triazacyclononane.[55] Due to thermal instability of the complex reactivity studies and rate measurements could not be performed. Further efforts from Ray and co-workers focused on an iron(IV)-oxo complex with sulfur-containing cyclam ligand, namely $[Fe^{IV}(O)(dithiacyclam)(CH_3CN)]^{2+}$ with dithiacyclam = 1,8-dithia-4,11-diazacyclotetradecane.[56] This system contains two sulfur coordination sites in the equatorial plane of the iron(IV)-oxo species.[56] The authors proposed that introducing the sulfur groups in the equatorial position weakens the Fe-O bond and enhances its oxidative reactivity with a diminished deuterium kinetic isotope effect. Their results are in sharp contrast to the earlier

report on $[Fe^{IV}(O)(TMCS)]^{+}$.[47] On the other hand, the substitution of the *N*-methyl groups in the tetramethylcyclam scaffold with oxygen atoms resulted in a rate enhancement for hydrogen atom abstraction (HAT) and oxygen atom transfer (OAT) by five to six orders of magnitude as compared to its parent complex.[57] It was suggested that the rate enhancement may be due to the higher electrophilicity of the iron center as a result of the equatorial oxygen atoms as compared to *N*-methyl groups. Recently, Kaur and Mandal reported a thorough computational study on the role of equatorial sulfur substitution on the C-H activation reactivity of iron(IV)-oxo cyclam complexes.[58] Their results show that with the enrichment of sulfur atoms into the ligand scaffold resulted in the increased reactivity successively along the series $N_4 < N_3S < S_2N_2 < S_3N < S_4$.[58]

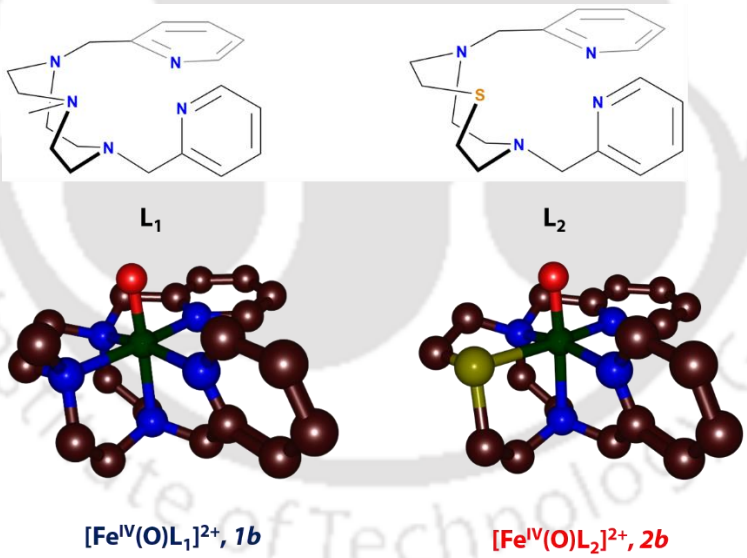

Figure. 3.2. Ligand frameworks (*top*) studied and DFT-optimised structures of the corresponding iron(IV)-oxo complexes.

To gain further insight into equatorial sulfur positioning in nonheme iron(IV)-oxo complexes, we report here a novel N_4S-ligated iron(IV)-oxo complex

(**2b**) and compare its structure and reactivity with the corresponding N_5-ligated iron(IV)-oxo complex (**1b**), see Figure 3.2 for their structures. In particular, we report the synthesis and characterization of the stable N_5- and N_4S-ligated iron(IV)-oxo complexes. The $[Fe^{IV}(O)(L_2)]^{2+}$ (**2b**) (L_2 = 1-thia-4,7-bis(2-pyridylmethyl)-diazacyclononane) was synthesized at room temperature and characterized with spectroscopic techniques and reacted with model substrates. In addition, we investigated the reactivity patterns for a system (**1b**), where the thioether sulfur ligand in **2b** was replaced by an *N*-methyl moiety in the parent ligand framework. A detailed experimental and computational study shows that a sulfur atom in the equatorial plane affects the redox potentials and enables faster electron transfer, thereby resulting in hydride abstraction instead of hydrogen atom abstraction.

3.2. Results and Discussion

3.2.1. Synthesis and Characterization

Ligands L_1 and L_2 were synthesized and characterized (See figures 2.5 & 2.6) according to reported procedures.[61-64] Subsequently, the L_1 and L_2 ligands were reacted with $[Fe^{II}(CH_3CN)_2(OTf)_2]$ with OTf = triflate in acetonitrile under inert atmosphere inside the glovebox to form the corresponding iron(II) complexes: $[Fe^{II}(L_1)(CH_3CN)](OTf)_2$ (1a) and $[Fe^{II}(L_2)(CH_3CN)](OTf)_2$ (2a).[63,64] These iron(II) complexes were characterized with UV-vis absorption spectroscopy, cyclic voltammetry (CV), NMR spectroscopy and electrospray ionization mass spectrometry (ESI-MS) (see Fig. 2.14 and 2.15, Chapter-II). Treatment of **1a** with 1.5 equivalents of iodosylbenzene (PhIO) or *n*-$BuNIO_4$ in CH_3CN under ambient conditions generated the corresponding iron(IV)-oxo complex $[Fe^{IV}(O)(L_1)]^{2+}$, **1b**. UV-vis absorption characterized the iron(IV)-oxo complex with a $\lambda_{max,\mathbf{1b}}$ = 737 nm ($\varepsilon_{\mathbf{1b}}$ = 310 M^{-1} cm^{-1}) with a half-life of 30 minutes, Figure 2a. These values are similar to those reported by Company et al.[64] Complex **2b** was synthesized following the same approach as **1b** and its characterization

with UV-vis absorption spectroscopy and ESI-MS is shown in Figure 3.3a. The UV-vis absorption spectrum of $[Fe^{IV}(O)(L_2)]^{2+}$, **2b**, gives an absorption band at $\lambda_{max,\mathbf{2b}}$ = 730 nm ($\varepsilon_{\mathbf{2b}}$ = 165 M^{-1} cm^{-1}) with a half-life of 60 minutes. As far as we know, this would be the first report of a sulfur-ligated nonheme iron(IV)-oxo complex to be found stable at room temperature. Moreover, the substitution of the *N*-methyl moiety in L_1 by a sulfur atom to obtain L_2 resulted in an iron(IV)-oxo species with hypsochromic shift of the d-d transition band by 7 nm. This is further indication of a change in the first-coordination sphere and indicative of sulfur binding to the metal.

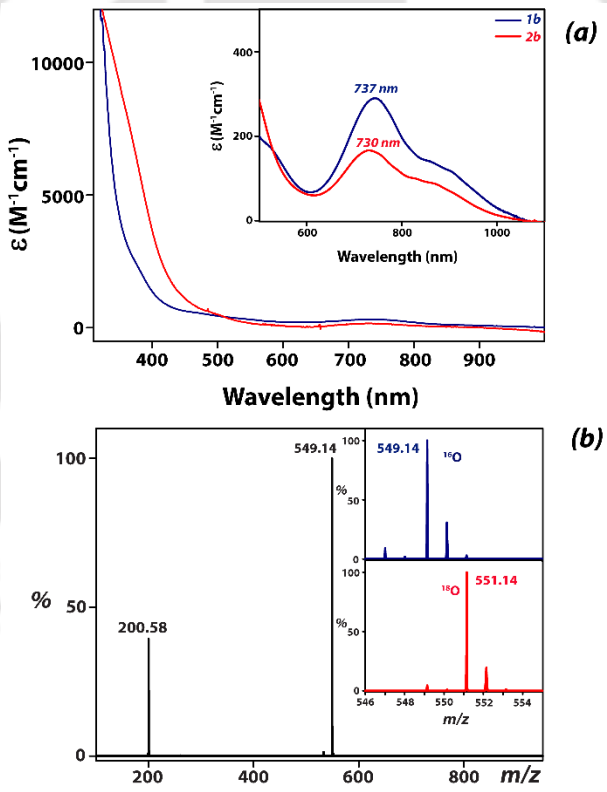

Figure. 3.3. (a) UV-vis spectra of **1b** (blue) and **2b** (red) in CH_3CN at 298 K. (b) Electrospray ionization mass spectra of **2b** in CH_3CN at 298 K. The in-set shows expanded isotopic distribution patterns of $[Fe^{IV}(^{16}O)(L_2)(OTf)]^+$ (in blue) and $[Fe^{IV}(^{18}O)(L_2)(OTf)]^+$ (in red).

The ESI-MS spectrum of **2b** shows prominent peaks at m/z 549.14 and m/z 200.58 corresponding to the $[Fe^{IV}(O)(L_2)(OTf)]^+$ and $[Fe^{IV}(O)(L_2)]^{2+}$ ions, respectively (Figure 3.3b). The isotopic distribution patterns for the two species confirms their assignments. The formation of the $[Fe^{IV}(O)(L_2)(OTf)]^+$ species was further established by an isotopic labelling experiment using $H_2{}^{18}O$, which leads to oxygen atom exchange with the oxo group. The experiment with $H_2{}^{18}O$ moves the peak in the ESI-MS spectrum for $[Fe^{IV}(O)(L_2)(OTf)]^+$ from m/z 549.14 to m/z 551.14, while the peak representing the $[Fe^{IV}(O)(L_2)]^{2+}$ ion shifts by one unit. Hence the isotopic labelling experiment confirms that one oxygen atom is incorporated into the metal complex in the form of an iron(IV)-oxo species.

3.2.2. Reaction Kinetics

In order to find out whether the change in spectroscopic properties of the oxidant (**2b** versus **1b**) has an effect on the oxidation properties, we did a thorough kinetics study using a range of different substrates. In particular, thioanisole was employed as the substrate to assess the oxygen atom transfer (OAT) reactivity, while a range of substrates with varying C–H bond strengths were tested for hydrogen atom transfer (HAT) pathways. The addition of substrates to a solution containing **1b** or **2b** in acetonitrile led to the decay of the characteristic d-d transition band in the UV-vis spectrum, which enabled us to obtain their pseudo-first-order rate constants. The second-order rate constants (k_2) were subsequently determined by plotting the pseudo-first-order rate constants (k_{obs}) as a function of the relative increment of the substrate concentration. Generally, sulfoxidation reactions proceed via a concerted oxygen atom transfer to the sulfur atom of the organic substrate, resulting in the formation of sulfoxides as the oxidized products. The addition of thioanisole to **2b** at 283 K led to the decay of the iron(IV)-oxo characteristic band at 730 nm in the UV-vis spectrum (Figure 3.4a), thereby

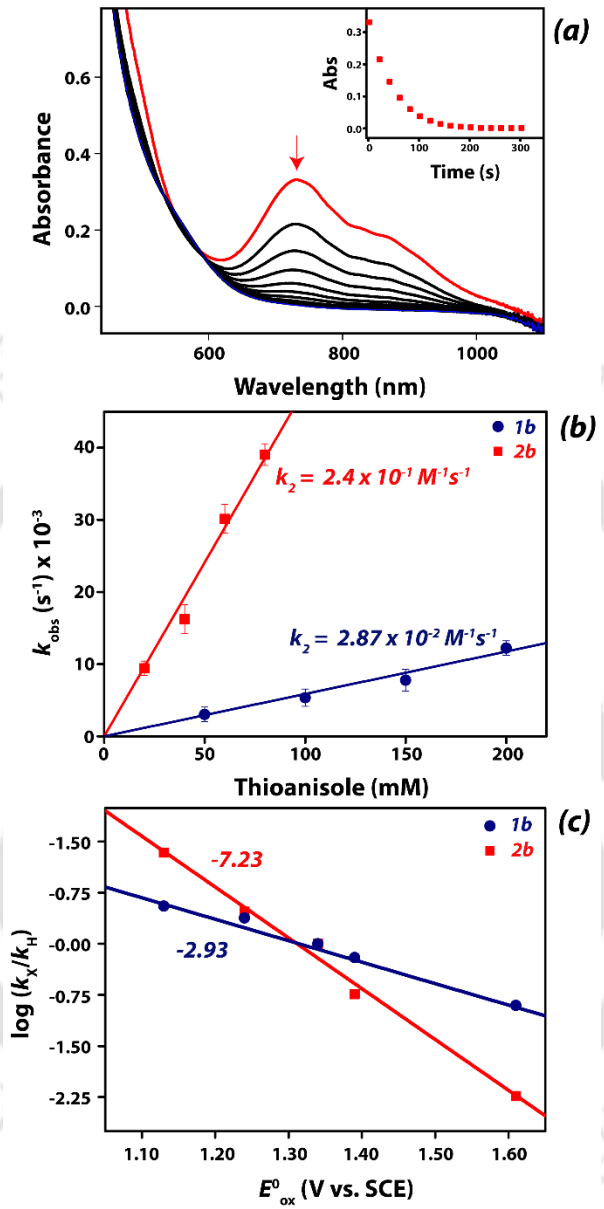

Figure. 3.4. (a) UV-vis spectral changes of **2b** upon addition of 40 equiv. of thioanisole in CH_3CN at 283 K. Inset shows the decay profile of the 730 nm band. (b) The second-order rate constant determined for the reaction of **1b** (2 mM) and **2b** (2 mM) with thioanisole at 283 K. (c) plot of log(k_X/k_H) against one-electron oxidation potentials ($E°_{ox}$) of *p*-X-thioanisole in their reaction with **1b** and **2b** at 283 K in CH_3CN, where k_X and k_H are the pseudo first-order rate constants of *p*-X-thioanisole and thioanisole, respectively.

producing methylphenylsulfoxide as the major product. The UV-vis spectra were monitored for changes in absorbance at 730 nm as a function of time, which allowed us to determine the pseudo-first-order rate constant (k_{obs}) for the reaction.

These observed rate constants were converted into second-order rate constants (k_2) from the slope of the k_{obs} values as a function of substrate concentration (Figure 3.4b). The second-order rate constant (k_2) for the reaction of thioanisole with **2b** was evaluated to be 2.40×10^{-1} M^{-1} s^{-1} at 283 K. Subsequently, the reaction of thioanisole with **1b** under the same reaction conditions was measured and a second-order rate constant of 2.87×10^{-2} M^{-1} s^{-1} was determined. Therefore, under the same experimental conditions, the reactivity of **2b** with thioanisole is about 9 times faster than that of **1b** (Figure 3.4b). Clearly, the introduction of a sulfur heteroatom in the equatorial position in the ligand framework enhances the reactivity.

To gain a deeper understanding into the reaction mechanism, we investigated the reaction of **1b** and **2b** with *p*-X-substituted thioanisole substrates with X = OCH_3, CH_3, H, Cl and CN. Thus, these *para*-substituents influence the charge distributions and thereby give a measure of the strength of electron transfer in the rate-determining transition state that is measured from the slope of the plot of the natural of the rate constant versus the Hammett σ_P parameter.[78-81] Second-order rate constants were measured for each substrate (Supporting Information, Table S1) and plotted as the logarithm of the rate constant ratio (k_X/k_H) as a function of the σ_p Hammett values [82,83] (Figure S21, Supporting Information). For the reaction of *p*-X-substituted thioanisole substrates with **1b**/**2b** a linear correlation between the σ_P Hammett value and $\log(k_X/k_H)$ is found with a slope of $\rho = -1.54$ and $\rho = -3.67$ for **1b** and **2b**, respectively (Figure S21, Supporting Information). To accommodate the additional stabilization of the positive charge in the transition

state, new Hammett plots were also made using σ_P^+ values leading to slope ρ values of –0.82 and –2.08, respectively, for **1b** and **2b** (Supporting Information, Figure S22). The large Hammett values obtained for **2b** can be explained on the basis of additional stabilization of positive charge in the transition state by electron-donating groups in the *para*-position of thioanisole. The differences in the Hammett slopes for **1b** and **2b** implicate that the two oxidants react with thioanisole through a different reaction mechanism. In particular, a slope of ρ = –1.54 is typical for an atom transfer reaction,[76,84,85] whereas a relatively larger slope with a value of ρ = –3.67 would indicate an electron transfer mechanism.[78,80] Similarly, when the logarithm of the rate constant ratio was plotted against the one-electron redox potential ($E°_{ox}$) of the substrates also a linear correlation was obtained. The plots of the logarithm of the rate constant ratio (k_X/k_H) versus the redox potential of the substrate has a slope of –2.93 and –7.23 for **1b** and **2b**, respectively (Figure 3.4c). As far as we know, it has never been observed previously to have changes in a reaction mechanism as a result of equatorial ligand field perturbation around nonheme iron(IV)-oxo centers. Nevertheless, there have been reports on rate-enhancement upon equatorial ligand perturbations in iron(IV)-oxo complex reactivities. For example, alkyl/aryl substitution at the sixth position in the pyridine ring of methylene carbon of N4Py ligand framework resulted in a rate enhancement, but no change in reaction mechanism and selectivity was observed.[84,85] However, the example shown here is a one of a kind where a subtle change in the ligand framework leads to a switch in the reaction mechanism from oxygen atom transfer to electron transfer.

Table 3.1. Second-order rate constants (k_2) determined for the reaction of **1b** and **2b** (2 mM solution in CH_3CN) with various *para*-X-substituted thioanisole substrates in CH_3CN at 283 K.[a]

***p*-X**[b]	σ_p [c]	σ_p^+ [c]	$E°_{oxd}$ [d]	**Complex**	k_2 ($\times 10^{-2}$ M^{-1} s^{-1}) [e]	k_X/k_H [f]	$\log(k_X/k_H)$
-OMe	–0.27	–0.78	1.13	**1b**	10.3(2)	3.57	0.55
				2b	1086(3)	45.18	1.33
-Me	–0.17	–0.31	1.24	**1b**	6.86(1)	2.39	0.37
				2b	41.9(2)	1.74	0.24
-H	0.00	0.00	1.34	**1b**	2.87(4)	1.0	0.0
				2b	24.0(2)	1.0	0.0
-Cl	0.23	0.11	1.37	**1b**	1.81(3)	0.62	–0.20
				2b	4.39(1)	0.18	–0.73
-CN	0.68	0.66	1.61	**1b**	0.35(2)	0.125	–0.90
				2b	0.16(3)	0.0058	–2.23

[a] All the reactions were followed by monitoring the UV/Vis spectral changes of the reaction solution. [b] *para*-substituents in *para*-X-thioanisole. [c] Data taken from ref. 74. [d] Data taken from ref. 75. [e] In s^{-1}. [f] Relative rate constant obtained by dividing the k_{obs} of *p*-X-thioanisole by k_{obs} of *p*-H-thioanisole.

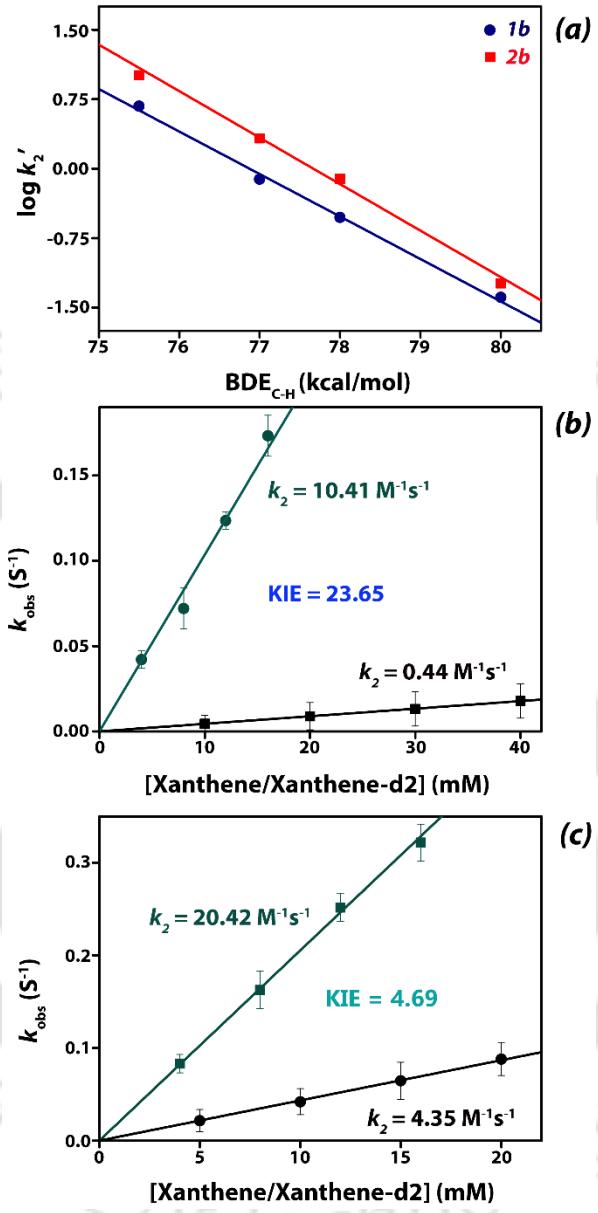

Figure. 3.5. (a) plot of the logarithms of the second-order rate constants (log k_2') vs. the C–H BDEs of the substrates with **1b** and **2b** in CH_3CN at 233 K. (b) Plots of the pseudo-first order rate constants k_{obs} vs. the substrate concentrations for xanthene and xanthene-[D_2] and the obtained kinetic isotopic effect (KIE) for the reaction with **1b** with xanthene in CH_3CN at 233 K. (c) Plots of the pseudo-first order rate constants k_{obs} vs. substrate concentration for xanthene and xanthene-[D_2] and the obtained KIE for the reaction of **2b** with xanthene in CH_3CN at 233 K.

Encouraged by the *S*-oxidation results, we then decided to study the C–H bond activation by **1b** and **2b**. The obtained second order rate constants for these reactions are given in Supporting Information, Table S2. Previous studies have demonstrated that reactions involving a rate-determining hydrogen atom abstraction step show a linear relationship between the natural logarithm of the second-order rate constant and the C–H bond dissociation energy ($BDE_{C–H}$).[86-90] In particular, we investigated the hydrogen atom abstraction reactions of **1b** and **2b** with substrates with known C–H bond strengths, namely xanthene, 9,10-dihydroanthracene (DHA), 1,4-cyclohexadiene (CHD) and fluorene. These substrates span a range of C–H bond dissociation energies ($BDE_{C–H}$) from 75 to 80 kcal mol^{-1} (Table 3.

2) and hence should elucidate the thermodynamics behind the HAT reaction rates by **1b** and **2b**. Next, we plotted the natural logarithm of the second-order rate constants for HAT by **1b**/**2b** versus the $BDE_{C–H}$ of the substrates, see Figure 3.5a. The linearity and the non-zero slope value of the Bell-Evans-Polanyi plot (log k_2' versus $BDE_{C–H}$) gives evidence of a rate-determining hydrogen atom abstraction reaction. Moreover, a larger slope in the curve is seen for **2b** than **1b**, which implies that the introduction of an equatorial sulfur ligand to the iron(IV)-oxo species exhibits a significant effect on its reactivity. In reactions with substrates containing C–H bonds such as those in xanthene, CHD, DHA and fluorene, **2b** reacts at least with a *2 to 4 times* faster rate than **1b** (Table 3.2).

To gain further insight into the reaction mechanism we employed xanthene-[D_2] as a substrate and repeated the experiments with **1b** and **2b**. In both experiments the second-order rate constant is considerably lower when xanthene-[D_2] is used leading to a kinetic isotope effect (KIE, k_H/k_D) of $KIE_{\mathbf{1b}}$ = 23.7 for the reactions with **1b** and $KIE_{\mathbf{2b}}$ = 4.7 with **2b** as oxidant (Figures 3.5b and 3.5c). Therefore, **2b**

reacts with a considerably lower kinetic isotope effect and consequently experiences much lesser quantum chemical tunneling than the corresponding reaction of **1b** with xanthene. These results are in agreement with the diminished KIE value reported for the $[Fe^{IV}(O)(N_2S_2)]^+$ complex studied by Deutscher et al.[56] In particular, they also observed that upon equatorial sulfur substitution in place of an N–H moiety (KIE = 20), there is a drop in the KIE for hydrogen versus deuterium abstraction from the substrate to values of 1.5 and 2.8 when xanthene and DHA are employed, respectively. Nevertheless, when the logarithms of the second order rate constants (log k_2') are plotted versus the $BDE_{C–H}$ values of the substrates, a linear correlation is found for the reactions involving **1b** and **2b** with substrates (Figure 3.5a).

The process of hydrogen atom abstraction generally involves the simultaneous transfer of a proton and electron. However, it is important to note that the rate is influenced differently by the transfer of the proton and the electron. While proton transfer plays a significant role in determining the rate of oxidation of C–H bonds by **1b**, there is also a substantial contribution from quantum chemical tunneling in the hydrogen atom transfer (HAT). This phenomenon is commonly observed in HAT reactions mediated by high-valent metal-oxo species in both enzymes and biomimetic models.[91-96] By contrast, the system with equatorial sulfur ligand shows much smaller KIE and lesser tunneling effects. Klein et al[48] proposed that the axial thiolate ligand of $[Fe^{IV}(O)(TMCS)]^+$ plays a unique role in facilitating quantum chemical tunneling, thereby resulting in a large KIE of 80 for hydrogen atom abstraction from DHA. The equatorial sulfur ligation, in contrast, has been shown to have a diminishing effect on the tunneling contribution, resulting in a reduced KIE value. The effect of *N* versus *S* donors in an otherwise identical ligand environment is also reflected in the enhanced oxygen atom transfer (OAT) ability of **2b** relative to **1b** (Table 3.1). The switch in the reaction mechanism for

sulfoxidation and HAT reactions are well established with different kind of metal-intermediates and, for instance, shown in the comparison of the reactivity of iron(IV)-oxo versus iron(IV)-tosylimido.[81,97-99]

Table 3.2. C–H Bond dissociation energies and second-order rate constant values for the reaction of **1b** (2 mM) and **2b** (2 mM) with various substrates in CH_3CN at 233 K.

Substrate [a]	*BDE_{C-H} (kcal mol^{-1})* [b]	*$BDFE_{C-H}$ (kcal mol^{-1})* [c]	*Complex*	*k_2 (M^{-1} s^{-1})* [c]	*k_2'* [d]	*log (k_2')*
Xanthene (2)	75.5	73.3	**1b** **2b**	10.4(3) 20.4(4)	5.205 10.21	0.71 1.00
9,10-Dihydroanthracene (4)	77	76	**1b** **2b**	2.63(1) 8.51(2)	0.65 2.12	–0.18 0.32
1,4-Cyclohexadiene (4)	78	-	**1b** **2b**	1.19(1) 4.18(3)	0.297 1.045	–0.52 0.019
Fluorene (2)	80	77.4	**1b** **2b**	0.082(2) 0.107(4)	0.041 0.053	–1.38 –1.27

[a] The number in the parenthesis indicates the number of equivalent H-atoms on the substrate that can react with the iron(IV)-oxo species. [b] from Ref 6. [c] from Ref 7. [d] In M^{-1} s^{-1}. [e] The k_2' values are obtained by dividing k_2 values by the number of equivalent hydrogen atoms in the substrate that would react with the iron(IV)-oxo species.

3.2.3. Computational Backup

To gain further insight into the electronic and chemical differences of complexes **1b** and **2b** we did a computational study on their structure, properties and reactivity. Accordingly, the reaction mechanism of C–H activation from CHD and *S*-oxidation of dimethylsulfide (DMS) by **1b** and **2b** was studied as model substrates for those reactions. The choice of DMS for computational studies was based on comparable one electron oxidation potential to that of thioanisole. Let us start with discussing the structural and electronic differences of both systems first. Both **1b** and **2b** have a triplet spin ground state by more than 5 kcal mol^{-1} with respect to their nearest quintet state. This matches experimental data on **1b** and

analogous nonheme iron(IV)-oxo complexes that were characterized as a triplet ground state.[95] The Fe–O bond lengths in **1b** and **2b** are short (1.62-1.63 Å) for all spin states, and are representative of a double bond. These Fe–O values are analogous to other nonheme iron biomimetic systems crystallography characterized or obtained from DFT calculations.[100-116] The bond length between iron and the axial nitrogen atom (Fe–N_{ax}) is fairly constant among all structures. After substituting the *N*-methyl group in **1b** by a sulfur atom to obtain **2b**, a considerable lengthening of the metal-ligand bond is observed as expected for the interaction of two second-row elements.

Regardless of the differences in the equatorial plane of the system for **1b** versus **2b**, both are in a triplet spin ground state with the same electronic configuration and orbital occupation as: $\delta_{xy}^2\ \pi^*_{xz}{}^1\ \pi^*_{yz}{}^1$, whereby the *z*-axis is defined as along the Fe–O bond. By contrast, the quintet spin state has configuration $\delta_{xy}{}^1\ \pi^*_{xz}{}^1\ \pi^*_{yz}{}^1\ \sigma^*_{x2\text{-}y2}{}^1$. As such the molecular orbitals originating from the 3d-block of metal orbitals is occupied by four electrons in the iron(IV)-oxo species with a low-energy π^*_{xy} orbital in the plane of four Fe–N interactions in **1b**, while in **2b**, the 3d orbital interacts with three nitrogen atoms and the sulfur ligand. The π^*_{xz} and π^*_{yz} orbitals are the antibonding metal-oxo interactions and have little involvement of the equatorial atoms, while the $\sigma^*_{z}2$ is also along this bond but σ-type. The valence orbitals show little differences between those for **1b** and **2b**. The lowest energy orbital for both complexes is the δ_{xy} orbital with its lobes placed between the four equatorial nitrogen atoms in **1b** and interacting with the sulfur in **2b**. Although the orbital

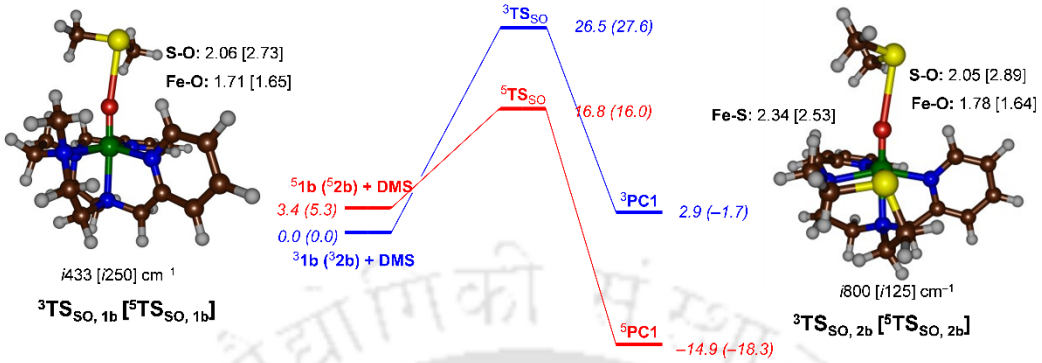

Figure. 3.6. UB3LYP calculated potential energy landscape for DMS sulfoxidation by **1b** and **2b** (data for **2b** in parenthesis). Free energies (in kcal mol^{-1}) use UB3LYP/BS2 energies, and 298 K zero-point, thermal and entropic corrections at UB3LYP/BS1 level of theory. Optimized transition state structures give distances in Å and the imaginary frequency in cm^{-1}.

lobes of the δ_{xy} orbital for **2b** are very similar, the orbital is stabilized by nearly 0.04 hartrees with respect to the one in the **1b** complex. The π_{xz}/π^*_{xz} and π_{yz}/π^*_{yz} pair of orbitals are degenerate for **1b** due to their symmetry but the pairs are not degenerated in **2b**. They appear to be stabilized in **2b** together with the σ* orbitals, which will affect its electron abstraction capability and its reactivity with substrates. The $\delta_{xy}/\sigma^*_{x2-y2}$ energy gap generally determines the triplet-quintet spin state ordering and splitting.[111] Indeed the stabilization of the δ_{xy} orbitals in ^{3}**2b** leads to a larger triplet-quintet energy gap of ΔG = 5.3 kcal mol^{-1} for **2b** as compared to ΔG = 3.4 kcal mol^{-1} for **1b**.

Subsequently, we investigated the sulfoxidation of DMS by **1b** and **2b** and the results are shown in Figure 3.6. The reactions start from a reactant complex of substrate DMS with iron(IV)-oxo species (^{3,5}**RC**), and after the transition state (^{3,5}**TS**$_{SO}$) leads to the formation of the product complex ^{3,5}**PC**. Sulfoxidation is a concerted one-step reaction, whereby a spin state crossing from the triplet to the quintet spin state takes place before the transition state. The calculated sulfoxidation barrier for DMS activation on the quintet spin state is $\Delta G^{\ddagger}$ = 16.8

kcal mol^{-1} for **1b**, while it is 16.0 kcal mol^{-1} for **2b**. Using transition state theory, the energy difference of those barriers will correspond to a rate enhancement of about 6 for **2b** over **1b**. Consequently, the calculated rate enhancement is in good agreement with the sulfoxidation rates measured experimentally that show a rate enhancement by an order of *9*. On the quintet spin state surfaces the overall reaction is strongly exergonic. The transition states on the quintet spin state surface are found to be earlier with short Fe–O and long S–O distances as compared to the triplet spin transition states, see Figure 3.6. The imaginary frequencies of the transition states represent S–O stretch vibrations and have magnitudes of i433 cm^{-1} for ^{3}**TS**$_{SO,1b}$, i120 cm^{-1} for ^{5}**TS**$_{SO,1b}$, i800 cm^{-1} for ^{3}**TS**$_{SO,2b}$ and i125 cm^{-1} for ^{5}**TS**$_{SO,2b}$. These values are of similar order of magnitude as previously calculated sulfoxidation transition states.[117-121]

An analysis of the electronic configurations and group spin densities and charges of the various complexes reveals that no early charge-transfer happens. In particular, the reactant complexes have the same charge and spin as the isolated species. This indicates that the mechanism is a direct oxygen atom transfer mechanism. For the quintet spin pathway the charge transfer from substrate to oxidant takes place after the transition state for both **1b** and **2b**, while it appears to be earlier for the triplet spin state surface. Although the Hammett plot indicates an early electron transfer this is not seen in the transition state structures from the spin densities. However, the calculated electron affinities of **1b** and **2b** are significantly different in line with the easier electron transfer to **2b** than **1b**. Thus, the sulfoxidation reaction leads to a change from iron(IV)-oxo to iron(II)-sulfoxide and the transfer of two electrons into the iron, which fills the $\sigma^*_{x^2-y^2}$ and $\sigma^*_{z^2}$ orbitals. While the triplet-quintet energy gap of the iron(IV)-oxo is determined by the filling of the $\sigma^*_{x^2-y^2}$ orbital, the rate-determining sulfoxidation step is determined by the transfer of an electron into $\sigma^*_{z^2}$ instead. Therefore, the triplet-

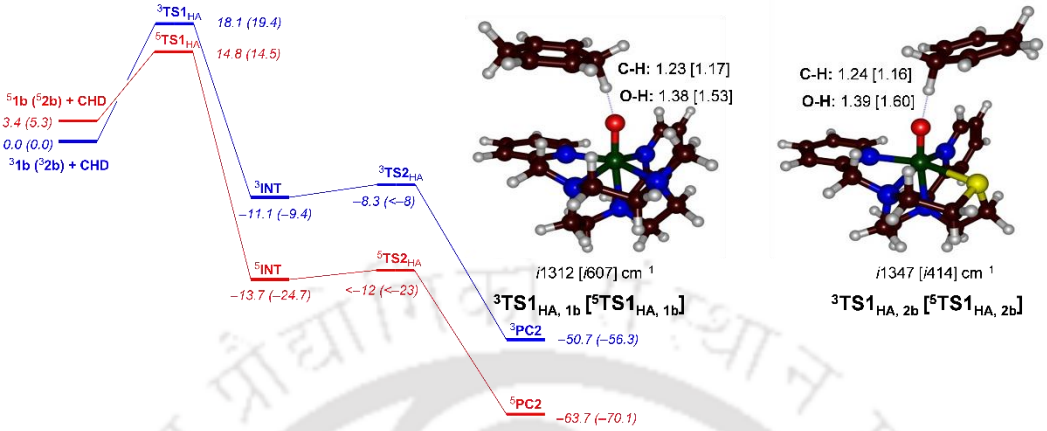

Figure. 3.7. UB3LYP calculated potential energy landscape for CHD dehydrogenation by **1b** and **2b** (data for **2b** in parenthesis). Free energies (in kcal mol^{-1}) use UB3LYP/BS2 energies, and 298 K zero-point, thermal and entropic corrections at UB3LYP/BS1 level of theory. Optimized transition state structures give distances in Å and the imaginary frequency in cm^{-1}.

quintet gap is larger for **2b** than **1b**, while the sulfoxidation barriers are reversed and lower in energy for **2b** as compared to **1b**.

Next, we investigated the mechanism for dehydrogenation of CHD by **1b**/**2b** and the DFT calculated potential energy profile is shown in Figure 6. The reaction is stepwise with two consecutive hydrogen atom abstraction steps via transition state **TS1**$_{HA}$ and **TS2**$_{HA}$ that separate a radical intermediate **INT**. The first hydrogen atom abstraction from CHD is rate-determining and free energies of activation of $\Delta G^{\ddagger}$ = 14.8 kcal mol^{-1} for **1b** and $\Delta G^{\ddagger}$ = 14.5 kcal mol^{-1} for **2b** are obtained. The difference between these two free energies of activation would correspond to a rate enhancement by a factor of 2 at 233 K, while experimentally a value of 3.5 is observed. Consequently, the calculations are in excellent agreement with the trends obtained experimentally. Moreover, the experimental rates of CHD activation by **1b**/**2b** of 1.19 and 4.18 M^{-1} s^{-1} would correspond to a free energy of activation at 233 K of $\Delta G^{\ddagger}$ = 13.4 and 12.9 kcal mol^{-1}, respectively.

The computationally obtained free energies of activation, therefore, are in excellent agreement with those measured experimentally.

Optimized geometries of the hydrogen atom abstraction transition states are shown in Figure 6. The triplet spin transition states have a large imaginary frequency of >i1300 cm^{-1} for the C–H–O stretch vibration and consequently will result in considerable amount of quantum chemical tunneling and a large kinetic isotope effect. Interestingly, both quintet spin transition states have a small imaginary frequency of only i607 cm^{-1} (for ^{5}**TS1**$_{HA,1b}$) and i414 cm^{-1} (for ^{5}**TS1**$_{HA,2b}$), although their animation still shows dominant hydrogen atom transfer. The reason for these low imaginary modes is likely because both quintet spin transition states are late on the potential energy surface with long O–H and short C–H bonds. Structurally both pairs of triplet spin transition states are alike with similar C–H and O–H distances for each spin state structure. The hydrogen atom transfer from CHD by **1b**/**2b** leads to a radical intermediate with large exergonicity and is followed by a small second hydrogen atom abstraction barrier via **TS2** to form benzene, water and an iron(II) complex. This mechanism is in line with previous studies on CHD activation by heme and nonheme iron(IV)-oxo complexes.[122,123]

Interestingly, a comparison of the CHD activation by **1b** and **2b** gives small differences. Thus, the triplet-quintet energy gap in the iron(III)-hydroxo intermediate (**INT**) is small for the reaction of **1b** with CHD (2.6 kcal mol^{-1}), whereas it is much larger for **2b** (15.3 kcal mol^{-1}). Therefore, there is a major difference in stability of the iron(III)-hydroxo complexes of the system with equatorial sulfur ligand as compared to the one without. An analysis of the group spin densities for the intermediate complexes shows that the ^{5}**INT**$_{1b}$ complex has a spin of −1.0 on the substrate which represents a down-spin electron, which

corresponds to an overall electronic configuration of $\delta_{xy}^1\ \pi^*_{xz}{}^1\ \pi^*_{yz}{}^1\ \sigma^*_{z}2^1\ \sigma^*_{x}2_{-y}2^1\ \varphi^1$. By contrast, the substrate moiety bears a total spin of 0.0 in ^{5}**INT**$_{2b}$. As such, ^{5}**INT**$_{2b}$ is the result of a hydride transfer, i.e. a proton and two electrons, as it has the configuration of the product complex with four metal-based orbitals singly occupied with configuration: $\delta_{xy}^2\ \pi^*_{xz}{}^1\ \pi^*_{yz}{}^1\ \sigma^*_{x}2_{-y}2^1\ \sigma^*_{z}2^1\ \varphi^0$. The latter highlights a strong asynchronicity of the desaturation process, whereby the second electron and proton transfer accompanying the overall hydrogen atom transfer are separated in time.[97,124,125] As a result, the second electron transfer happens early, namely together with the first hydrogen atom transfer, resulting in an initial hydride transfer step. This asynchronicity of the proton and electron transfer processes during the reaction mechanism will lead to low values of the imaginary frequency in the transition state.

Indeed, an analysis of the spin densities of the FeO and substrate moieties along the hydrogen atom transfer scan from the reactants complex to form **INT** shows a gradual accumulation of spin on the substrate for the reaction with **1b**. By contrast, for the reaction of **2b** with CHD in the first stage of the hydrogen transfer scan some unpaired spin density is accumulated on the substrate, however, when the scan approaches the intermediate state, i.e. at short O−H distances, the spin disappears from the substrate moiety again and creates an intermediate with an iron(II)-hydroxo coupled to a substrate cation. These results show that both reactions start with a hydrogen atom abstraction from the substrate, but the scan with **2b** is followed with a fast second electron transfer on or after the transition state to give an overall hydride transfer reaction. Further evidence that the reaction of ^{5}**2b** with CHD proceeds via hydride followed by proton transfer follows from the comparison of the group spin densities of ^{5}**INT**$_{2b}$ and ^{5}**TS2**$_{2b}$. Thus, in ^{5}**INT**$_{2b}$ the spin on the FeO group is 3.82, while the substrate spin is 0.01. These values do

not change much for ^{5}**TS2**$_{2b}$, and consequently ^{5}**TS2**$_{2b}$ happens through proton transfer.

In summary, **1b** reacts with CHD through two consecutive hydrogen atom abstraction reactions, while **2b** reacts via hydride transfer followed by proton transfer instead. Therefore, the equatorial sulfur ligand appears to influence the reduction potentials of the iron(IV)-oxo and iron(III)-hydroxo complexes and enable quicker electron transfer. The switch in mechanism from HAT to hydride transfer when we move from **1b** to **2b** may also be responsible for the lowering of the KIE with **1b**. In particular, it has been reported that hydride transfer tends to proceed with a low KIE with values of region of *2–5*, while typical KIE values for HAT are often well over 15.[126,127] Our KIE measurements, therefore, are indicative of hydride versus hydrogen atom transfer reactions as highlighted by the calculations.

As sulfur-based biomimetic complexes often suffer from ligand sulfoxidation,[128] we calculated the reaction of **2b** for internal sulfoxidation. These calculations give a concerted oxygen atom transfer, similarly to the sulfoxidation mechanism shown above in Figure 3.6 and matching thioether sulfoxidation as well as cysteine dioxygenase calculations reported previously.[119-121,129-132] Nevertheless, ligand sulfoxidation in **2b** encounters a transition state of ΔG = 25.0 kcal mol^{-1} on the quintet spin state with respect to ^{3}**2b**. This barrier is almost >9 kcal mol^{-1} higher in energy than the sulfoxidation transition state calculated for DMS by **2b**. Consequently, ligand sulfoxidation will be a slow process at room temperature and will not be able to compete with substrate sulfoxidation, although some ligand sulfoxidation may happen at low substrate concentrations.

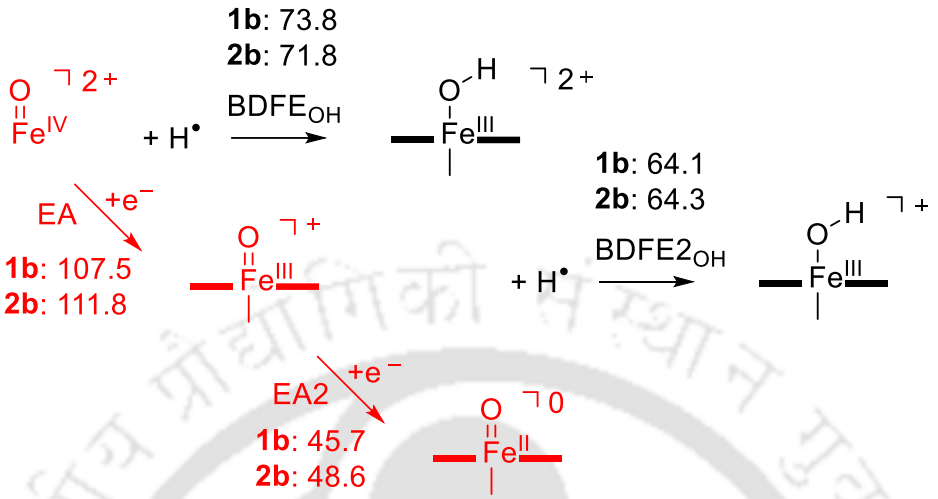

Figure. 3.8. UB3LYP/BS2 calculated electron affinities and $BDFE_{OH}$ values of reactant complexes. Free energies are given in kcal mol^{-1} and contain ZPE, thermal and entropic corrections.

To understand the differences in reaction mechanism for substrate activation by **1b** and **2b**, we investigated several thermochemical properties of these oxidants and determined a thermochemical cycle as described before.[133] We first calculated the bond dissociation free energy (BDFE) of the iron(III)-hydroxo complex to form the iron(IV)-oxo and a hydrogen atom. For **1b** and **2b** these $BDFE_{OH}$ values are within 2 kcal mol^{-1} and if hydrogen transfer is rate-determining, based on these small energy differences they are expected to react with similar rates. We then looked into possible electron transfer processes of **1b** and **2b** and calculated the adiabatic electron affinities (EA) of ^{3}**1b** and ^{3}**2b**, see Figure 7. In both cases the iron(III)-oxo species is in a quartet spin state and an adiabatic electron affinity of ΔG = 107.5 kcal mol^{-1} for **1b** and ΔG = 111.8 kcal mol^{-1} for **2b** is obtained. These results show that **2b** is easier to reduce than **1b** leading to a more exothermic reaction for electron transfer. The thermodynamic analysis, therefore, supports our experimental finding that **2b** reacts with considerably earlier electron transfer with sulfides. For a hydride transfer reaction;

however, a two-electron transfer from substrate to oxidant takes place and therefore we also calculated the second electron affinity EA2 for the reduction of the iron(III)-oxo to iron(II)-oxo. In addition, we calculated the $BDFE2_{O–H}$ for the O−H bond strength in the iron(II)-hydroxo complexes. Both iron(II)-hydroxo species have similar $BDFE2_{O–H}$ strengths with values calculated of ΔG = 64.1 and 64.3 kcal mol^{-1} for $[Fe^{II}(OH)(L_1)]^+$ and $[Fe^{II}(OH)(L_2)]^+$, respectively. The hydride transfer energy to the iron(IV)-oxo species, however, is the sum of EA and $BDFE2_{O–H}$. Since, the EA is larger for **2b** than **1b** this will imply that also the hydride transfer energy will be more exergonic for **2b** and therefore more likely to happen. Furthermore, both the iron(IV)-oxo and iron(III)-oxo of **2b** show larger values of one-electron reduction and therefore are more susceptible for electron abstraction than their corresponding N_5 ligated complexes. These electron affinity differences give evidence of more likely early electron transfer for **2b** than for **1b**.

In order to understand the difference in the reactivity and the mechanism observed, we then attempted to evaluate the one-electron reduction potentials and the reorganization energies during electron transfer of **1b** and **2b** with a series of ferrocene derivatives. The fundamental electron transfer properties i.e. the reorganization energy and the one-electron reduction potentials of both complexes were evaluated with the help of the driving force dependence of electron transfer rate in light of the Marcus theory of electron transfer.[134,135] When ferrocene ($E°_{ox}$ = 0.37 V vs SCE) was added to **1b**, no formation of ferrocenium ion was observed clearly demonstrating that **1b** is unable to oxidize ferrocene. We then added dimethylferrocene ($E°_{ox}$ = 0.26 V vs SCE) to **1b**.[136] The electron transfer from dimethylferrocene (Me_2Fc) to **1b** can be measured from the formation of the $Me_2Fc^{+\bullet}$ cation radical with an absorption in the 647 nm region in the UV-Vis spectrum.[66] In particular, we set out to determine the one-electron transfer equilibrium constant between Me_2Fc and **1b** at various Me_2Fc concentrations

ranging from 0.10 – 2.5 mM and with [**1b**] = 0.48 mM. The equilibrium constant (K_{ET}) was determined to be 1.45 at 298 K (Scheme 2 and Supporting Information Figure S32). Subsequently, the one-electron reduction potential of **1b** was determined and found to be 0.27 V vs. SCE. This value compares well with the calculated EA_{1b} that when converted into a redox potential gives $E°_{red,1b,calc}$ = 0.30 V vs SCE.[137,138]

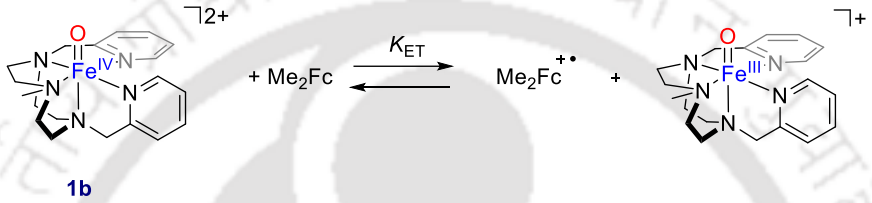

Figure. 3.9. Electron Transfer Equilibrium Between 1b and Me_2Fc.

The experiments do not record reactivity of **1b** with ferrocene (0.37 V vs. SCE), whereas **2b** is able to oxidize dibromoferrocene ($E°_{ox}$ = 0.71 V vs. SCE).[67] These results highlight the electronic and electrochemical differences in redox potential/electron affinity. We then explored electron transfer equilibria of **2b** with dibromoferrocene under the same reaction condition as that for **1b**. The electron transfer equilibrium between Br_2Fc and **2b** was measured in detail and we observe that the final concentration of $Br_2Fc^{+\bullet}$ produced in the ET reduction of **2b** increases with the increase in initial Br_2Fc concentration. This way, a value of $K_{ET,2b}$ = 4.92 was determined for the equilibrium between **2b** and Br_2Fc. Using the Nernst Equation (Eq 1), the one-electron reduction potential of **2b** is calculated to be 0.75 V vs. SCE. The experimentally determined reduction potentials of **1b** and **2b** follow the same trends as the electron affinities calculated and show that **2b** has a larger redox potential than **1b** and thus, **2b** will be more efficient in electron transfer processes. Consequently, embedding a sulfur atom into the ligand scaffold in the *cis* orientation leads to an increase of the reduction potential by 0.48 V.

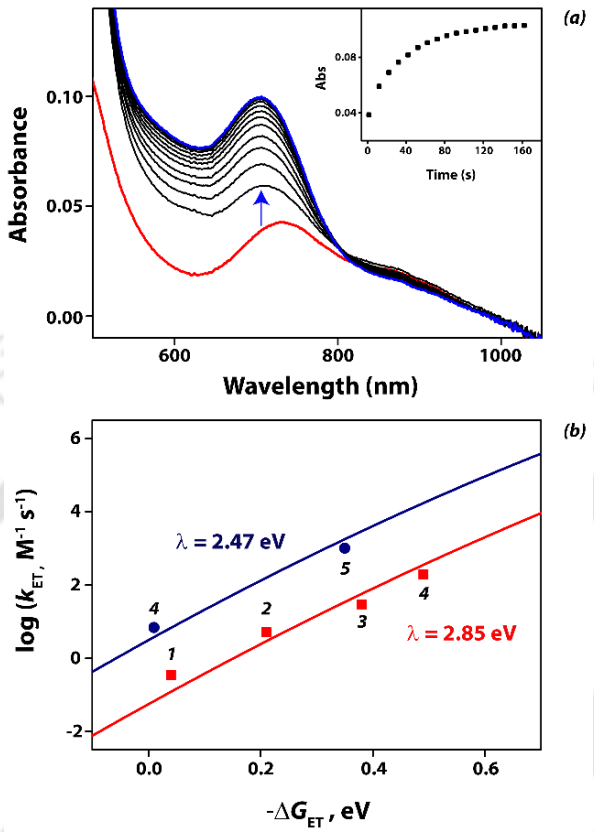

Figure. 3.10. (a) UV-vis spectral changes of **2b** (0.25 mM) upon addition of 10 equiv. of dibromoferrocene in deaerated CH_3CN at 298 K. Inset shows the formation profile of the 700 nm band. (b) Driving force dependence of rate constants (log k_{ET}) for ET from ferrocene derivatives (1, dibromoferrocene; 2, bromoferrocene; 3, ferrocene; 4, dimethylferrocene; 5, decamethylferrocene) to **1b** (blue) and **2b** (red) in deaerated CH_3CN at 298 K.

$$E°_{red} = E°_{ox} + (RT/F) \ln K_{ET} \qquad (1)$$

The electron transfer rates of both **1b** and **2b** were also examined with other ferrocene derivatives and similar reaction patterns were obtained. In general, the electron-transfer rates obeyed pseudo-first order reaction kinetics when a large excess of ferrocene derivatives was used. The pseudo-first-order rate constants (k_{obs}) increase linearly with increasing concentrations of ferrocene derivatives. The second-order rate constants (k_{ET}) were determined from the slopes of linear plots

of k_{obs} versus concentrations of ferrocene derivatives. The k_{ET} values thus obtained are listed in Table S3 (Supporting Information), together with the $E°_{ox}$ values of ferrocene derivatives, the determined $E°_{red}$ values of **1b** and **2b** and the predicted driving force for electron transfer, ($-\Delta G_{ET} = e\ (E°_{red} - E°_{ox})$ in eV with e the elementary charge). The driving force dependence of the rate constants of the ET reduction of **1b** and **2b** in acetonitrile at 298 K are shown in Figure 8b, where the log k_{ET} values are plotted against the $-\Delta G_{ET}$ values. Both curves were fitted by a linear correlation with Marcus theory dependence for adiabatic outer-sphere electron transfer as described in Eq 2.

$$k_{ET} = Z \exp [- 1/4\ (\lambda)\ (1 + \Delta G_{ET} / \lambda)^2 / k_B T] \qquad (2)$$

In Eq 2, Z is the collision frequency taken as 1×10^{11} M^{-1} s^{-1}, λ is the reorganization energy for electron transfer, k_B is the Boltzmann constant, and T is the absolute temperature.[134] Thus, the λ values were determined from the fits through the data using Eq 2 and found to be 2.47 eV and 2.85 eV for **1b** and **2b**, respectively. Consequently, the coordination of an equatorial sulfur atom to the iron(IV)-oxo ligand periphery increases the one-electron reduction potential and the reorganization energy of the iron(IV)-oxo species significantly. The higher $E°_{red}$ potential of **2b** is attained by the compensation from the higher reorganization energy including the structural changes required for electron transfer.

3.3. Conclusion

In summary, we have reported a room temperature stable equatorial sulfur ligated iron(IV)-oxo complex **2b**, and compared its structure, spectroscopic parameters and reactivity with the analogous complex with five nitrogen atoms

bound to iron (**1b**). The two structures show similar spectroscopic features and an electronic structure calculation gives the same ground state and orbital configuration. However, the introduction of a sulfur ligand in place of an N−CH_3 moiety in the parent ligand framework gives remarkably enhanced reactivity of **2b** with respect to *S*-oxidation and C−H activation reactions. We did a comparative experimental and computational study of **1b** and **2b** in OAT reaction with sulfides and hydrogen atom transfer reactions with CHD. We show that **2b** reacts with substrates with increased order of rate constants as compared to **1b**. In addition to that, **1b** and **2b** proceeds through different reaction pathway in *S*-oxidation and C−H activation reactions. It is observed that, for sulfoxidation reactions by **1b** the reaction proceeds through atom transfer via an electrophilic reaction mechanism whereas with **2b** the reaction is through an electron-transfer pathway instead. In HAT reactions, a lowering in KIE is observed which suggest that strong tunneling behavior in reaction mechanism for **1b**, whereas much lesser tunneling is seen in the case of **2b**. The differences in reactivity are shown to result from differences in chemical reaction mechanism, whereby the reaction of CHD with **1b** proceeds through two successive hydrogen atom transfer steps, while its reaction with **2b** starts with hydride transfer and is followed by rapid proton transfer. As such the electron transfer steps happen earlier with **2b** than with **1b**, thereby leading to differences in chemical reaction mechanism and lowering of the free energies of activation. To find further support of differences in electron transfer properties between **1b** and **2b** we studied their reaction with ferrocene derivatives. These studies establish that introduction of a sulfur heteroatom in the equatorial position enhances the one-electron reduction potential by 480 mV. Our work highlights the role of equatorial sulfur ligation in the reactivity nonheme iron(IV)-oxo core, which may provide a fascinating foundation for the nature's use of *cis*-sulfur ligated iron(IV)-oxo intermediate in important biological transformations.

3.4. References

1. A. G. Jarvis, *Curr. Opin. Chem. Biol*. **2020**, *58*, 63–71.
2. A. Das, C. Hessin, Y. Ren, M. Desage-El Murr, *Chem. Soc. Rev*. **2020**, *49*, 8840–8867.
3. A. C. Ghosh, C. Duboc, M. Gennari, *Coord. Chem. Rev*. **2021**, *428*, 213606.
4. H. M. Berman, J. Westbrook, Z. Feng, G. Gilliland, T. N. Bhat, H. Weissig, I. N. Shindyalov, P. E. Bourne, *Nucl. Acids Res*. **2000**, *28*, 235–242.
5. T. L. Poulos, A. H. Follmer, *Acc. Chem. Res*. **2022**, *55*, 373–380.
6. D. J. Stuehr, *Biochim. Biophys. Acta* **1999**, *1411*, 217–230.
7. C.-C. Wei, B. R. Crane, D. J. Stuehr, *Chem. Rev*. **2003**, *103*, 2365–2384.
8. J. H. Dawson, R. H. Holm, J. R. Trudell, G. Barth, R. E. Linder, E. Bunnenberg, C. Djerassi, S. C. Tang, *J. Am. Chem. Soc*. **1976**, *98*, 3707–3709.
9. T. L. Poulos, *J. Biol. Inorg. Chem*. **1996**, *1*, 356–359.
10. F. Ogliaro, S. P. de Visser, S. Shaik, *J. Inorg. Biochem*. **2002**, *91*, 554–567.
11. M. Sono, M. P. Roach, E. D. Coulter, J. H. Dawson, *Chem. Rev*. **1996**, *96*, 2841–2888.
12. *Handbook of Porphyrin Science*, (Eds.: K. M. Kadish, K. M. Smith, R. Guilard), World Scientific Publishing Co., New Jersey, **2010**.

13. *Iron-containing enzymes: Versatile catalysts of hydroxylation reaction in nature* (Eds.: S. P. de Visser, D. Kumar), RSC Publishing, Cambridge (UK), **2011**.

14. P. R. Ortiz de Montellano, *Chem. Rev*. **2010**, *110*, 932–948.

15. P. Mondal, I. Ishigami, E. F. Gérard, E. Lim, S. R. Yeh, S.P.de Visser, G.B. Wijeratne. *Chem. Sci.* **2021**, *12*, 8872-8883.

16. P. Mondal, S. Rajapakse, G. B. Wijeratne. *J. Am. Chem. Soc.* **2022**, *144*, 3843–3854.

17. B. Meunier, S. P. de Visser, S. Shaik. *Chem. Rev.* **2004**, *104*, 3947–3980.

18. I. G. Denisov, T. M. Makris, S. G. Sligar, I. Schlichting. Chem. Rev. **2005**, *105*, 2253–2278.

19. K. D. Dubey, S. Shaik. Acc. Chem. Res. **2019**, *52*, 389-399.

20. J. Rittle, M. T. Green. Science **2010**, *330*, 933–937.

21. K. L. Stone, R. K. Behan, M. T. Green, M. T. Proc. Natl. Acad. Sci. U.S.A. **2006**, *103*, 12307–12310.

22. J. E. Baldwin, M. Bradley. Chem. Rev. **1990**, *90*, 1079–1088.

23. M. Lundberg, P. E. M. Siegbahn, K. Morokuma. Biochemistry. **2008**, *47*, 1031–1042.

24. M. H. Stipanuk. Annu. Rev. Nutr. **2004**, *24*, 539–577.

25. G. D. Straganz, B. Nidetzky. ChemBioChem. **2006**, *7*, 1536–1548.

26. C. A. Joseph, M. J. Maroney. Chem. Commun. **2007**, 3338–3349.

27. M. H. Stipanuk, C. R. Simmons, P. A. Karplus, J. E. Dominy Jr. Amino Acids. **2011**, *41*, 91–102.

28. D. Buongiorno, G. D. Straganz. Coord. Chem. Rev. **2013**, *257*, 541–563.

29. S. P. de Visser. Chem. Record **2018**, *18*, 1501–1516.

30. K. V. Goncharenko, A. Vit, W. Blankenfeldt, F. P. Seebeck, F. P. Angew. Chem. Int. Ed. **2015**, *54*, 2821–2824.

31. M. Fellner, S. Aloi, E. P. Tchesnokov, S. M. Wilbanks, G. N. L. Jameson. Biochemistry **2016**, *55*, 1362–1371.

32. N. J. York, M. M. Lockart, S. Sardar, N. Khadka, W. Shi, R. E. Stenkamp, J. Zhang, P. D. Kiser, B. S. Pierce. J. Biol. Chem. **2021**, *296*, 100492.

33. E. I. Solomon, T. C. Brunold, M. I. Davis, J. N. Kemsley, S. K. Lee, N. Lehnert, F. Neese, A. J. Skulan, Y. S. Yang, J. Zhou. Chem. Rev. **2000**, *100*, 235–349.

34. T. D. H. Bugg. Chem. Biol. **2001**, *5*, 550–555.

35. P. C. A. Bruijnincx, G. van Koten, R. J. M. Klein Gebbink. Chem. Soc. Rev. **2008**, *37*, 2716–2744.

36. P. Comba, M. Kerscher. Coord. Chem. Rev. **2009**, *253*, 564–574.

37. A. R. McDonald, L. Que Jr. Coord. Chem. Rev. **2013**, *257*, 414–428.

38. W. Nam, Y. -M. Lee, S. Fukuzumi. Acc. Chem. Res. **2014**, *47*, 1146–1154.

39. K. Ray, F. F. Pfaff, B. Wang, W. Nam. J. Am. Chem. Soc. **2014**, *136*, 13942–13958.

40. S. P. de Visser, G. D. Straganz. J. Phys. Chem. A **2009**, *113*, 1835–1846.

41. X. Engelmann, I. Monte-Perez, K. Ray. Angew. Chem., Int. Ed. **2016**, *55*, 7632–7649.

42. L. Vicens, G. Olivo, M. Costas. ACS Catal. **2020**, *10*, 8611–8631.

43. T. Devi, Y. -M. Lee, W. Nam, S. Fukuzumi. Coord. Chem. Rev. **2020**, *410*, 213219.

44. J. Chen, Z. Jiang, S. Fukuzumi, W. Nam, B. Wang. Coord. Chem. Rev. **2020**, *421*, 213443.

45. G. Mukherjee, J. K. Satpathy, U. K. Bagha, M. Q. E. Mubarak, C. V. Sastri, S. P. de Visser. ACS Catal. **2021**, *11*, 9761−9797.

46. S. P. de Visser, Y. -T. Lin, H. S. Ali, U. K. Bagha, G. Mukherjee, C. V. Sastri. Coord. Chem. Rev. **2021**, *439*, 213914.

47. M. R. Bukowski, K. D. Koehntop, A. Stubna, E. L. Bominaar, J. A. Halfen, E. Münck, W. Nam, L. Que Jr. Science **2005**, *310*, 1000–1002.

48. J. E. M. N. Klein, D. Mandal, W. M. Ching, D. Mallick, L. Que, S. Shaik. J. Am. Chem. Soc. **2017**, *139*, 18705–18713.

49. Y. Jiang, L. R. Widger, G. D. Kasper, M. A. Siegler, D. P. Goldberg. J. Am. Chem. Soc. **2010**, *132*, 12214–12215.

50. A. R. McDonald, M. R. Bukowski, E. R. Farquhar, T. A. Jackson, K. D. Koehntop, M. S. Seo, R. F. De Hont, A. Stubna, J. A. Halfen, E. Munck, W. Nam, L. Que Jr. J. Am. Chem. Soc. **2010**, *132*, 17118-17129.

51. M. Sallmann, S. Kumar, P. Chernev, J. Nehrkorn, A. Schnegg, D. Kumar, H. Dau, C. Limberg, S. P. de Visser. Chem. Eur. J. **2015**, *21*, 7470–7479.

52. K. Anandababu, R. Ramasubramanian, H. Wadepohl, P. Comba, N. J. Britto, M. Jaccob, R. Mayilmurugan. Chem. Eur. J. **2019**, *25*, 9540-9547.

53. G. Villar-Acevedo, P. Lugo-Mas, M. N. Blakely, J. A. Rees, A. S. Ganas, E. M. Hanada, W. Kaminsky, J. A. Kovacs. J. Am. Chem. Soc. **2017**, *139*, 119−129.

54. A. A. Fischer, J. R. Miller, R. J. Jodts, D. M. Ekanayake, S. V. Lindeman, T. C. Brunold, A. T. Fiedler. Inorg. Chem. **2019**, *58*, 16487−16499.

55. J. B. Gordon, A. C. Vilbert, I. M. DiMucci, S. N. MacMillan, K. M. Lancaster, P. Moënne-Loccoz, D. P. Goldberg. J. Am. Chem. Soc. **2019**, *141*, 17533–17547.

56. J. Deutscher, P. Gerschel, K. Warm, U. Kuhlmann, S. Mebs, M. Haumann, H. Dau, P. Hildebrandt, U. P. Apfel, K. Ray. Chem. Commun. **2021**, *57*, 2947–2950.

57. I. Monte-Pérez, X. Engelmann, Y. -M. Lee, M. Yoo, E. Kumaran, E. R. Farquhar, E. Bill, J. England, W. Nam, M. Swart, K. Ray. Angew. Chem. Int. Ed. **2017**, *56*, 14384–14388.

58. L. Kaur, D. Mandal. Inorg. Chem. **2022**, *61*, 14582–14590.

59. Purification of laboratory chemicals (Eds.: W. L. Armarego, D. D. Perrin), Pergamon Press, Oxford, **1997**.

60. H. Saltzman. in Organic Syntheses, J. G. Sharekin. (Ed.), Vol. V, Wiley, New York, **1973**, pp. 658.

61. B. Chak, A. McAuley, T. W. Whitcombe. Can. J. Chem. **1994**, *72*, 1525-1532.

62. M. Obermeier, F. Beckmann, R. S. Schaer, O. S. Wenger, M. Schwalbe. Front. Chem. **2021**, *9*, 812.

63. D. Zhang, D. H. Busch, N. W. Alcock. Bull. Korean Chem. Soc. **1998**, *19*, 895-1018.

64. A. Company, G. Sabenya, M. Gonzalez-Bejar, L. Gomez, M. Clemancey, G. Blondin, A. J. Jasniewski, M. Puri, W. R. Browne, J. -M. Latour, L. Que Jr, M. Costas, J. Perez-Prieto, J. Lloret-Fillol. J. Am. Chem. Soc. **2014**, *136*, 4624–4633.

65. Z. Cong, H. Kinemuchi, T. Kurahashi, H. Fujii. Inorg. Chem. **2014**, *53*, 10632-10641.

66. A. Paul, R. Borrelli, H. Bouyanfif, S. Gottis, F. Sauvage. ACS Omega **2019**, *4*, 14780–14789.

67. H. Yoon, Y. Morimoto, Y.M. Lee, W. Nam, S. Fukuzumi. Chem. Commun. **2012**, *48*, 11187-11189.

68. Gaussian 09, Revision D.01, M. J. Frisch, G. W. Trucks, H. B. Schlegel, G. E. Scuseria, M. A. Robb, J. R. Cheeseman, G. Scalmani, V. Barone, B. Mennucci, G. A. Petersson, H. Nakatsuji, M. Caricato, X. Li, H. P. Hratchian, A. F. Izmaylov, J. Bloino, G. Zheng, J. L. Sonnenberg, M. Hada, M. Ehara, K. Toyota, R. Fukuda, J. Hasegawa, M. Ishida, T. Nakajima, Y. Honda, O. Kitao, H. Nakai, T. Vreven, J. A. Montgomery Jr., J. E. Peralta, F. Ogliaro, M. Bearpark, J. J. Heyd, E. Brothers, K. N. Kudin, V. N. Staroverov, R. Kobayashi, R. Normand, K. Raghavachari, A. Rendell, J. C. Burant, S. S. Iyengar, J. Tomasi, M. Cossi, N. Rega, J. M. Millam, M. Klene, J. E. Knox, J. B. Cross, V. Bakken, C. Adamo, J. Jaramillo, R. Gomperts, R. E. Stratmann, O. Yazyev, A. J. Austin, R. Cammi, C. Pomelli,

J. W. Ochterski, R. L. Martin, K. Morokuma, V. G. Zakrzewski, G. A. Voth, P. Salvador, J. J. Dannenberg, S. Dapprich, A. D. Daniels, O, Farkas, J. B. Foresman, J. V. Ortiz, J. Cioslowski, D. J. Fox. Gaussian, Inc., C. T. Wallingford, **2009**.

69. J. Tomasi, B. Mennucci, R. Cammi. Chem. Rev. **2005**, *105*, 2999-3094.

70. A. D. Becke. J. Chem. Phys. **1993**, *98*, 5648–5652.

71. C. Lee, W. Yang, R. G. Parr. Phys. Rev. B **1988**, *37*, 785–789.

72. P. J. Hay, W. R. Wadt. J. Chem. Phys. **1985**, *82*, 270–283.

73. M. M. Francl, W. J. Pietro, W. J. Hehre, J. S. Binkley, M. S. Gordon, D. J. DeFrees, J. A. Pople. J. Chem. Phys. **1982**, *77*, 3654–3658.

74. H. S. Ali, S. P. de Visser. Chem. Eur. J. **2022**, *28*, e202104167.

75. T. Mokkawes, S. P. de Visser. Chem. Eur. J. **2023**, *29*, e202203875.

76. G. Mukherjee, A. Alili, P. Barman, D. Kumar, C. V. Sastri, S. P. de Visser. Chem. Eur. J. **2019**, *25*, 5086–5098.

77. U. K. Bagha, R. Yadav, T. Mokkawes, J. K. Satpathy, D. Kumar, C. V. Sastri, S. P. de Visser. Chem. Eur. J. **2023**, *29*, e202300478.

78. Y. Goto, T. Matsui, S. -I. Ozaki, Y. Watanabe, S. Fukuzumi. J. Am. Chem. Soc. **1999**, *121*, 9497–9502.

79. C. V. Sastri, J. Lee, K. Oh, Y. J. Lee, J. Lee, T. A. Jackson, K. Ray, H. Hirao, W. Shin, J. A. Halfen, J. Kim, L. Que, Jr, S. Shaik, W. Nam. Proc. Natl. Acad. Sci. USA **2007**, *104*, 19181–19186.

80. J. Park, J. Morimoto, Y. -M. Lee, W. Nam, S. Fukuzumi. J. Am. Chem. Soc. **2011**, *133*, 5236–5239.

81. A. K. Vardhaman, P. Barman, S. Kumar, C. V. Sastri, D. Kumar, S. P. de Visser. Angew. Chem. Int. Ed. **2013**, *52*, 12288–12292.

82. H. C. Brown, Y. Okamoto. J. Am. Chem. Soc. **1958**, *80*, 4979–4987.

83. C. Hansch, A. Leo, R. W. Taft. Chem. Rev. **1991**, *91*, 165-195.

84. W. Washeed, A. Draksharapu, S. Banerjee, V. G. Young Jr., R. Fan, Y. Guo, M. Ozerov, J. Nehrkorn, J. Krzystek, J. Telser, L. Que Jr. Angew. Chem. Int. Ed. **2018**, *130*, 9531–9535.

85. G. Mukherjee, C. W. Z. Lee, S. S. Nag, F. G. Cantú Reinhard, D. Kumar, C. V. Sastri, S. P. de Visser. Dalton Trans. **2018**, *47*, 14945–14957.

86. J. M. Mayer. Acc. Chem. Res. **1998**, *31*, 441–450.

87. J. Yoon, S. A. Wilson, Y. K. Jang, M. S. Seo, K. Nehru, B. Hedman, K. O. Hodgson, E. Bill, E. I. Solomon, W. Nam. Angew. Chem., Int. Ed. **2009**, *121*, 1283–1286.

88. D. E. Lansky, D. P. Goldberg. Inorg. Chem. **2006**, *45*, 5119–5125.

89. J. J. Warren, T. A. Tronic, J. M. Mayer. Chem. Rev. **2010**, *110*, 6961–7001.

90. S. N. Dhuri, Y. -M. Lee, M. S. Seo, J. Cho, D. D. Narulkar, S. Fukuzumi, W. Nam. Dalton Trans. **2015**, *44*, 7634-7642.

91. R. A. Baglia, J. P. T. Zaragoza, D. P. Goldberg. Chem. Rev. **2017**, *117*, 13320–13352.

92. D. Mandal, S. Shaik. J. Am. Chem. Soc. **2016**, *138*, 2094–2097.

93. D. Mandal, D. Mallick, S. Shaik. Acc. Chem. Res. **2018**, *51*, 107–117.

94. E. J. Klinker, S. Shaik, H. Hirao, L. Que Jr. Angew. Chem., Int. Ed. **2009**, *48*, 1291–1295.

95. J. C. Price, E. W. Barr, T. E. Glass, C. Krebs, J. M. Bollinger Jr. J. Am. Chem. Soc. **2003**, *125*, 13008–13009.

96. L. M. Hoffart, E. W. Barr, R. B. Guyer, J. M. Bollinger Jr, C. Krebs. Proc. Natl. Acad. Sci. U.S.A. **2006**, *103*, 14738–14743.

97. S. Kumar, A. S. Faponle, P. Barman, A. K. Vardhaman, C. V. Sastri, D. Kumar, S. P. de Visser. J. Am. Chem. Soc. **2014**, *136*, 17102–17115.

98. A. K. Vardhaman, Y. -M. Lee, J. Jung, K. Ohkubo, W. Nam, S. Fukuzumi. Angew. Chem. Int. Ed. **2016,** *55*, 3709–3713.

99. G. Mukherjee, F. G. Cantú Reinhard, U. K. Bagha, C. V. Sastri, S. P. de Visser. Dalton Trans. **2020**, *49*, 5921–5931.

100. J. -U. Rohde, J. -H. In, M. H. Lim, W. W. Brennessel, M. R. Bukowski, A. Stubna, E. Münck, W. Nam, L. Que Jr. Science **2003**, *299*, 1037–1039.

101. P. J. Riggs-Gelasco, J. C. Price, R. B. Guyer, J. H. Brehm, E. W. Barr, J. M. Bollinger Jr., C. Krebs. J. Am. Chem. Soc. **2004**, *126*, 8108–8109.

102. C. Krebs, D. G. Fujimori, C. T. Walsh, J. M. Bollinger Jr. Acc. Chem. Res. **2007**, *40*, 484–492.

103. D. Kumar, H. Hirao, L. Que Jr, S. Shaik. J. Am. Chem. Soc. **2005**, *22*, 8026–8027.

104. A. Company, L. Gómez, M. Güell, X. Ribas, J. M. Luis, L. Que, M. Costas. J. Am. Chem. Soc. **2007**, *129*, 15766–15767.

105. S. P. de Visser. Angew. Chem. Int. Ed. **2006**, *45*, 1790–1793.

106. L. Bernasconi, E. -J. Baerends. Eur. J. Inorg. Chem. **2008**, *2008*, 1672–1681.

107. A. Dey. J. Am. Chem. Soc. **2010**, *132*, 13892–13901.

108. E. Andris, R. Navrátil, J. Jašík, T. Terencio, M. Srnec, M. Costas, J. Roithová. J. Am. Chem. Soc. **2017**, *139*, 2757– 2765.

109. S. F. Ye, F. Neese. Proc. Natl. Acad. Sci. USA **2011**, *108*, 1228–1233.

110. A. Ansari, A. Kaushik, G. Rajaraman. J. Am. Chem. Soc. **2013**, *135*, 4235–4249.

111. Y. Cao, J. A. Valdez-Moreira, S. Hay, J. M. Smith, S. P. de Visser. Chem. Eur. J. **2023**, *29*, e202300271.

112. E. Andris, J. Jašík, L. Gómez, M. Costas, J. Roithová. Angew. Chem., Int. Ed. **2016**, *55*, 3518-3518.

113. V. Dantignana, M. C. Perez-Segura, P. Besalu-Sala, E. Delgado-Pinar, A. Martinez-Camarena, J. Serrano-Plana, A. Alvarez-Nunez, C. E. Castillo, E. Garcia-Espana, J. M. Luis, M. G. Basallote, M. Costas, A. Company. Angew. Chem., Int. Ed. **2023**, *62*. e202211361.

114. S. Stepanović, L. Andjelković, M. Zlatar, K. Andjelković, M. Gruden-Pavlović, M. Swart. Inorg. Chem. **2013**, *52*, 13415–13423.

115. P. Barman, A. S. Faponle, A. K. Vardhaman, D. Angelone, A. -M. Löhr, W. R. Browne, P. Comba, C. V. Sastri, S. P. de Visser. Inorg. Chem. **2016**, *55*, 10170–10181.

116. K. Cheaib, M. Q. E. Mubarak, K. Sénéchal-David, C. Herrero, R. Guillot, M. Clémancey, J. -M. Latour, S. P. de Visser, J. -P. Mahy, F. Banse, F. Avenier. Angew. Chem. Int. Ed. **2019**, *58*, 854–858.

117. D. Kumar, S. P. de Visser, P. K. Sharma, H. Hirao, S. Shaik. Biochemistry **2005**, *44*, 8148–8158.

118. H. Hirao, L. Que Jr, W. Nam, S. A. Shaik. Chem. Eur. J. **2008**, *14*, 1740–1756.

119. D. Kumar, G. N. Sastry, S. P. de Visser. Chem. Eur. J. **2011**, *17*, 6196–6205.

120. R. Kumar, B. Pandey, A. Singh, G. Rajaraman. Inorg. Chem. **2021**, *60*, 12085–12099.

121. S. Shaik, Y. Wang, H. Chen, J. Song, R. Meir. Faraday Discuss. **2010**, *145*, 49–70.

122. D. Kumar, L. Tahsini, S. P. de Visser, H. Y. Kang, S. J. Kim, W. Nam. J. Phys. Chem. A **2009**, *113*, 11713–11722.

123. R. Latifi, M. A. Sainna, E. V. Rybak-Akimova, S. P. de Visser. Chem. Eur. J. **2013**, *19*, 4058–4068.

124. D. Usharani, D. Lacy, A. S. Borovik, S. Shaik. J. Am. Chem. Soc. **2013**, *135*, 17090-17104.

125. M. K. Goetz, J. S. Anderson. J. Am. Chem. Soc. **2019**, *141*, 4051−4062.

126. S. Fukuzumi, H. Kotani, Y. -M. Lee, W. Nam. J. Am. Chem. Soc. **2008**, *130*, 15134–15142.

127. P. Comba, S. Fukuzumi, H. Kotani, S. Wunderlich. Angew. Chem. Int. Ed. **2010**, *49*, 2622–2625.

128. A. C. McQuilken, Y. Jiang, M. A. Siegler, D. P. Goldberg. J. Am. Chem. Soc. **2012**, *134*, 8758−8761.

129. D. Kumar, W. Thiel, S. P. de Visser. J. Am. Chem. Soc. **2011**, *133*, 3869–3882.

130. D. Kumar, G. N. Sastry, D. P. Goldberg, S. P. de Visser. J. Phys. Chem. A **2012**, *116*, 582–591.

131. A. S. Faponle, F. P. Seebeck, S. P. de Visser. J. Am. Chem. Soc. **2017**, *139*, 9259–9270.

132. C. -C. G. Yeh, C. Pierides, G. N. L. Jameson, S. P. de Visser. Chem. Eur. J. **2021**, *27*, 13793–13806.

133. S. P. de Visser. J. Am. Chem. Soc. **2010**, *132*, 1087–1097.

134. R. A. Marcus. Annu. Rev. Phys. Chem. **1964**, *15*, 155–196.

135. R. A. Marcus. Angew. Chem. Int. Ed. Engl. **1993**, *32*, 1111–1121.

136. S. Fukuzumi, K. Okamoto, C. P. Gros, R. J. Guilard. J. Am. Chem. Soc. **2004**, *126*, 10441–10449.

137. P. Comba, D. Faltermeier, B. MartinZ. Anorg. Allg. Chem. **2020**, *646*, 1839–1845.

138. V. A. Dixit, J. Warwicker, S. P. de Visser. Chem. Eur. J. **2020**, *26*, 15270–15281.

CHAPTER-IV

Exploring a Sulfur Ligated Iron(IV)-Tosylimido species: A Comparative Study with its Oxo-Analogue

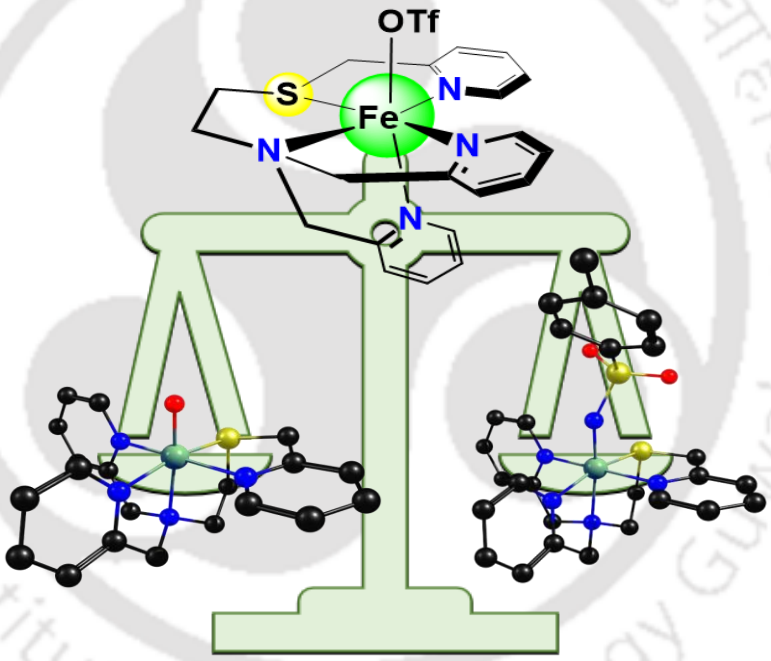

To be submitted

4.1 Introduction

Iron(IV)-oxo complexes, both heme and non-heme, are important catalytic intermediates in enzymes that enable vital biotransformation for human health. These include detoxification processes in the liver and the biosynthesis of hormones.[1-11] A catalytically active iron(IV)-oxo species is produced when monooxygenases and dioxygenases interact with molecular oxygen at an iron centre, transferring an oxygen atom to the substrate. Iron(IV)-imido and Iron(V)-nitrido complexes can be synthesized by utilizing a nitrogen donor. Even though these complexes are rare, there is evidence that cytochrome P450 enzymes catalyze substrate aziridination, presumably through a high-valent iron(IV)-nitrido or iron(IV)-imido complex.[12-14] Numerous nitrene or imido ligand-based iron-porphyrin model systems have been investigated, exhibiting reactivity towards effective olefin aziridination.[15-19]

There are only quite a few literature studies are available on the iron(V)-nitrido species ($Fe^{V}\equiv N$) and iron(IV)-imido ($Fe^{IV}=NR$) species, in comparison to iron(IV)-oxo complexes, which have been the subject of substantial research over the years. These high-valent metal-nitrido/imido complexes are believed to be able to catalyze isolobal amination processes due to their strong oxidative capability. Several groups have researched the chemistry of metal-catalyzed aminidation of aliphatic C-H bonds and aziridination of alkenes utilizing iminoiodane reagents over the past ten years.[20-27] Understanding the basic chemical characteristics of the hypothesised metal-nitrogen multiple bound species has advanced significantly in recent years thanks to their isolation and spectroscopic characterization.[20-24,28-35] However, little is known about its relative reactivity to the well-known iron(IV)-oxo species, and there is no information on its potential as a nitrogen atom transfer agent.[35]

Previously, a comparative study between iron(IV)-oxo and iron(IV)-imido oxidants were performed using the pentadentate N4Py ligand (N,N-bis(2-pyridylmethyl)-N-bis(2-pyridyl)methylamine) as the basic ligand skeleton.[36-38] This ligand was the first example that can support both the high valent iron(IV)-oxo and -imido species. Here it was reported that both iron(IV)-oxo and iron(IV)-imido oxidants reacts with substrates via different reaction pathway. For e.g. iron(IV)-oxo reacts with thioanisole via direct oxygen atom transfer, where as iron(IV)-imido goes via electron transfer. Also, there was a report of two octahedral iron(IV)-imido complexes with $MePy_2TACN$ and $Me_2(CHPy_2)TACN$ ligand frameworks by Costas etal ($MePy_2TACN$ = N-methyl-N,N-bis(2-picolyl)-1,4,7-triazacyclononane, and $Me_2(CHPy_2)TACN$ = 1-(di(2-pyridyl)methyl)-4,7-dimethyl-1,4,7- triazacyclononane.[39] Also, our group have extensively studied the comparative reactivity of iron(IV)-oxo and iron(IV)-imido complexes with BnTPeN ligand framework (BnTPeN = N-Benzyl-N,N,N-tris(pyridine-2-ylmethyl)ethane-1,2-diamine).[40] This chapter discusses in depth the reactivity of $[Fe^{IV}(NTs)(STPeN)]^{2+}$ (**6c**) and $[Fe^{IV}(O)(STPeN)]^{2+}$ (**6b**) towards S-oxidation and C-H activation. Attempts have been made to gain insights to the similarities and differences in the reaction pathway of the two intermediates.

4.2 Experimental Section

High-valent iron intermediates iron(IV)-oxo intermediate and iron(IV)-imido were generated in-situ from 1mM solution of the respective iron(II) complexes. The iron(IV)-oxo complex **6b** was prepared using 1.5 equiv. of soluble iodosylbenzene (^{S}PhIO) as an oxidant in acetonitrile solution at 298 K. The iron(IV)-imido complex **6c** was generated in an acetonitrile solution *in situ* using 1.5 equiv. of ^{S}PhINTs in dichloromethane as tosylimido donor using procedures reported before. The oxidation reactions of thioanisole and C-H bonds

were followed by monitoring the change in absorption spectrum of the intermediates using UV-vis. spectroscopy. The second order rate constants were determined by varying the concentration of thioanisole, and its derivatives, Xanthene, 9,10-Dihydroanthracene (DHA), 1,4-Cyclohexadiene (CHD), fluorene and triphenylmethane for **6b** and **6c**.

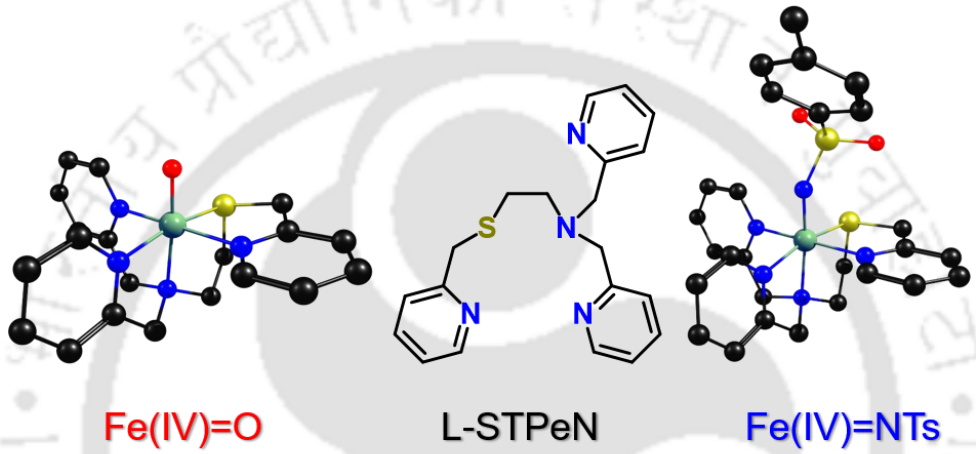

Figure. 4.1. Ligands and oxidants employed in this study.

4.3 Results and discussions

Ligands L5 and L6, with L5 = N^1-benzyl-N^1, N^2, N^2-tris(pyridine-2-ylmethyl) ethane-1,2-diamine and L6 = 2-(2-Pyridinyl)methylthio-N,N-bis[(2-pyridinyl)methyl]ethanamine were synthesized and characterized (Figures 2.4-2.9, Chapter II) according to reported procedures. Subsequently, the L5 and L6 ligands were reacted with $[Fe^{II}(CH_3CN)_2(OTf)_2]$ with OTf = triflate in acetonitrile under inert atmosphere inside the glovebox to form the corresponding iron(II) complexes: $[Fe^{II}(L5)(CH_3CN)](OTf)_2$ (**5a**) and $[Fe^{II}(L6)(CH_3CN)](OTf)_2$ (**6a**).[63,64] These iron(II) complexes were characterized with UV-vis absorption spectroscopy, cyclic voltametry (CV), electrospray ionization mass spectrometry (ESI-MS) and X-Ray crystallography, see Figures 2.15, 2.16, 2.21, 2.25 & 2.28

in the chapter II. Our obtained characterization matches previous work of these iron(II)

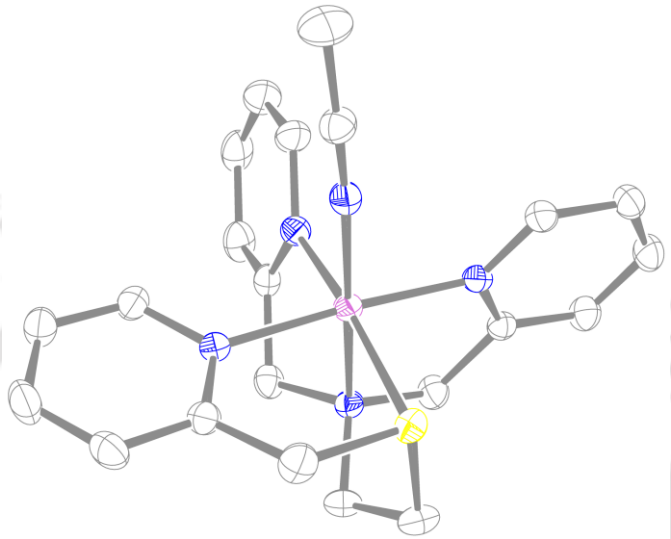

Figure. 4.2. ORTEP plot of $[Fe^{II}(STPen)(CH_3CN)](OTf)_2$ with thermal ellipsoid drawn at 30 % probability level. Counter-ions and hydrogens have been omitted for better clarity.

complexes with BnTPen ligand framework.[40] The UV-vis spectrum of both iron(II) complexes shows a ligand to metal charge-transfer band with a notable shift in the molar extinction coefficient (ε) and λ_{max} values. In particular, for **5a** we obtained an ε_{5a} = 8046 M^{-1} cm^{-1} ($\lambda_{max,5a}$ = 386 nm), whereas the corresponding values for complex **6a** are ε_{6a} = 8469 M^{-1} cm^{-1} ($\lambda_{max,6a}$ = 372 nm). As such, a hypsochromic shift (by 14 nm) with increased molar absorption coefficient is obtained through insertion of a sulfur atom in the equatorial plane of the complex (Chapter II, Figure 2.28). Moreover, cyclic voltammetry studies of the iron(II) complexes **5a** and **6a** exhibited a reversible/quasi-reversible Fe^{II}/Fe^{III} couple with a difference of 140 mV in their redox potentials, namely values of $E_{1/2}$ = 870 mV for **5a** and $E_{1/2}$ = 1010 mV for **6a** (Chapter II, Figure 2.21). Also, the single crystal structure of 6a illustrates this geometry to be pseudooctahedral, where there are six coordination sites with the Fe center.

where, the sulphur atom is found to be in an equatorial position and an acetonitrile molecule is bound to the iron centre. The three pyridine rings are in the equatorial plane, whereas another tethering N atom is axially bound to iron. The complexes gave ESI-MS peaks at *m/z* = 628.06 and 555.04 corresponding to $[Fe^{II}(L5)CF_3SO_3]^+$ and $[Fe^{II}(L6)CF_3SO_3]^+$ fragment ion respectively (Figure 2.15 & 2.16). The isotropic distribution pattern for the complexes confirms their assignments.

Table 4.1. Selected bond lengths [Å] and bond angles [°] for $[Fe^{II}(STPeN)(CH_3CN)](OTf)_2$ (6a)

Bonds	Bond-lengths (Å)
Fe1 _ N1	1.980
Fe1 _ N2	2.025
Fe1 _ N3	2.010
Fe1 _ N4	1.956
Fe1 _ N5	1.929
Fe1 _ S1	2.261
Avg Fe _ N	1.980

***cis*-equatorial bond angles (°)**		***cis*-bond angle of equatorial Fe1-S with $N_{ax/eq}$ (°)**	
∠ N1-Fe1-N4	90.05(2)	∠ N3-Fe1-S1	85.50 (2)
∠ N1-Fe1-N3	94.34(2)	∠ N4-Fe1-S1	89.90(2)
∠ N2-Fe1-N4	84.18(2)	∠ N2-Fe1-S1	88.44(2)
∠ S1-Fe1-N3	85.50(2)	∠ N5-Fe1-S1	96.94(2)
***trans*-equatorial bond angles (°)**		***cis*-bond angle of equatorial Fe1-N/ Fe1-S with N2 (°)**	
∠ N3-Fe1-N4	175.38(2)	∠ N1-Fe1-N2	80.84(2)
∠ S1-Fe1-N1	169.23(2)	∠ N4-Fe1-N2	84.18(2)
-	-	∠ N3-Fe1-N2	95.11(2)
-	-	∠ S1-Fe1-N2	88.44(2)

Fe^{IV}=O and Fe^{IV}=NTs complexes of L5 ligand framework is well known in the literature.[40] Treatment of $[Fe^{II}(L6)(CH_3CN)](OTf)_2$ with 1.5 equivalents of ^{s}PhIO & ^{s}PhINTs in CH_3CN under ambient conditions generated the corresponding iron(IV)-oxo complex $[Fe^{IV}(O)(L6)]^{2+}$, **6b** (λ_{max} = 756 nm, ε = 380 $M^{-1}cm^{-1}$, $t_{1/2}$ = 60 mins. at RT) and $[Fe^{IV}(NTs)(STPeN)]^{2+}$, **6c** ($\lambda_{max}$ = 730 nm, ε = 250 $M^{-1}cm^{-1}$, $t_{1/2}$ = 45 mins. at RT). Thus, the substitution of the N-benzyl

moiety in L5 with the sulfur atom to form L6 resulted in a red shift of the d-d transition band by 20 nm for the Fe(IV)=O complex. These ferryl-oxo and ferryl-nitrene complexes were characterized by UV-vis and ESI-MS spectrometry and resonance raman spectroscopy.

The ESI-MS spectrum of **6b** shows prominent peaks at m/z 571.03 and m/z 211.04 corresponding to the $[Fe^{IV}(O)(L_6)(OTf)]^+$ and $[Fe^{IV}(O)(L_6)]^{2+}$ ions, respectively (Figure. 4.3a). The isotopic distribution patterns for the two species confirm their assignments. The formation of the $[Fe^{IV}(O)(L_2)(OTf)]^+$ species was further established by an isotopic labeling experiment using $H_2{}^{18}O$, which leads to oxygen atom exchange with the oxo group. The experiment with $H_2{}^{18}O$ moves the peak in the ESI-MS spectrum for $[Fe^{IV}(O)(L_2)(OTf)]^+$ from m/z 549.14 to m/z 551.14, while the peak representing the $[Fe^{IV}(O)(L_2)]^{2+}$ ion shifts by one unit. Hence the isotopic labelling experiment confirms that one oxygen atom is incorporated into the metal complex in the form of an iron(IV)-oxo species. Similarly, The ESI-MS spectrum of **6c** shows prominent peaks at m/z 724.06 and m/z 287.50 corresponding to the $[Fe^{IV}(NTs)(L_6)(OTf)]^+$ and $[Fe^{IV}(NTs)(L_6)]^{2+}$ ions, respectively (Figure. 4.3b). The isotopic distribution patterns for the two species confirm their assignments. The resonance Raman spectra of **6c** obtained at 571 nm excitation wavelength features a resonantly enhanced bands at 975 cm^{-1}, that was not there in the starting Fe(II) complex as well as in the spectra for the solvent. In analogy with the previously reported Fe^{IV}=NTs complexes,[41] we have assigned this band as having originated from the Fe=N (975 cm^{-1}) stretch, see Figure. 4.3. We couldn't able to get the resonance Raman spectra for complex **6b**, due to the conversion of Fe^{IV}=O to Fe^{II} upon laser excitation.

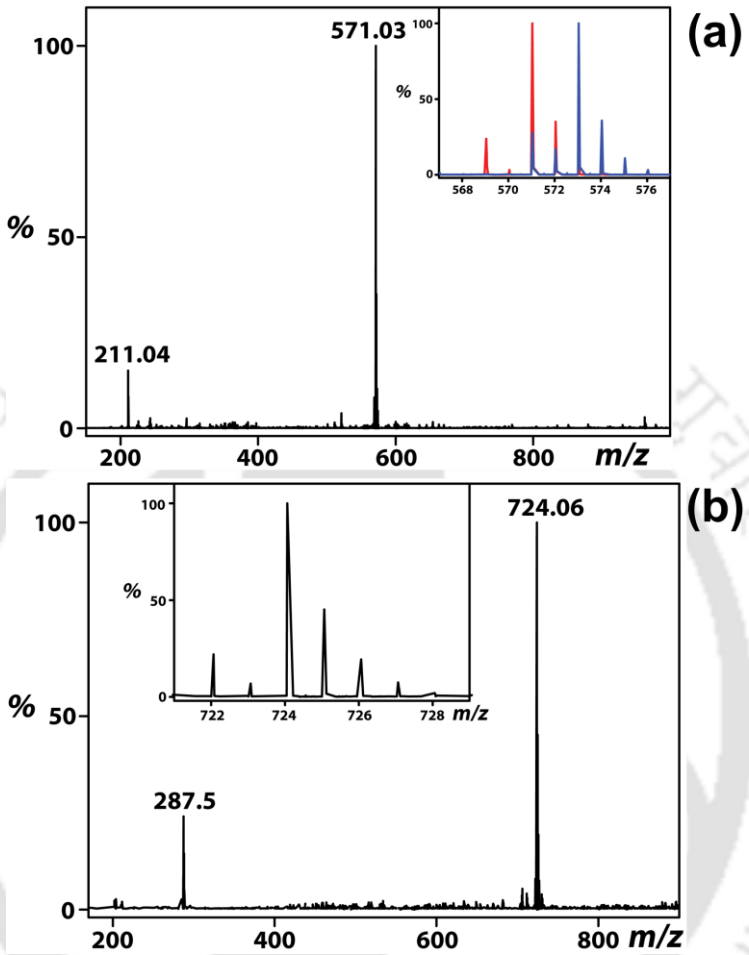

Figure. 4.3. (a) Electrospray ionization mass spectra of 6b in CH_3CN at 298 K. The inset shows expanded isotopic distribution patterns of $[Fe^{IV}(^{16}O)(L_6)(OTf)]^+$ (in red) and $[Fe^{IV}(^{18}O)(L_6)(OTf)]^+$ (in blue). (b) Electrospray ionization mass spectra of 6c in CH_3CN at 298 K. The inset shows expanded isotopic distribution patterns of $[Fe^{IV}(NTs)(L_6)(OTf)]^+$.

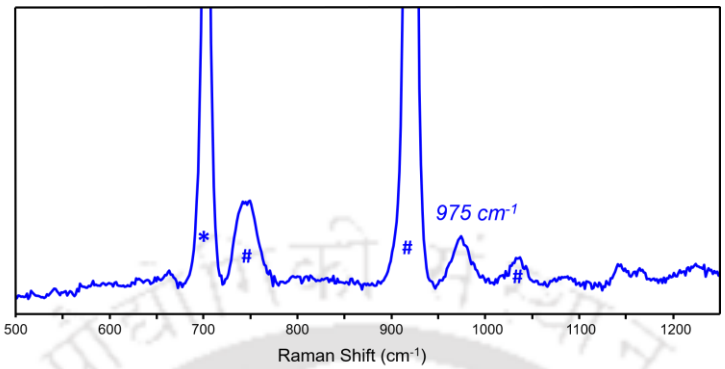

Figure. 4.4. Resonance Raman spectra of 6c at 298 K at 571 nm excitation wavelength. * indicates for the solvent peaks.

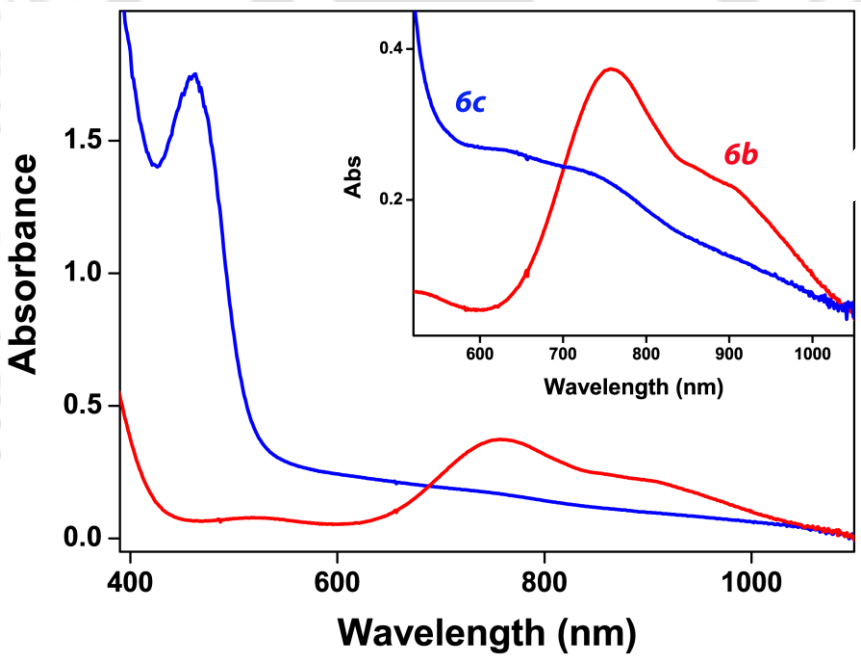

Figure. 4.5. UV-vis spectra of 6b (red) and 6c (blue) in CH_3CN at 298 K.

The addition of thioanisole to **6b** at 263 K led to the decay of the iron(IV)-oxo characteristic band at 756 nm in the UV-vis spectrum (Fig. 4.6a), thereby producing methyl phenyl sulfoxide as the major product. We measured

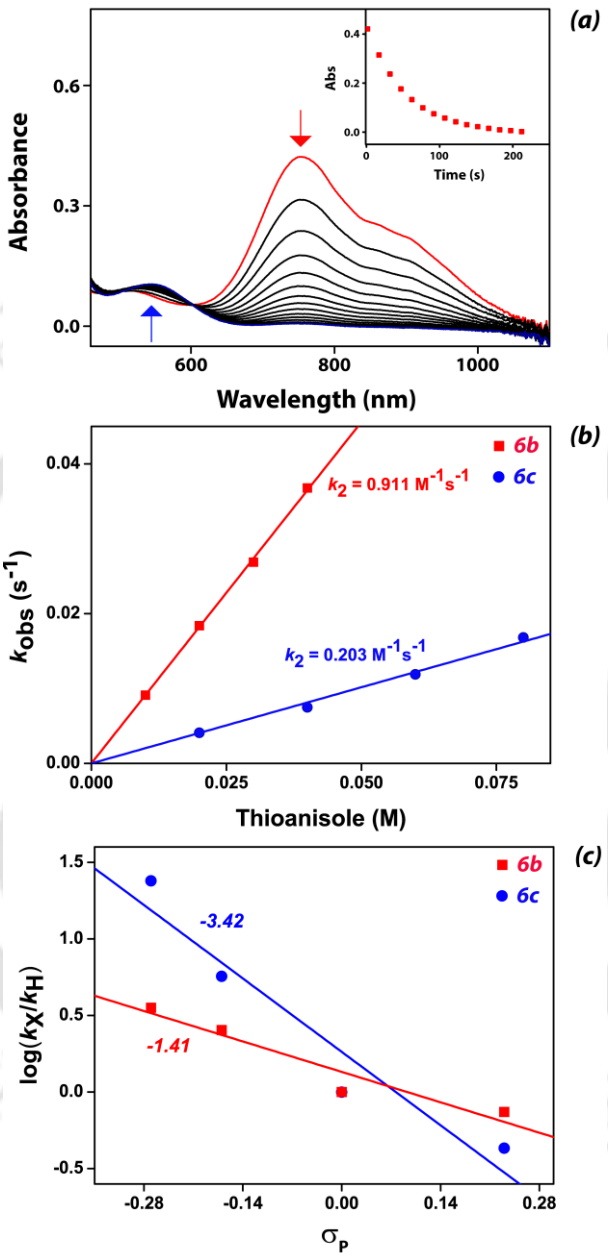

Figure. 4.6. (a) UV-vis spectral changes of 6b upon addition of 20 equiv. of thioanisole in CH_3CN at 263 K. Inset shows the decay profile of the 756 nm band. (b) The second-order rate constant determined for the reaction of 6b (Red) (1 mM) and 6c (Blue) (1 mM) with thioanisole at 263 K. (c) plot of $\log(k_X/k_H)$ against one-electron oxidation potentials (E^0_{ox}) of *p*-X-thioanisole in their reaction with 6b and 6c at 263 K in CH_3CN, where k_X and k_H are the pseudo first-order rate constants of *p*-X-thioanisole and thioanisole, respectively.

the change in absorbance from the UV-vis spectra at 756 nm and plotted it as a function of time, which enabled us to determine the pseudo-first-order rate constant (k_{obs}) for the reaction. Then, these observed rate constants were converted into second-order rate constants by plotting k_{obs} as a function of substrate concentration. The second-order rate constant (k_2) for the reaction of thioanisole with **6b** was evaluated to be 0.911 $M^{-1}s^{-1}$ at 263 K. Subsequently, the reaction of thioanisole with **6c** under the same reaction conditions provided a second-order rate constant of 0.203 $M^{-1}s^{-1}$. Thus, under the same experimental conditions, the reactivity of **6b** with thioanisole is faster than that of **6c** by a factor of almost *four-times* (Fig. 3c).

To gain insight into the mechanistic details of the reaction pathway, we studied the reaction of **6b** and **6c** with various para-*X*-substituted thioanisole substrates (X = OCH_3, CH_3, H, Cl) and measured their reaction rates (Fig. 4.2).[42-47] It had been widely studied that a significant larger slope indicative of an electron transfer pathway, whereas a smaller Hammett slope indicates an oxygen atom transfer pathway. A plot of the logarithm of the rate constant ratio (k_X/k_H) as a function of σ_p values of various para-*X*-substituted thioanisole substrates gives a linear correlation with a slope of ρ = –1.41 and ρ= -3.42 for **6b** and **6c** respectively. The larger Hammett slope is due to the additional stabilization of positive charge in the transition state by electron donating groups in the *para*-position of thioanisole and thus enhanced the overall rate of oxidation. similarly, when plotted against the E^0_{ox} values for various para-*X*-substituted thioanisole produces a linear correlation with a slope of -2.88 and -7.12 for **6b** and **6c** respectively. From the Hammett plot, it indicates that thioanisole reacts with **6b** and **6c** through different reaction mechanisms. It is observed that **6b** undergoes

an atom transfer through an electrophilic reaction mechanism whereas **6c** proceeds through an electron-transfer pathway.[37-38]

Table. 4.2. Hammett parameters and second-order rate constants (k_2) determined in the reaction of 6b & 6c (1 mM solution in CH_3CN) with various para-substituted thioanisole substrates in CH_3CN at 283 K.[a]

p-X	σ_p [b]	σ_p^+ [b]	E^0_{ox} [c]	*Complex*	k_2 (M^{-1} s^{-1}) x 10^{-2}	k_x/k_H [d]	log (k_x/k_H)
-OMe	–0.27	-0.78	1.13	**6b**	3.240	3.55	0.55
				6c	4.868	23.98	1.38
-Me	–0.17	-0.31	1.24	**6b**	2.318	2.54	0.40
				6c	1.157	5.69	0.75
-H	0.00	0.00	1.34	**6b**	0.911	1.0	0.00
				6c	0.203	1.0	0.00
-Cl	0.23	0.11	1.37	**6b**	0.675	0.74	–0.13
				6c	0.087	0.42	-0.37

[a] All the reactions were followed by monitoring the UV/Vis spectral changes of the reaction solution. [b] Data taken from: H. C. Brown and Y. Okamoto, *J. Am. Chem. Soc.*, 1958, 80, 4979. [c] Relative rate constant obtained by dividing the k_2 of *p*-X-thioanisole by k_2 of *p*-H-thioanisole.

Table. 4.3. Pseudo first-order rate constants determined for the reaction of 6b & 6c (1 mM) with ethylbenzene & ethylbenzene-D7 in CH_3CN at RT.

Concentration (mM)	Complex	k_{obs} x 10^{-2} for Ethylbenzene	k_{obs} x 10^{-2} for [D7]-Ethylbenzene
50	**6b**	0.61	0.042
	6c	0.49	0.0122
100	**6b**	1.40	0.089
	6c	1.01	0.0248
150	**6b**	1.96	0.136
	6c	1.52	0.0358
200	**6b**	2.61	0.176
	6c	2.11	0.0458

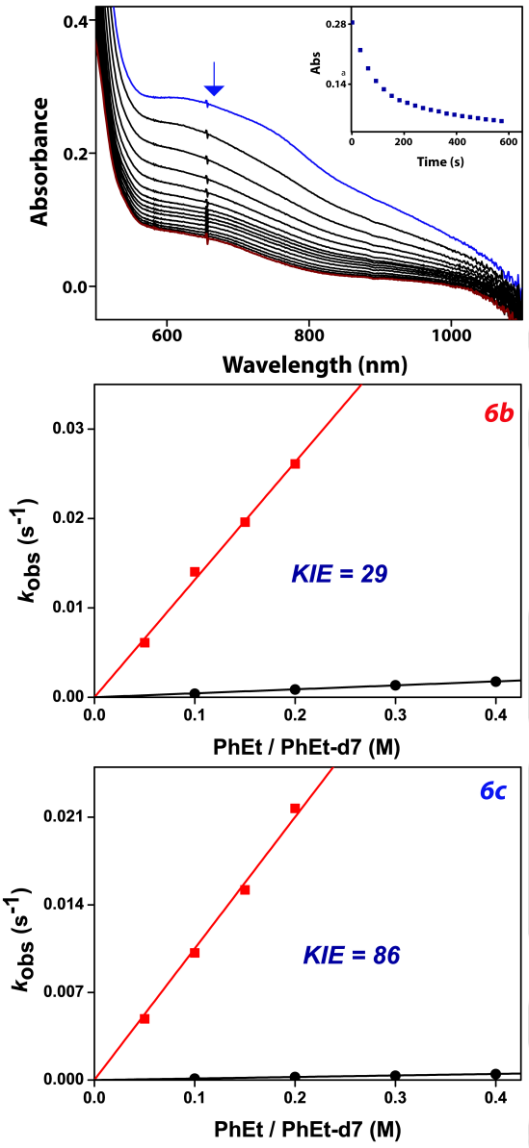

Figure. 4.7. (a) UV-vis spectral changes of 6c upon addition of 100 equiv. of ethylbenzene in CH_3CN at 298 K. Inset shows the decay profile of the 730 nm band. (b) Plots of the pseudo-first order rate constants k_{obs} vs. the substrate concentrations for ethylbenzene and d7- ethylbenzene in order to determine the kinetic isotopic effect (KIE) for the reaction of 6b with ethylbenzene in CH_3CN at 298 K. (c) Plots of the pseudo-first order rate constants k_{obs} vs. the substrate concentrations for ethylbenzene and d7- ethylbenzene in order to determine the kinetic isotopic effect (KIE) for the reaction of 6c with ethylbenzene in CH_3CN at 298 K.

We then studied the hydrogen atom abstraction ability of **6b** and **6c** with a selection of substrates with known C–H bond strengths. Earlier studies have demonstrated that reactions involving rate-determining hydrogen atom abstraction exhibits a linear relationship between the natural logarithm of the rate constant and the C–H bond dissociation energy ($BDE_{C–H}$). We investigated the hydrogen atom abstraction reactions of **6b** & **6c** with substrates including Triphenylmethane, Cumene, ethylbenzene and Toluene. These substrates span a range of C–H bond dissociation energies ($BDE_{C–H}$) typical for hydrogen atom abstraction reaction rates. A linear correlation between the natural logarithm of the rate constant versus $BDE_{C–H}$ is found for the reactions of **1a**/**2a** with substrates including Triphenylmethane, Cumene, ethylbenzene and Toluene. These substrates span a range of C–H bond dissociation energies (BDEC–H) typical for hydrogen atom abstraction reaction rates. The linearity of the Bell-Evans-Polanyi plot (log k_2' versus $BDE_{C–H}$) provides evidence of a rate-determining hydrogen atom abstraction reaction. So, the introduction of the equatorial sulfur ligands also exhibits a significant effect on the reactivity of the oxoiron (IV) and tosylimidoiron(IV) unit. In reactions with substrates containing C-H bonds like Triphenylmethane, Cumene, ethylbenzene and Toluene, **6b** reacts at least *2-3 orders* of magnitude faster than **6c**. Furthermore, a detailed kinetic isotope effect study was explored with ethylbenzene and ethylbenzene-D7 as substrates. In both experiments, the second-order rate constant is considerably lower when ethylbenzene-D7 was used leading to a kinetic isotope effect (KIE, k_H/k_D) of $KIE_{\mathbf{6b}}$ = 29 for the reactions with **6b** and $KIE_{\mathbf{6c}}$ = 86 with **6c** as oxidant (Figures 4.4b and 4.4c). This tells us that larger quantum mechanical tunneling is observed in the reaction of 6b & 6c with ethyl benzene. Both oxidants are going through the initial hydrogen atom abstraction pathway.

4.4 Conclusion

In summary, this chapter present here the first experimental characterization of a sulfur ligated iron(IV)-imido complex. The iron(IV)-imido complex was spectroscopically well charcterized and compared with its iron(IV)-oxo counterpart. Also, the reactivity studies in heteroatom oxidation and C-H activation reaction was studied with both the complexes. In both heteroatom oxidation and C-H activation reaction, the iron(IV)-oxo complex seems to be more reactive as compared to the iron(IV)-imido species. The mechanistic pathway for S-oxidation reactions for iron(IV)-oxo and iron(IV)-imido were different. The former proceed via oxygen atom transfer while in the latter case electron transfer is the rate limiting step.

4.5 References

1. M. Sono, M. P. Roach, E. D. Coulter, J. H. Dawson, *Chem. Rev*. 1996, **96**, 2841–2888.
2. J. T. Groves, *Proc. Natl. Acad. Sci. USA*.2003, **100**, 3569–3574.
3. P. R. Ortiz de Montellano, Ed. *Cytochrome P450: Structure, Mechanism and Biochemistry*. 3rd ed.; Kluwer Academic/Plenum Publishers, New York, 2004.
4. K. M. Kadish, K. M. Smith, R. Guilard, Eds. *Handbook of Porphyrin Science*; World Scientific Publishing Co.: New Jersey, 2010.
5. S. P. de Visser and D. Kumar (Eds.) *Iron-containing enzymes: Versatile catalysts of hydroxylation reactions in nature*. RSC Publishing, Cambridge, 2011.
6. M. Costas, M. P. Mehn, M. P. Jensen, L. Que Jr., *Chem. Rev*. 2004, **104**, 939–986.

7. S. V. Kryatov, E. V. Rybak-Akimova, S. Schindler, *Chem. Rev*. 2005, **105**, 2175–2226.
8. M. M. Abu-Omar, A. Loaiza, N. Hontzeas, *Chem. Rev*. 2005, **105**, 2227–2252.
9. R. van Eldik, *Coord. Chem. Rev*. 2007, **251**, 1649–1662.
10. P. C. A. Bruijnincx, G. van Koten, R. J. M. Klein Gebbink, *Chem. Soc. Rev*., 2008, **37**, 2716–2744.
11. A. R. McDonald, L. Que Jr, *Coord. Chem. Rev*., 2013, **257**, 414–428.
12. R. E. White, M. B. McCarthy, *J. Am. Chem. Soc*., 1984, **106**, 4922–4926.
13. E. W. Svastis, J. H. Dawson, R. Breslow, S. H.Gellman, *J. Am. Chem. Soc*., 1985, **107**, 6427–6428.
14. J. Hohenberger, K. Ray, K. Meyer, *Nature Comm*., 2012, **3**, 1–13.
15. D. Mansuy, P. Battioni, J.-P. Mahy, *J. Am. Chem. Soc*. 1982, **104**, 4487–4489.
16. J.-P. Mahy, P. Battioni, D. Mansuy, J. Fisher, R. Weiss, J. Mispelter, I. Morgenstern-Badarau, P. Gans, *J. Am. Chem. Soc*. 1984, **106**, 1699–1706.
17. J.-P. Mahy, P. Nattioni, D. Mansuy, *J. Am. Chem. Soc*. 1986, **108**, 1079–1080.
18. C.-M. Che, C.-Y. Zhou, E. L.-M. Wong, *Top. Organomet. Chem.*2011, **33**, 111–138.
19. T. W.-S. Chow, G.-Q. Chen, Y. Liu, C.-Y. Zhou, C.-M. Che, *Pure Appl. Chem*. 2012, **84**, 1685–1704.
20. J. F. Berry, E. Bill, E. Bothe, S. DeBeer George, B. Mienert, F. Neese, K. Wieghardt, *Science*2006, **312**, 1937–1941.
21. P. Comba, C. Lang, C. Lopez de Laorden, A. Muruganatham, G. Rajaraman, H. Wadepohl, M. Zajaczkowski, *Chem. Eur. J*. 2008, **14**, 5313–5328.

22. K. L. Klotz, L. M. Slominski, M. E. Riemer, J. A. Phillips, J. A. Halfen, *Inorg. Chem.*2009, **48**, 801–803.
23. J. J. Scepaniak, J. A. Young, R. P. Bontchev, J. M. Smith, *Angew. Chem. Int. Ed*. 2009, **48**, 3158–3160.
24. P. Leeladee, G. N. L. Jameson, M. A. Siegler, D. Kumar, S. P. de Visser, D. P. Goldberg, *Inorg. Chem*. 2013, **52**, 4668–4682.
25. M. J. Zdilla, M. M. Abu-Omar, *J. Am. Chem. Soc*. 2006, **128**, 16971-16979.
26. S. Kundu, E. Miceli, E. Farquhar, F. F. Pfaff, U. Kuhlmann, P. Hildebrandt, B. Braun, C. Greco, K. Ray, *J. Am. Chem. Soc.* 2012, **134**,14710−14713.
27. J. W. W. Chang, P. W. H. Chan, *Angew. Chem. Int. Ed.* 2008, **47**, 1138–1140.
28. T. Petrenko, S. DeBeer George, N. Aliaga-Alcalde, E. Bill, B. Mienert, Y. Xiao, Y. S. Guo, W. Sturhahn, S. P. Cramer, K. Wieghardt, F. Neese, *J. Am. Chem. Soc*. 2007, **129**, 11053–11060.
29. R. E. Cowly, N. A. Eckert, S. Vaddadi, T. M. Figureg, T. R. Cundari, P. L. Holland, *J. Am. Chem. Soc*. 2011, **133**, 9796–9811.
30. M. P. Mehn, J. C. Peters, *J. Inorg. Biochem*. 2006, **100**, 634–643.
31. C. M. Thomas, N. P. Mankad, J. C. Peters, *J. Am. Chem. Soc*. 2006, **128**, 4956–4957.
32. I. Neito, F. Ding, R. P. Bontchev, H. Wang, J. M. Smith *J. Am. Chem. Soc*. 2008, **130**, 2716–2717.
33. E. R. King, E. T. Hennessy, T. A. Betley, *J. Am. Chem. Soc*. 2011, **133**, 4917–4923.
34. Y. Liu, X. Guan, E. L. –M. Wong, P. Liu, J. –S. Huang, C.-M. Che, *J. Am. Chem. Soc*. 2013, **135**, 7194–7204.

35. E. T. Hennessy, T. A. Betley, *Science* 2013, **340**, 591–595.
36. E. J. Klinker, T. A. Jackson, M. P. Jensen, A. Stubna, G. Juhász, E. L. Bominaar, E. Münck and L. Que Jr, *Angew. Chem. Int. Ed*., **2006**, *45*, 7394.
37. A. K. Vardhaman, P. Barman, S. Kumar, C. V. Sastri, D. Kumar and S. P. de Visser, *Angew. Chem. Int. Ed*., **2013**, *52*, 12288.
38. S. Kumar, A. S. Faponle, P. Barman, A. K. Vardhaman, C. V. Sastri, D. Kumar and S. P. de Visser, *J. Am. Chem. Soc*., **2014**, *136*, 17102.
39. G. Sabenya, I. Gamba, L. Gómez, M. Clémancey, J. R. Frisch, E. J. Klinker, G. Blondin, S. Torelli, L. Jr. Que, V. Martin-Diaconescu, J. M. Latour, *Chem. Sci*. **2019**, *10*, 9513−9529.
40. G. Mukherjee, F. G. CantúReinhard, U. K. Bagha, C. V. Sastri, S. P. de Visser, *Dalton Trans*. **2020**, *49*, 5921−5931.
41. G. Sabenya, I. Gamba, L. Gómez, M. Clémancey, J. R. Frisch, E. J. Klinker, G. Blondin, S. Torelli, L. Que, V. Martin-Diaconescu, J.-M. Latour, J. Lloret-Fillol, M. Costas, *Chem. Sci*. 2019, 10, 9513–9529.
42. Mokkawes, T.; de Visser, S. P. Caffeine Biodegradation by Cytochrome P450 1A2. What Determines the Product Distributions? Chem. Eur. J. 2023, 29, e202203875.
43. Mukherjee, G.; Alili, A.; Barman, P.; Kumar, D.; Sastri, C. V.; de Visser, S. P. Interplay between steric and electronic effects: A joint spectroscopy and computational study of nonheme iron(IV)-oxo complexes. Chem. Eur. J. 2019, 25, 5086–5098.
44. Bagha, U. K.; Yadav, R.; Mokkawes, T.; Satpathy, J. K.; Kumar, D.; Sastri, C. V.; de Visser, S. P. Defluorination of Fluorophenols by a Nonheme Iron(IV)-Oxo Species: Observation of a New Intermediate Along the Reaction. Chem. Eur. J. 2023, 29, e202300478.

45. Goto, Y.; Matsui, T.; Ozaki, S.-I.; Watanabe, Y.; Fukuzumi, S. Mechanisms of sulfoxidation catalyzed by high-valent intermediates of heme enzymes: electron-transfer vs oxygen-transfer mechanism. J. Am. Chem. Soc. 1999, 121, 9497–9502.
46. Y. Goto, T. Matsui, S.-I. Ozaki, Y. Watanabe , S. Fukuzumi, *J. Am. Chem. Soc.* 1999, **121**, 9497–9502.
47. H. C. Brown, Y. Okamoto, *J. Am. Chem. Soc.*, 1958, **80**, 4979–4987.

CHAPTER – V

Sulfur Ligated Iron(III)-Alkylperoxide Complex: Spectroscopic Insights and Mechanistic Studies of Electrophilic Hydrogen Atom Abstraction with Aldehydes

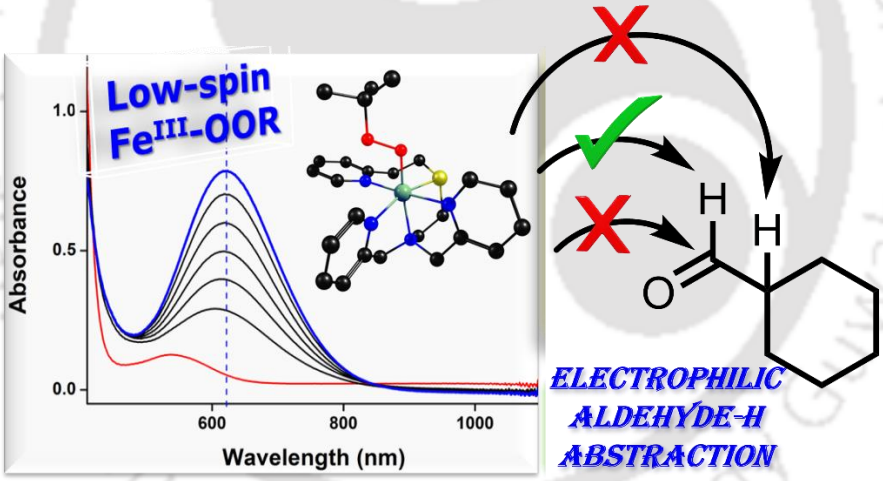

To be Submitted

• •

6.1. Introduction

The handling of dioxygen and its associated compounds, like hydrogen peroxide and superoxide, holds significant importance for various heme and nonheme iron metalloenzymes. In many instances, the generation of iron-oxygen adducts such as iron-superoxide, -hydroperoxide, or -alkylperoxde species stands as a pivotal stage in their operational process. Superoxide reductase (SOR), which is found in anaerobic and microaerophilic species, is an example of a metalloprotein. It contributes to the body's natural defence systems by converting superoxide into hydrogen peroxide.[1-12] In its active site, SOR features a Fe^{II} center surrounded by four histidine-derived imidazolyl nitrogen donors arranged in a planar fashion, along with a cysteine-derived thiolato sulfur donor positioned axially. This configuration results in a square pyramidal [(N_4S(thiolate)] geometry around the iron center. Notably, the coordination structure of SOR shares a clear resemblance with the heme-iron active site of cytochrome P450, where the iron center is coordinated by four pyrrolyl nitrogen donors in the equatorial plane and a cysteinate ligand in the axial position.[13-16] Both enzymes are believed to engage similar iron-(hydro)peroxy intermediates during their catalytic processes. However, these intermediates undergo significantly different outcomes: in SOR, the (hydro)peroxy ligand is released as H_2O_2, while in P450, cleavage of the O-O bond occurs, leading to the generation of a reactive high-valent iron-oxo species.

Spectroscopic and theoretical studies on hydroperoxo- and alkylperoxo-iron(III) models have shown that a low-spin Fe^{III} state leads to stronger Fe-O and weaker O-O bonds, whereas a high-spin Fe^{III} state results in weaker Fe-O and stronger O-O bonds.[17,18] It is hypothesized that a low-spin Fe^{III}-OO(H/R) intermediate in P450 promotes O-O bond cleavage, whereas a high-spin state in SOR aids Fe-O bond

cleavage. Our group recently demonstrated C-O bond cleavage in a nonheme Fe^{III}-alkylperoxide complex with a pentadentate bispidine ligand.[18]

Many synthetic models have been studied to understand metal-mediated transformations. Fe^{III}-hydroperoxide and Fe^{III}-alkylperoxide complexes show sluggish reactivity with organic substrates.[19-24] Various nonheme metal-alkylperoxide intermediates, such as Ni^{III}-OOR and Cu^{II}-OOR, have been studied,[25-29] but many synthetic iron(III)peroxido oxidants remain unreactive under ambient conditions, possibly due to in-situ generation of Fe^{IV}=O complexes upon O-O bond cleavage. Some Fe^{III}-OOH intermediates have been reported as reactive towards organic transformations.[30-41] The reactivity mechanisms of Fe(III)-OOR complexes are unclear due to their thermal instability, with kinetics often ambiguous because of competing reaction pathways. Reports of homolytic or heterolytic O-O bond cleavage exist,[42-47] and the metal center's spin state significantly influences reaction pathways by affecting Fe-O and O-O bond strengths.[48-50] Quantum-chemical calculations suggest high-spin Fe^{III}-alkylperoxido complexes tend to cleave Fe-O bonds, while low-spin complexes lead to homolytic O-O bond scission.[51-56] Some high-spin Fe^{III}-hydroperoxide systems react with organic substrates, displaying amphoteric behaviour.[57] Low-spin Fe^{III}-OOH complexes with well-known N4Py and BnTPeN ligand frameworks react only with halides, showing no reactivity with activated hydrocarbons or heteroatom oxidation.[58,59] Also, many model complexes of thiolate-ligated nonheme Fe(III)-alkylperoxides have been characterized, but these complexes don’t show any oxidative reactivity.[60-62] Herein, we report for the first time, the synthesis, characterization and reaction kinetics of a novel sulfur ligated low-spin Fe^{III}-alkylperoxido moiety which shows electrophilic reactivity towards organic substrates driven by a general O-O bond cleavage pathway.

Table 5.1. Observed Physical properties various Iron(III)-oxygen intermediates.

	λ_{max} (nm)	g values	ν_{Fe-O} (cm^{-1})	ν_{O-O} (cm^{-1})	*Spin state*	*Reactivity*	*Ref*
$[Fe^{III}(TMC)(OOH)]^{2+}$	526	6.8, 5.2, 1.96	658	868	5/2	Amphoteric	57
$[Fe^{III}(Bisp\text{-}NMe_2)(OO^tBu)]^{2+}$	598	4.295	-	-	5/2	Amphoteric	18
$[Fe^{III}([15]aneN_4)(SC_6H_5)(OO^tBu)]^{+}$	526	2.10, 1.97	611	803	1/2	Unreactive	60
$[Fe^{III}(N_3PySR)(OO^tBu)]^{2+}$	600	2.14, 2.08, 1.96	700	796	1/2	Unreactive	61
$[Fe^{III}(Bisp)(OO^tBu)]^{2+}$	605 (ACN)	2.16, 2.13, 1.97	694	790	1/2	Unreactive	62
	560(DCM)	9.4, 7.9, 5.6, 4.3	652	845	5/2	Unreactive	
$[Fe^{III}(L)(OOtBu)]^{2+}$ 8b, this work	**620**	**2.21, 2.19, 2.11**	**687**	**790**	**1/2**	**Amphoteric**	**This work**

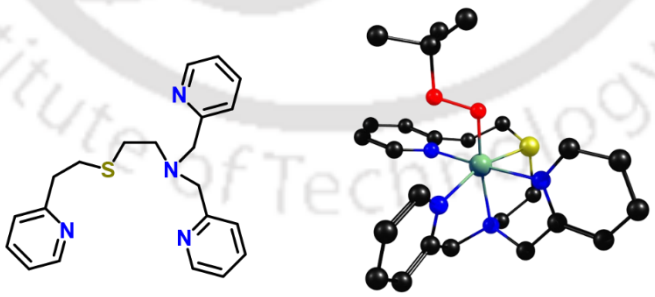

L

$Fe^{III}(OO^tBu)(L)$, 2a

Figure. 5.1. Ligand and oxidant used in this chapter.

6.2. Results and Discussion

6.2.1. Synthesis and Characterization

The pentadentate ligand (L) (L = 2-((2-(pyridin-2-yl)ethyl)thio)-N,N-bis(pyridin-2-ylmethyl)ethan-1-amine) was synthesized and characterized (Figures. 2.10-2.11, Chapter II) according to the previously reported procedures.[63] Subsequently, the ligand L was reacted with $[Fe^{II}(CH_3CN)_2(OTf)_2]$ with OTf = triflate in dry acetonitrile under an inert atmosphere inside a glovebox to form the corresponding iron(II) complex: $[Fe^{II}(L)(CH_3CN)](OTf)_2$ (**8a**). The iron(II) complex was characterized with UV−vis absorption spectroscopy, cyclic voltammetry(CV), NMR spectroscopy, and electrospray ionization mass spectrometry (ESI-MS); (see Figures 2.17, 2.22, Chapter II). The UV−vis spectrum of the iron(II) complex shows a ligand to metal charge-transfer band with a molar extinction coefficient (ε) and λ_{max} values of ε_{8a} = 2200 M^{-1} cm^{-1} ($\lambda_{max,\mathbf{8a}}$ = 358 nm) with a smaller band at 540 nm, ε = 126 $M^{-1}cm^{-1}$, which is due to the sulfur to iron charge transfer. Moreover, cyclic voltammetry studies of the iron(II) complexes **8a** exhibited a irreversible/quassireversible Fe^{II}/Fe^{III} couple. So, we performed the differential pulse voltametric experiment to determine the redox potential of the Fe^{II}/Fe^{III} copule, which is found to be at 1.12 V, Supporting Information Figure 2.22. The ^1H NMR studies establish a paramagnetic nature of **8a** at room temperature. We then calculated the solution state magnetic moment using modified Evan's method. The ^2H NMR Evans method allowed us to determine the magnetic moment of 4.87 μB for **8a** in a mixture of CD_3CN and $CDCl_3$ at 298 K, indicating that the complex **8a** possess a ground-state S=2 spin state in solution. This high spin character of Fe(II) also verifies the irreversible/quassireversible Fe^{II}/Fe^{III} couple during the cyclic voltametric study. The ESI-MS spectrum of **8a** shows prominent peak at 569.06 corresponding to $[Fe^{II}(L)(OTf)]^+$ molecular ion fragment, Figure 2.17.

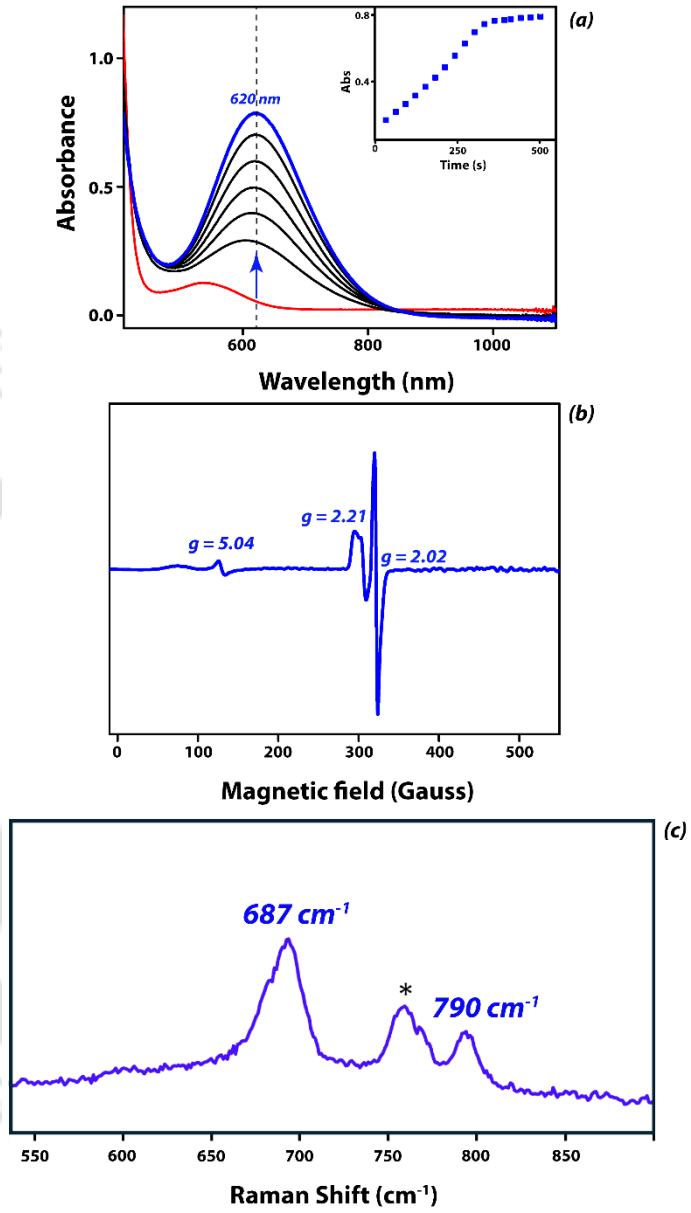

Figure. 5.2. (a) time-dependent UV/vis spectrum for the formation of 8b from 8a at 233 K in MeCN with 30 equiv. of ^{t}BuOOH (the inset shows the time trace at the absorption maximum of 620 nm). (b) Time dependent EPR spectra of 8b in MeCN at 77 K. (c) Resonance Raman spectra of 8b at 233 K at 638 nm excitation wavelength. * indicates for the solvent peaks.

Also, the isotopic distribution patterns for the fragment ion confirms the assignment.

When **8a** was treated with *tert*-butyl hydroperoxide (^{t}BuOOH, 70% in H_2O, 30 eq., MeCN, 233 K), gradually with time it formed a new blue species **8b**. Complex **8b** exhibits an intense absorption band at 620 nm ($\varepsilon \approx 840\ LM^{-1}cm^{-1}$, see Figure. 5.2a). The peak maximum and molar absorptivity are affirmative of the formation of $[Fe^{III}(L)(^{t}BuOO)]^{2+}$ and characteristic for an alkylperoxido to Fe^{III}

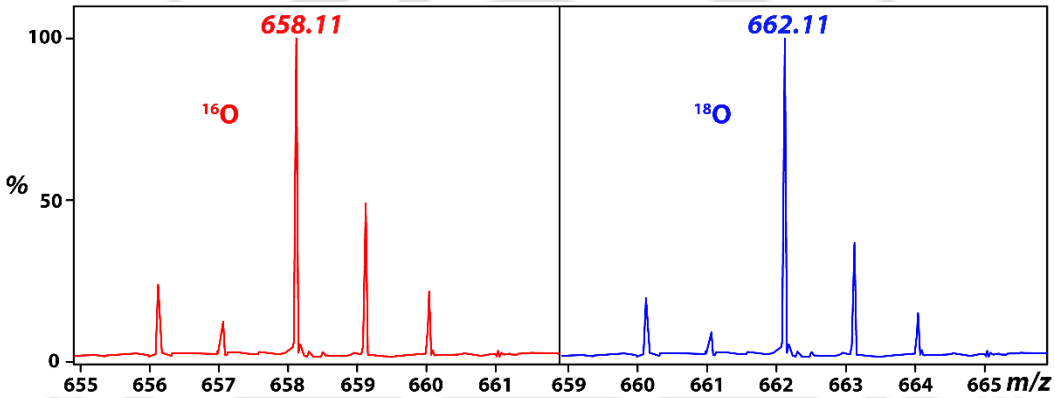

Figure. 5.3. Electrospray ionization mass spectra of 8b in CH_3CN at 233 K. The figure shows expanded isotopic distribution patterns of $[Fe^{III}(^{16}O\text{-}^{16}O^{t}Bu)(L)(OTf)]^{+}$ (in red) and $[Fe^{III}(^{18}O\text{-}^{18}O^{t}Bu)(L)(OTf)]^{+}$ (in blue).

LMCT band.[64,65] In fact, **8b** exhibits sufficient stability for spectroscopic analyses with half-lives of 3 hours at 233 K. the complex **8b** has been well characterized with UV-vis, EPR, resonance Raman spectroscopy, and ESI-MS spectrometry. The positive mode ESI-MS spectrum of **8b** shows major peak at m/z 658.1 corresponds to the molecular ion fragment for $[Fe^{III}(\mathbf{L})(^{t}BuOO)(OTf)]^{+}$.(see Figure 5.3; these assignments are confirmed by their isotopic distribution patterns). Furthermore, the addition of ^{18}O labeled ^{t}BuOOH shifted the m/z 658.11 to 662.11, indicating the coordination of a dioxygen species to iron. Also, the ESI-MS spectra is matching well with the simulated ESI-MS spectra for the complex **8b**. The X-

band EPR spectrum of the frozen solution of **8b** obtained at 77 K shows the spectral feature with major signals at g = 2.02, 2.11, and 2.21, suggestive of the presence of a low-spin Fe^{III}-OOR complex, with a minor signal at g = 5.04 indicative of the presence of a high-spin Fe(III)-OH complex. (See, Figure 5.2b).[60-62] Also, The resonance Raman spectra of **8b** obtained at 638 nm excitation wavelength feature two resonantly enhanced bands at 687 cm^{-1} and 790 cm^{-1} that was not there in the starting Fe(II) complex as well as in the spectra for the solvent. In analogy with the previously reported Fe^{III}-OOR species, we have assigned these bands as having originated from the Fe-O (687 cm^{-1}) and O-O (790 cm^{-1}) stretch, see Figure 5.2c.[61,62] Which shows the presence of a strong Fe-O bond and weak O-O bond. The observation of these two resonantly enhanced Raman bands together with the EPR and ESI-MS data strongly suggests **8b** to be a low-spin Fe(III)-OO^{t}Bu species.

The stability of **8b** at 233 K prompted an investigation of its reactivity with organic substrates. However, the addition of organic substrates to complex **8b** significantly accelerated the decay rate of the corresponding LMCT band, thereby indicating that the substrates are reacting with complex **8b**. Previously, several efforts were made to determine the decay rates and pathways for Fe^{III}-OOR complexes, but such exercises were rarely met with success. The reaction of **8b** with thioanisole was not possible at 233 K. Instead, we used dimethylsulfide as a substrate for sulfoxidation reaction. So, with different concentration of dimethylsulfide, a linear dependence between k_{obs} and the concentration of dimethylsulfide was seen at 233 K. The second-order rate constant k_2 = 1.54 x 10^{-2} $M^{-1}s^{-1}$ was determined. Then we also tried the reaction with triphenylphosphine as the model substrate for oxygen atom transfer reaction. Addition of excess equivalent of triphenylphosphine leads to the decomposition of **8b** under pseudo-first-order conditions, as monitored with the decay of the 620 nm band in the UV/vis spectrum (See Figure S11). While

testing its oxygen atom transfer (OAT) abilities, a linear dependence between k_{obs} and the triphenylphosphine concentration was obtained at 233 K in MeCN, giving a second-order rate constant k_2 = 1.48 $M^{-1}s^{-1}$. Interestingly, the reaction with thioanisole was found to be very sluggish at 233 K. However, **8b** was found to be

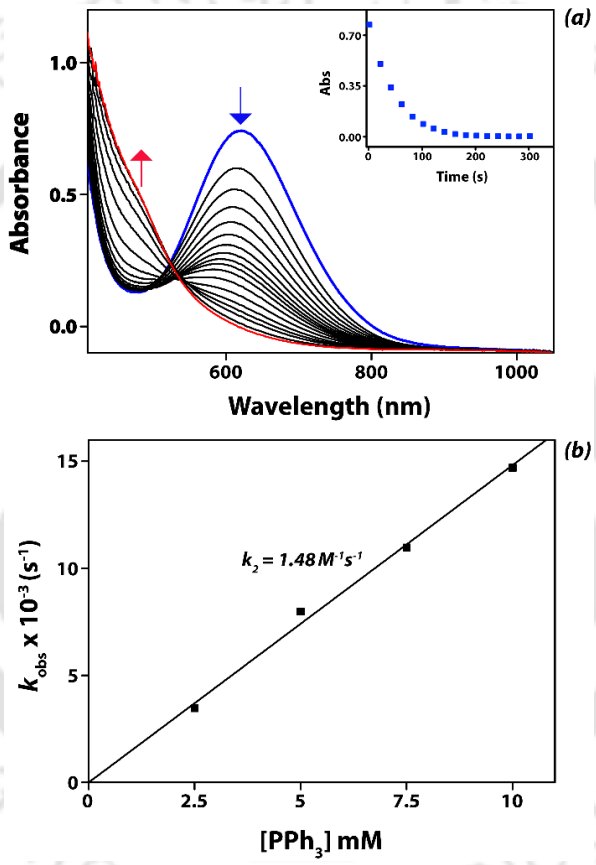

Figure. 5.4. (a) UV−vis spectral changes of 8b upon addition of 10 equiv. of Triphenylphosphine in MeCN at 233 K. The inset shows the decay profile of the 620 nm band. (b) Second-order rate constant determined for the reaction of 8b with different concentration of triphenylphosphine in MeCN at 233 K.

unreactive with other oxygen atom acceptors like cyclooctene and styrene, precluding the study of olefin epoxidation reactions.

Metal-dioxygen species like peroxido, hydroperoxido, and alkylperoxido complexes are effective at deformylating aldehydes.[66] Typically, these reactions involve a direct nucleophilic attack by the oxidant on the electrophilic carbonyl carbon.[67,68] However, for aldehydes with an α-hydrogen, an alternative electrophilic pathway has been reported for Mn^{III}-peroxido and Cu^{II}-peroxido intermediates.[69-71] It's suggested that an α-position hydrogen can lead to C-H abstraction through keto-enol tautomerism.[69]

To determine the reactivity of the iron(III)-alkylperoxido complex in this study, we conducted a detailed kinetic analysis using cyclohexanecarboxaldehyde (CCA) as a model substrate. When CCA was added to **8b** in MeCN at 233 K, the intermediate quickly decayed (Figure 5.5a). The decay rate of the 620 nm band in the UV-vis spectrum increased linearly with increasing CCA concentration, suggesting a bimolecular reaction mechanism. The second-order rate constant (k_2) for the oxidation of CCA by **8b** at 233 K was found to be 2.21×10^{-2} $M^{-1}s^{-1}$ (Figure 5.5b). Product analysis showed the formation of cyclohexanecarboxylic acid. Regardless of the reaction pathway, the same products were observed in aldehyde deformylation reactions. To resolve the reaction pathway conflicts, we used the kinetic isotope effect (KIE) as a tool. Replacing the C_α–H group in CCA with deuterium served as a probe for identifying the rate-determining step. When α-[D_1]-CCA was used, the second-order rate constant was 2.64×10^{-2} $M^{-1}s^{-1}$ (Figure 5.5b). The lack of a KIE indicates that electrophilic Cα−H bond cleavage is not the rate-determining step.

To explore the potential nucleophilic oxidation pathway for the oxidation of CCA, a series of *para*-substituted benzaldehyde were used to evaluate the Hammett

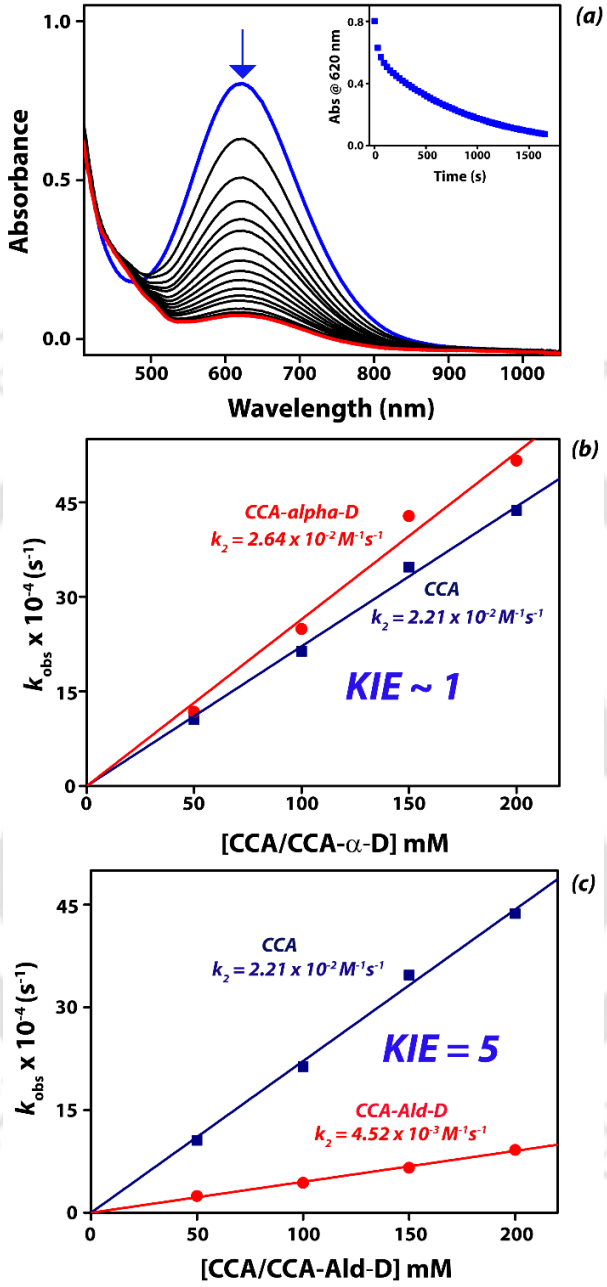

Figure. 5.5. (a) UV−vis spectral changes of 8b upon addition of 100 equiv. of cyclohexanecarboxaldehyde in MeCN at 233 K. The inset shows the decay profile of the 620 nm band. (b) Second-order rate constant determined for the reaction of 8b with different concentration of triphenylphosphine in MeCN at 233 K. (c) Second-order rate constant determined for the reaction of 8b with different concentration of CCA and Ald-D-CCA in MeCN at 233 K.

analysis. In the nucleophilic pathway, the oxidant attacks the carbonyl group leading to the formation of iron alkoxide adduct. This should result in a positive Hammett plot. Upon addition of an excess amount of various *para*-substituted benzaldehyde to **8b** induced the disappearance of the 620 nm band. A plot of the reaction rates against their para-substituent constants (σ_p) produces a Hammett plot with a negative slope (ρ = -0.98) which is contra indicative of the formation of iron

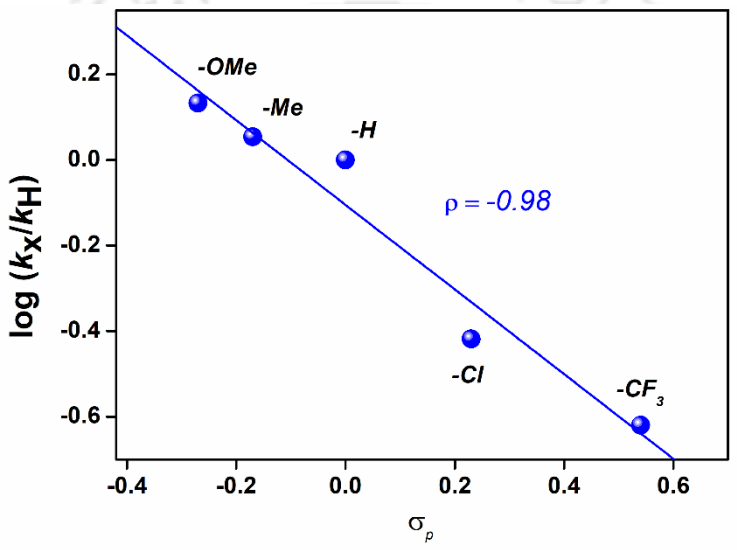

Figure. 5.6. Hammett plot of 8b with different *para*-substituted benzaldehydes in MeCN at 233 K.

alkoxide adduct during the nucleophilic attack at the carbonyl group (see, figure 5.6). The negative hammett slope indicates that the reaction proceeds via an electrophilic pathway instead. After ruling out the electrophilic C_α–H abstraction and the nucleophilic iron alkoxide adduct formation, the only plausible pathway for the electrophilic cyclohexanecarboxaldehyde oxidation to cyclohexane carboxylic acid should involve C-H abstraction of aldehydic-hydrogen atom. To confirm this reaction pathway, we now employed ald-D-CCA as a substrate, which gave a classical KIE of 5 under identical reaction conditions. This pathway is very similar to the oxidation of aldehydes by Fe^{IV}=O intermediates. To prove further

that **8b** reacts with aldehydes via the formation of Fe^{IV}=O species we now carried out the reactions with a series of aliphatic aldehydes. The electrophilicity of **8b** in the reaction with aldehydes was further investigated by employing a primary (Valeraldehyde for 1°-CHO), a secondary (2-methylbutyraldehyde for 2°-CHO), and a tertiary (Trimethylacetaldehyde for 3°-CHO) aldehyde (See table 5.3). The order of reaction rates (k_2) was observed to be 3°-CHO > 2°-CHO > 1°-CHO, which supports again the electrophilic character of **8b** in the oxidation reaction of aldehydes as well.

Generally, low-spin Fe^{III}-OOR complexes experience homolytic cleavage of the peroxido (O-O) bond, leading to the formation of a proposed Fe^{IV}=O moiety.[42,43] Lewis bases are typically employed to facilitate the peroxide bond cleavage, which exerts a push effect by coordinating to the metal ion, thereby accelerating the transformation from Fe^{III}-OOR to Fe^{IV}=O species.[72-75] Upon the addition of pyridine-N-oxide (10 equivalents) to **8b** at 233 K, the existing LMCT band decays rapidly with the formation of a new band at 500 nm in the UV/vis- spectrum, see Figure 5.6. While the literature suggests that the push effect drastically accelerates the decay of the Fe^{III}-OOR LMCT band, such that the Fe^{IV}=O chromophore should have been visible within seconds. But, in our case, no Fe^{IV}=O chromophore was seen upon the addition of a Lewis base to (L)Fe^{III}-OOR. But there is a band at 500 nm which may be due to the conversion of Fe^{III}-OOR to an highly unstable Fe^{IV}=O intermediate, which in turn self-decays to form the Fe^{II} complex, Which has been validated with EPR spectroscopic methods. So, we have performed the EPR experiment to get an idea about the spin-state of the decayed species after the addition of an excess amount of pyridine N-oxide to **8b**. From the EPR studies, We found the decayed species to be the Fe(II) complex with a trace amount of Fe(III) still present in it. Also, we performed the radical trapping experiment with CCl_3Br

as a probe to check the reaction pathway through which the reaction is progressing.[18]

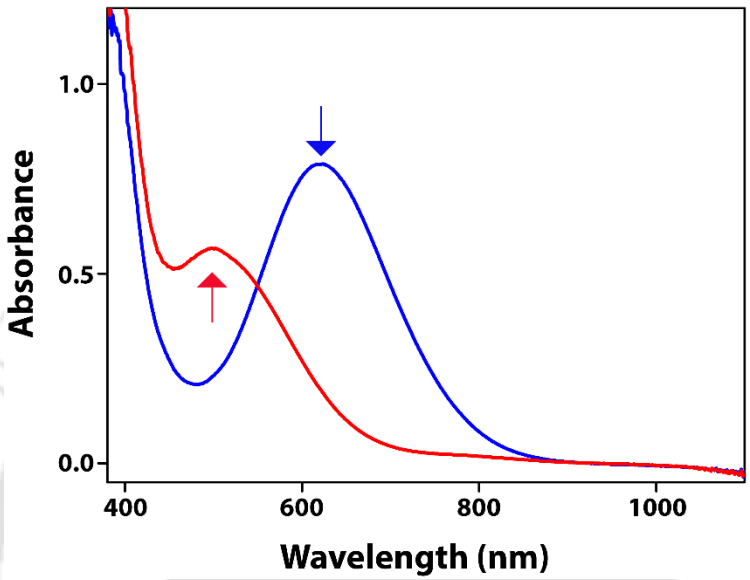

Figure. 5.7. UV−vis spectral changes of 8b upon addition of 10 equiv. of Pyridine-N-oxide in MeCN at 233 K.

When **8b** was reacted with triphenylphosphine as OAT substrate in the presence of the radical trapping reagent CCl_3Br, we did not see the brominated product, 2-bromo-2-methylpropane, but we did see the tertiary butanol as product. This clearly establishes the homolytric O-O bond cleavage during the course of the reaction to form a putative Fe^{IV}=O species, which is highly unstable in turn it decays to give the Fe(II) product.

Table. 5.2. Pseudo first-order rate constants determined for the reaction of 8b (1 mM) with CCA with α-[D_1]-CCA and Ald-[D_1]-CCA in CH_3CN at -40°C.

Concentration (mM)	k_{obs} x 10^{-2} for CCA	k_{obs} x 10^{-2} for α-[D_1]-CCA	k_{obs} x 10^{-2} for Ald-[D_1]-CCA
50	0.106	0.118	0.024
100	0.213	0.249	0.043
150	0.347	0.368	0.066
200	0.437	0.456	0.092

Table. 5.3. Pseudo first-order rate constants determined for the reaction of 8b (1 mM) with aliphatic aldehydes in CH_3CN at -40°C.

Concentration (mM)	k_{obs} x 10^{-2} for Valeraldehyde	k_{obs} x 10^{-2} for 2-Methylbutyraldehyde	k_{obs} x 10^{-2} for Trimethylacetaldehyde
150	0.113	0.232	0.407

Scheme 5.1. Possible reaction sites on CCA with 8b.

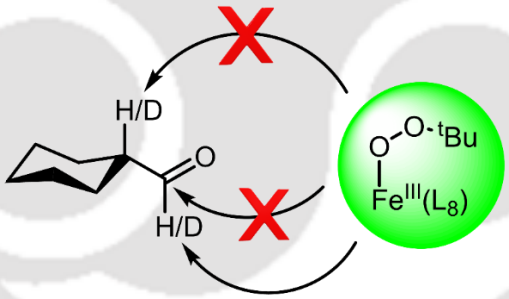

6.3. Conclusion

We report here in this chapter, the generation of a novel sulfur ligated low-spin (S = 1/2) Fe^{III}-OOR species supported by a pentadentate N4S ligand backbone. Generally, the low-spin Fe(III)-alkylperoxide complexes are known for their sluggish or no reactivity towards organic substrates. But here in, complex **8b** is one of a kind that shows electrophilic reactivity towards electrophilic oxygen atom transfer substrates as well as aldehydes. A thorough experimental mechanistic

study confirms the abstraction of aldehydic-hydrogen from cyclohexanecarboxaldehyde to give cyclohexanecarboxylic acids. The detailed DFT analysis implies that the reactions proceed via a O-O bond cleavage to form a putative Fe^{IV}=O complex during the catalytic process.

6.4. References

1. V. Nivière, M. Fontecave, *J. Biol. Inorg. Chem*. **2004**, *9*, 119–123.
2. D. M. Kurtz Jr. *J. Inorg. Biochem*. **2006**, *100*, 679–693.
3. A. Dey, F. E. Jenney, M. W. W. Adams, M. K. Johnson, K. O. Hodgson, B. Hedman, E. I. Solomon. *J. Am. Chem. Soc*. **2007**, *129*, 12418–12431.
4. V. W. Huang, J. P. Emerson, D. M. Kurtz Jr. *Biochemistry*. **2007**, *46*, 11342–11351.
5. J. A. Kovacs, L. M. Brines. *Acc. Chem. Res*. **2007**, *40*, 501–509.
6. C. Mathe´, C. O. Weill, T.A. Mattioli, C. Berthomieu, C. Houe´e-Levin, E. Tremey, V. Nivie`re. *J. Biol. Chem*. **2007**, *282*, 22207–22216.
7. S. P. de Visser, G. Mukherjee, H. S. Ali, C. V. Sastri, *Acc. Chem. Res*. **2022**, *55*, 65–74.
8. I. Moura, S. R. Pauleta, J. J. G. Moura. *J. Biol. Inorg. Chem*. **2008**, *13*, 1185–1195.
9. G. Katona, P. Carpentier, V. Nivie`re, P. Amara, V. Adam, J. Ohana, N. Tsanov, D. Bourgeois. *Science.* **2007**, *316*, 449–453.
10. M. D. Clay, T. C. Yang, F. E. Jenney, I. Y. Kung, C. A. Cosper, R. Krishnan, D. M. Kurtz Jr., M. W. W. Adams, B. M. Hoffman, M. K. Johnson. *Biochemistry*. **2006**, *45*, 427–438.

11. A. S. Pereira, P. Tavares, F. Folgosa, R. M. Almeida, I. Moura, J. J. G. Moura. *Eur. J. Inorg. Chem*. **2007**, 2569–2581.
12. S. G. Sligar, T. M. Makris, I. G. Denisov. *Biochem. Biophys. Res. Commun*. **2005**, *338*, 346–354.
13. S. Shaik, D. Kumar, S. P. de Visser, A. Altun, W. Thiel. *Chem. ReV*. **2005**, *105*, 2279–2328
14. G. H. Loew, D. L. Harris. *Chem. ReV*. **2000**, *100*, 407–419.
15. I. G. Denisov, T, M. Makris, S. G. Sligar, I. Schlichting. *Chem. ReV*. **2005**, *105*, 2253–2277.
16. N. Lehnert, R. Y. N. Ho, L. Que Jr., E. I. Solomon. *J. Am. Chem. Soc*. **2001**, *123*, 12802–12816.
17. N. Lehnert, R. Y. N. Ho, L. Que Jr., E. I. Solomon. *J. Am. Chem. Soc*. **2001**, *123*, 8271–8290.
18. G. Mukherjee, G. Velmurugan, M. Kersher, J. K. Satpathy, C. V. Sastri, P. Comba. *Chem. Eur. J*., **2024**, *30*, e202303127.
19. M. S. Seo, T. Kamachi, T. Kouno, K. Murata, M. J. Park, K. Yoshizawa, W. Nam, *Angew. Chem. Int. Ed*. **2007**, *46*, 2291-2294
20. C. Würtele, E. Gaoutchenova, K. Harms, M. C. Holthausen, J. Sundermeyer, S. Schindler, *Angew. Chem. Int. Ed.* **2006**, *45*, 3867-3869.
21. S. Itoh, *Acc. Chem. Res.* **2015**, *48*, 2066-2074.
22. J. J. Liu, D. E. Diaz, D. A. Quist, K. D. Karlin, *Isr. J. Chem.* **2016**, *56*, 738-755.
23. C. E. Elwell, N. L. Gagnon, B. D. Neisen, D. Dhar, A. D. Spaeth, G. M. Yee, W. B. Tolman, *Chem. Rev.* **2017**, *117*, 2059-2107.
24. J. K. Satpathy, R. Y. Yadav, U. K. Bagha, D. Kumar, C. V. Sastri, S. P. de Visser, *Inorg. Chem*. **2024**, *63*, 6752-6766.

25. B. Kim, D. Jeong, J. Cho, *Chem. Commun.* **2017**, *53*, 9328-9331.
26. S. Hikichi, H. Okuda, O. Yoshiko, M. Akita, *Angew. Chem. Int. Ed.* **2009**, *48*, 188-191.
27. M. S. Seo, T. Kamachi, T. Kouno, K. Murata, M. J. Park, K. Yoshizawa and W. Nam, *Angew. Chem. Int. Ed*. **2007**, *46*, 2291.
28. M. J. Park, J. Lee, Y. Suh, J. Kim and W. Nam, *J. Am. Chem. Soc*. **2006**, *128*, 2630.
29. R. Kumar, A. Maji, B. Biiswas, A. Draksharapu, *Dalton. Trans*. **2024**, *53*, 5401-5406.
30. T. Ogihara, S. Hikichi, M. Akita, T. Uchida, T. Kitigawa, Y. Moro-oka, *Inorg. Chem. Acta*, **2000**, *297*, 162-170.
31. A. P. Sobolev, D. E. Babushkin, E. P. Talsi, *J. Mol. Catal. A*. **2000**, *159*, 233-245.
32. J. Kim, Y. Zang, M. Costas, R. G. Harrison, E. C. Wilkinson, L. Que, Jr., *J. Biol. Inorg. Chem*. **2001**, *6*, 275-284.
33. M. P. Jensen, S. J. Lange, M. P. Mehn, E. L. Que, L. Que, Jr. *J. Am. Chem. Soc*. **2003**, *125*, 2113-2128.
34. N. Lehnert, K. Fujisawa, E. I. Solomon, *Inorg. Chem*. **2003**, *42*, 469-481.
35. J.-U. Rohde, S. Torelli, X. Shan, M. H. Lim, E. J. Klinker, J. Kaizer, K. Chen, W. Nam, L. Que, Jr. *J. Am. Chem. Soc*. **2004**, *126*, 16750-16761.
36. M. P. Jensen, M. Costas, R. Y. N. Ho, J. Kaizer, A. Mariata i Payeras, E. Münck, L. Que, Jr., J.-U. Rohde, A. Stubna, *J. Am. Chem. Soc*. **2005**, *127*, 10512-10525.
37. T. K. Paine, M. Costas, J. Kaizer, L. Que, Jr. *J. Biol. Inorg. Chem*. **2006**, *11*, 272-276.
38. J. Bautz, P. Comba, L. Que, Jr. *Inorg. Chem*, **2006**, *45*, 7077-7082.

39. X. Shan, J.-U. Rohde, K. D. Koehntop, Y. Zhou, M. R. Bukowski, M. Costas, K. Fujisawa, L. Que, Jr., *Inorg. Chem*. **2007**, *46*, 8410-8417.
40. F. Namuswe, G. D. Kasper, A. A. N. Sarjeant, T. Hayashi, C. M. Krest, M. T. Green, P.Moënne-Loccoz, D. P. Goldberg, *J. Am. Chem. Soc*. **2008**, *130*, 14189-14200.
41. F. Namuswe, T. Hayashi, Y. Jiang, G. D. Kasper, A. A. N. Sarjeant, P. Moënne-Loccoz, D. P. Goldberg, *J. Am. Chem. Soc*. **2010**, *132*, 157-167.
42. S. Ménage, E. C. Wilkinson, L. Que, Jr., M. Fontecave, *Angew. Chem. Int. Ed*. **1995**, *34*, 203-205.
43. R. Y. Ho, G. Roelfes, B. L. Feringa, L. Que, *J. Am. Chem. Soc*. **1999**, *121*, 264-265.
44. A. Bassan, M. R. Blomberg, P. E. Siegbahn, L. Que, Jr. *J. Am. Chem. Soc*. **2002**, *124*, 11056-11063.
45. W. N. Oloo, A. J. Fielding, L. Que, Jr. *J. Am. Chem. Soc*. **2013**, *135*, 6438-6441.
46. S. Bang, S. Park, Y.-M. Lee, S. Hong, K.-B. Cho, W. Nam, *Angew. Chem. Int. Ed*. **2014**, *53*, 7843-7847.
47. I. Ghosh, S. Banerjee, S, Paul, T. Corona, T. K. Paine, *Angew. Chem. Int. Ed*. **2019**, *58*, 12534-12539.
48. J. J. Girerd, F. Banse, A. J. Simaan, *Struct. Bonding (Berlin)*. **2000**, *97*, 145-177.
49. M. P. Jensen, A. Mariata i Payeras, A. T. Fiedler, M. Costas, J. Kaizer, A. Stubna, E. Münck, L. Que, Jr. *Inorg. Chem*. **2007**, *46*, 2398-2408.
50. J. Kaizer, M. Costas, L. Que, Jr., *Angew. Chem. Int. Ed*. **2003**, *42*, 3671-3673.

51. N. Lehnert, R. Y. N. Ho, L. Que, Jr., E. I. Solomon, *J. Am. Chem. Soc*. **2001**, *123*, 8271-8290.
52. N. Lehnert, R. Y. N. Ho, L. Que, Jr., E. I. Solomon, *J. Am. Chem. Soc*. **2001**, *123*, 12802-12816.
53. L. R. Widger, Y. Jiang, A. C. McQuilken, T. Yang, M. A. Siegler, H. Matsumura, P. Moënne-Loccoz, D. Kumar, S. P. de Visser, D. P. Goldberg, *Dalton Trans*. **2014**, *43*, 7522-7532.
54. Y. Zang, J. Kim, Y. Dong, E. C. Wilkinson, E. H. Appelman, L. Que, Jr., *J. Am. Chem. Soc*. **1997**, *119*, 4197-4205.
55. M. R. Bukowski, H. L. Halfen, T. A. van den Berg, J. A. Halfen, L. Que, Jr., *Angew. Chem. Int. Ed*. **2005**, *44*, 584-587.
56. D. Krishnamurthy, G. D. Kasper, F. Namuswe, W. D. Kerber, A. A. N. Sarjeant, P. Moënne-Loccoz, D. P. Goldberg, *J. Am. Chem. Soc*. **2006**, *128*, 14222-14223.
57. J. Cho, S. Jeon, S. A. Wilson, L. V. Liu, E. A. Kang, J. J. Braymer, M. H. Lim, B. Hedman, K. O. Hodgson, J. S. Valentine, E. I. Solomon, W. Nam, *Nature*, **2011**, *478*, 502–505.
58. A. K. Vardhaman, C. V. Sastri, D. Kumar, S. P. de Visser, *Chem. Commun.* **2011**, *47*, 11044–11046.
59. A. K. Vardhaman, P. Barman, S. Kumar, C. V. Sastri, D. Kumar, S. P. de Visser, *Angew. Chem. Int. Ed.* **2013**, ***52***, 12288–12292.
60. D. Krishnamurthy, G. D. Kasper, F. Namuswe, W. D. Kerber, A. A. N. Sarjeant, P. Monne-Loccoz, D. P. Goldberg, *J. Am. Chem. Soc*. **2006**, *128*, 14222–14223.
61. L. R. Widger, Y. Jiang, A. C. McQuilken, T. Yang, M. A. Siegler, H. Matsumura, P. Moenne-Loccoz, D. Kumar, S. P. de Visser, D. P. Goldberg, *Dalton Trans*. **2014**, *43*, 7522 – 7532.

62. J. Bautz, P. Comba, L. Que, Jr., *Inorg. Chem*. **2006**, *45*, 7077-7082.
63. R. R. Fernandes, J. Lasri, M. F. C. Guedes da Silva, J. A. L. da Silva, J. J. R. Frafflsto da Silva, A. J. L. Pombeiro, *J. Mol. Catal. A: Chem*. **2011**, *351*, 100 – 111.
64. J. Kim, E. Larka, E. C. Wilkinson, L. Que, Jr., *Angew. Chem. Int. Ed. Engl.* **1995**, *34*, 2048-2051; *Angew. Chem.* **1995**, *107*, 2191-2194.
65. A. Wada, S. Ogo, Y. Watanabe, M. Mukai, T. Kitagawa, K. Jitsukawa, H. Masuda, H. Einaga, *Inorg. Chem.* **1999**, *38*, 3592-3593.
66. U. K. Bagha, J. K. Satpathy, G. Mukherjee, C. V. Sastri, S. P. de Visser, *Org. Biomol. Chem*. **2021**, *19*, 1879–1899.
67. G. Mukherjee, J. K. Satpathy, U. K. Bagha, M. Q. E. Mubarak, C. V. Sastri, S. P. de Visser, *ACS Catal*. **2021**, *11*, 9761–9797.
68. G. Mukherjee, C. V. Sastri, *Isr. J. Chem*. **2020**, *60*, 1032-1048.
69. P. Barman, P. Upadhyay, A. S. Faponle, J. Kumar, S. S. Nag, D. Kumar, C. V. Sastri, S. P. de Visser, *Angew. Chem. Int. Ed*. **2016**, *55*, 11091-11095.
70. F. G. Cantú Reinhard, P. Barman, G. Mukherjee, J. Kumar, D. Kumar, D. Kumar, C. V. Sastri, S. P. de Visser, *J. Am. Chem. Soc*. **2017**, *139*, 18328-18338.
71. S. S. Nag, G. Mukherjee, P. Barman, C. V. Sastri, *Inorg. Chim. Acta*, **2019**, *485*, 80-85.
72. K. Yamaguchi, Y. Watanabe and I. Morishima, *J. Am. Chem. Soc*. **1993**, *115*, 4058.
73. S. Hong, L. Yong-Min, C. Kyung-Bin, M. S. Seo, D. Song, J. Yoon, R. Garcia-Serres, M. Clémancey, T. Ogura, W. Shin, J.-M. Latour and W. Nam, *Chem. Sci*. **2014**, *5*, 156.

74. M. Sono, M. P. Roach, E. D. Coulter and J. H. Dawson, Chem. Rev. 1996, 96, 2841.
75. J. Kaizer, M. Costas and L. Que, Jr., *Angew. Chem. Int. Ed*. **2003**, *42*, 3671.
76. W. L. Armarego and D. D. Perrin, Purification of laboratory chemicals, Pergamon Press, Oxford, **1997**.

CHAPTER-VI

- **Thesis Overview & Future Prospects**

This thesis investigates the generation, characterization, and reactivity of various sulfur-ligated high-valent non-heme iron intermediates. Specifically, it focuses on the chemistry of non-heme iron(IV)-oxo, iron(IV)-tosylimido, and iron(III)-alkylperoxo systems. Chapter III demonstrates the significant impact of substituting a sulfur ligand for an N-CH3 group on the reactivity of the iron(IV)-oxo species. Chapter IV details the creation of a sulfur-ligated iron(IV)-tosylimido complex and compares its properties with those of the iron(IV)-oxo analogue. Chapter V presents the generation of a sulfur-ligated iron(III)-alkylperoxo species and introduces a novel mechanism for its reaction with aldehydes.

This field of bio-inorganic chemistry is both promising and challenging due to its inherent uncertainties. Small modifications can lead to significant changes, complicating predictions. For instance, in Chapter III, replacing the N-CH3 group with a sulfur ligand alters the reaction mechanism for both sulfoxidation and C-H bond activation. However, in Chapter IV, this substitution does not affect the reaction mechanism. A new direction is explored in aldehyde deformylation reactions, where Chapter V reveals a novel pathway involving the abstraction of an aldehydic-H bond from CCA by a Fe(III)-alkylperoxo species, which then undergoes O-O bond cleavage to produce an iron(IV)-oxo species. Typically, iron(III)-peroxo complexes employ a nucleophilic mechanism for deformylating CCA. Thus, the overall reactivity and mechanisms are influenced by various interacting factors, making it an exciting journey to explore the specific effects that differentiate each species.

- **List of Publications**

1. **Satpathy, J. K.**; Yadav, R.; Bagha, U. K.; Kumar, D.; Sastri, C. V.; de Visser, S. P.; Enhanced Reactivity through Equatorial Sulfur Coordination in Nonheme Iron(IV)–Oxo Complexes: Insights from Experiment and Theory. *Inorg. Chem.* **2024**, *63*, 6752–6766.
2. Mukherjee, G.; Velmurugan, G.; Kerscher, M.; **Satpathy, J. K**.; Sastri, C. V.; Comba, P.; Mechanistic Insights into Amphoteric Reactivity of an Iron-Bispidine Complex. *Chem. Eur. J.* **2024**, *30*, e202303127.
3. Sahoo, L.; **Satpathy, J. K**.; Yadav, R.; de Visser, S. P.; Sastri, C. V.; Equatorial Perturbation Driven Reaction Bifurcation in Non-Heme Iron Complexes for Chlorite Oxidation. *Eur. J. Inorg. Chem*, **2023**, *26*, e202300380.
4. Bagha, U. K.; Yadav, R.; Mokkawes, T.; **Satpathy, J. K**.; Kumar, D.; Sastri, C. V.; de Visser, S. P. Defluorination of Fluorophenols by a Nonheme Iron(IV)-Oxo Species: Observation of a New Intermediate Along the Reaction. *Chem. Eur. J*. **2023**, *29*, e202300478.
5. Yeh, G, C-C.; Ghafoor, S.; **Satpathy, J. K.**; Mokkawes, T.; Sastri, C. V.; de Visser S. P. Cluster Model Study into the Catalytic Mechanism of α-Ketoglutarate Biodegradation by the Ethylene-Forming Enzyme Reveals Structural Differences with Nonheme Iron Hydroxylases. *ACS. Catal.*, **2022,** *12*, 3923-3937.
6. Bagha, U. K.; **Satpathy, J. K**.; Mukherjee, G.; Barman, P.; Kumar, D.; de Visser S. P.; Sastri, C. V. Oxidative dehalogenation of halophenols by high-valent nonheme iron(IV)-oxo intermediates. *Faraday Discuss.*, **2022**, *234*, 58–69.

7. Bagha. U. K.; **Satpathy. J. K**.; Mukherjee, G.; Sastri, C. V. de Visser, S. P. A Comprehensive Insight into Aldehyde Deformylation: Mechanistic Implications from Biology and Chemistry. *Org. Biomol. Chem*., **2021**, *19*, 1879-1899.
8. Roach, S.; Faponle, A. S.; **Satpathy, J. K**.; Sastri, C. V.; de Visser. S. P. Substrate sulfoxidation by a biomimetic cytochrome P450 Compound I mimic: How do porphyrin and phthalocyanine equatorial ligand compare?. *J. Chem. Sci*, **2021**, *133*, 61-74.
9. Mukherjee, G.; **Satpathy, J. K**.; Bagha, U. K.; Mubarak, M. Q. E.; Sastri, C. V.; de Visser, S. P. Inspiration from Nature: Influence of Engineered Ligand Scaffolds and Auxiliary Factors on the Reactivity of Biomimetic Oxidants. *ACS. Catal*., **2021**, *15*, 9761 - 9797.

- **List of Presentations**

1. Jagnyesh Kumar Satpathy, ***Poster Presenter*** at National symposium in chemistry: "CRSI-NSC-28" at IIT Guwahati, India, from March 25-27, 2022.
2. Jagnyesh Kumar Satpathy, ***Poster Presenter*** at "Frontiers in Chemical Sciences-2022", IIT Guwahati, India, from December 2-4, 2022.
3. Jagnyesh Kumar Satpathy, ***Poster Presenter*** at international conference on "Modern Trends in Inorganic Chemistry-XX", IISC Bangalore, India, from December 14-17, 2023.
4. Jagnyesh Kumar Satpathy, ***Poster Presenter*** at international conference on "6th Symposium on Advanced Biological Inorganic Chemistry, SABIC 2024", Kolkata, India, from January 7-11, 2024.
5. Jagnyesh Kumar Satpathy, ***Oral Presenter*** at National Conference: "Recent Trends In Chemical Sciences" (RETICS-2024), Sambalpur University, India from March 01-03, 2024.

: Short Biography :

Jagnyesh Kumar Satpathy is a post-graduate researcher at the Department of Chemistry, IIT Guwahati. He was born to Shri. Lalu Satpathy and Smt. Sunita Satpathy in a village named Bahabal, Odisha, India. He did his schooling from D. D. P High School, Bahabal, and graduated in 2016 with Chemistry (Hons.) from Rajendra Autonomous College, Balangir. He completed his Master's Degree (M.Sc.) in Applied Chemistry from the Sambalpur University, Odisha in 2019. Later that year he joined the research group of Prof. Chivukula Vasudeva Sastri at IIT Guwahati and did his Ph.D. research work based on the mechanistic insights into the role of sulfur ligation on the oxidative reactivity of high-valent non-heme iron intermediates.